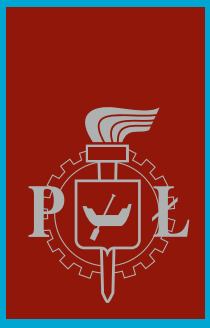

Politechnika Łódzka

ZESZYTY NAUKOWE Nr 1087

LAURENT BABOUT

STUDY OF DEGRADATION PROCESSES IN ENGINEERING MATERIALS USING X-RAY (MICRO)TOMOGRAPHY AND DEDICATED VOLUMETRIC IMAGE PROCESSING AND ANALYSIS

ŁÓDŹ 2011

POLITECHNIKA ŁÓDZKA

ZESZYTY NAUKOWE Nr 1087

ROZPRAWY NAUKOWE, Z. 403

LAURENT BABOUT

STUDY OF DEGRADATION PROCESSES IN ENGINEERING MATERIALS USING X-RAY (MICRO)TOMOGRAPHY AND DEDICATED VOLUMETRIC IMAGE PROCESSING AND ANALYSIS

ŁÓDŹ 2011

TABLE OF CONTENT

Summary ……..…. 7

List of acronyms ……..…… 8

I. Definition and objectives of the research project …….. 11

I.1. Introduction …….. 11

I.2. State-of-the-art and uncovered problems …… 11

I.2.1. Examples of degradation process in materials science ……... 12

I.2.1.1. Degradation as a result of mechanical loading ……... 12

I.2.1.2. Degradation as a result of chemical reaction: thermal oxidation 13

I.2.1.3. Degradation occurring during the combination of mechanical loading and chemical reaction: Stress Corrosion Cracking ……... 15

I.2.2. State-of-the-art X-ray tomography …….. 16

I.2.2.1. A technique that responds to the limitations of 2D observations 16

I.2.2.2. X-ray tomography setups ……. 18

I.2.2.3. Recent developments in X-ray tomography ……..... 22

I.2.3. From volumetric image acquisition to material property modelling: a 4 step process illustrated by the study of damage mechanism in a model metallic material ……...……...… 23

I.2.3.1. Step 1: Selection of materials and realisation of experiments …... 24

I.2.3.2. Step 2: Preparation of the image analysis – the volumetric image processing step ……..… 25

I.2.3.3. Step 3: Understanding the image – qualitative and quantitative volumetric image analysis ……... 26

I.2.3.4. Step 4: Comparing experimental results with predictions – the modelling step ……...…… 28

I.2.4. Open or unsolved problems ……. 29

I.3. Objectives and definition of the thesis …… 30

II. 3D Analysis of complicated porosity network in nuclear graphite subject to thermal oxidisation ……..……...…..…… 33

II.1. Context of the study …… 34

II.2. Material description and experimental setup …….. 35

II.2.1. Material …… 35

II.2.2. X-ray tomography setup ……. 35

II.3. Experimental results …… 38

II.3.1. Qualitative observation of microstructural changes due to thermal oxidation ……. 38

II.3.2. Quantitative analysis ……... 40

II.3.2.1. Inclusion segmentation ……... 40

II.3.2.2. Porosity classification …….. 45

II.3.2.2.1. Segmentation of porosity …… 45

II.3.2.2.2. Isolated vs. Continuous: the IB method …….. 47

II.3.2.2.3. Morphology of isolated pores …… 52

II.4. Modelling of thermal property: case of thermal conductivity …….. 56

II.4.1. Considerations……...… 56

II.4.2. Model Description and results …… 56

II.5. Conclusion ……..... 59

III. Bridge ligaments detection in sensitized stainless steel during intergranular stress corrosion cracking ……..…… 61

III.1. Context of the study ……... 61

III.2. Material description and experimental setup ……..…….... 63

III.2.1. Material ……... 63

III.2.2. X-ray microtomography and set-up ……... 63

III.3. Experimental results ……... 64

III.3.1. Qualitative observation of stress corrosion cracking and detection of bridge ligaments …… 64

III.3.1.1. Two dimensional sections of the crack path …… 64

III.3.1.2. Three dimensional visualisation of the crack path ……... 68

III.3.1.3. Conclusion regarding qualitative observations …… 69

III.3.2. Quantitative analysis of bridge ligaments …… 70

III.3.2.1. Which notion describes best a bridge ligament: notion of a hole 70

III.3.2.2. First approach to detect a hole using SS coding: advantages and limitations …… 71

III.3.2.3. Hole closing and filling using a discrete geometry approach …. 74

III.3.2.3.1. Topological notions ……... 74

III.3.2.3.2. Hole closing algorithm ……... 75

III.3.2.3.3. Hole filling algorithm …… 76

III.3.2.4. From a hole to a bridge: considerations and analysis ……..… 78

III.4. Conclusion and future work ……... 80

IV. Effect of lamellar microstructure in titanium alloys during in situ fatigue test ……... 83

IV.1. Context of the study ……... 83

IV.2. Material description and experimental setup ……..……... 85

IV.2.1. Material ……... 85

IV.2.2. Experimental setup …… 85

IV.3. Experimental results ……... 86

IV.3.1. Correlation between lamellar microstructure and mechanical properties: 2D and 3D considerations ……...…… 86

IV.3.1.1. Strain mapping during monotonic tensile test ……. 86

IV.3.1.2. Crack propagation during in situ fatigue test coupled with X-ray microtomography ……... 89

IV.3.2. 2D segmentation of lamellar colonies using texture-based method: ideas and limitations ……....…... 91

IV.3.2.1. Methodology …….. 92

IV.3.2.2. Microscope images …… 96

IV.3.2.3. X-ray microtomography image …… 98

IV.4. Conclusion and future work …….. 100

V. Final conclusions and future work ……. 103

Bibliography ……... 107

Streszczenie ……..... 123

Charakterystyka zawodowa autora ……..…… 124

SUMMARY

This dissertation presents new experimental and computing methodologies to study different degradation processes in engineering materials. This has been done thanks to the unique use of X-ray tomography and the development of new image processing and analysis strategies.

The work consists of four chapters. The first one introduces some of the most frequent degradation processes encountered in engineering materials. It also presents how X-ray tomography has become a competitive and unique tool to study non destructively and in three dimensions these phenomena in the past 10 years. This fact is illustrated in more detail by one example corresponding to the quantification of damage initiation and propagation in a model composite material. This material has been especially fabricated to satisfy the main requirements from X-ray tomography. This example is also used to stress the fact that, despite the uniqueness of the 3D information that is obtained from X-ray tomography, a large proportion of studies remain qualitative because of complicated microstructures or low contrasted images to be studied. This introduces the main message of this manuscript: there is a need to develop image processing strategies so as to extract quantitative information from 3D images.

In this context, the next three chapters are devoted to different challenging studies, both from the materials science and computer science points of view. in the order of presentation, they deal with thermal oxidation in graphite for nuclear applications, intergranular stress corrosion cracking in austenitic stainless steel and propagation of fatigue crack in (α+β) titanium alloys with lamellar microstructure. The author contributed to each of those research areas, both at the experimental and computing level. in each chapter, the results obtained from X-ray tomography are highlighted, with a particular focus on microstructural features that influence the degradation process. Then, the study is put into a computer science context and the novel image processing or image analysis algorithm that has been developed is presented. The last step concerns, when applicable, the study of the results from a materials science point of view, based on the quantitative data obtained thanks to image processing.

This work is interdisciplinary. a great deal of effort has therefore been put in the writing of this manuscript to make it readily comprehensible for both materials and computer scientists who are willing to get more information about the other field of science.

LIST OF ACRONYMS

2D: two Dimensional

3D: three Dimensional

3DXRD: three-Dimensional X-Ray Diffraction microscopy

A3SI: Algorithmes, Architectures, Analyse et Synthèse d'Images

AGR: Advanced Gaz-cooled Reactor

BWR: Boiled-Water Reactor

CCD: charge-coupled device

CED: Computer Engineering Department

CSL: Coincidence Site Lattice

CT: Computed Tomography

CWL: Corrected bulk Weight Loss

DCT: X-ray Diffraction Contrast Tomography

DENIDIA: Development of Excellence in Non Invasive Diagnostic system for Industrial and scientific Applications

DWT: Discrete Wavelet Transform

EBSD: Electron Back Scattered Diffraction

ESIEE: Ecole Supérieure d'Ingénieurs en Electronique et Electrotechnique

ESRF: European Synchrotron Radiation Facility

FBP: Filtered Back-Projection

FEA: Finite Element Analysis

FEM: Finite Element Modeling

FFT: Fast Fourier Transform

FIB: Focused Ion Beam

FSSW: Friction Stir Spot Welding

GCP: Groupe Conception Production

GEMPPM: Groupe de Métallurgie Physique et Physique des Matériaux

hcp: hexagonal close-packed

HMXIF: Henry Moseley X-ray Imaging Facility

HOPG: Highly Oriented Polycrystalline Graphite

IB: Intersected Branch

IGSCC: InterGranular Stress Corrosion Cracking

INPG: Institut National Polytechnique de Grenoble

INSA: Institut National des Science Appliquées

MATEIS: MATEriaux, Ingénieurie et Science

MMSC: Manchester Materials Science Centre

MPC: Materials Performance Centre

NRG: Nuclear Research & Consultancy Group

OM: Optical Microscopy

PCC: Phase-Contrast Crack

PDRA: Post Doc Research Associate

PGA: Pile Grade A

PMMA: Poly(methyl methacrylate)

RBMK: Russian Bolshoy Moshchnosti Kanalniy

ROI: Region of Interest

SDC: Stress and Damage Characterisation

SEM: Secondary Electron Microscope

SKIZ: SKeletization by Influence Zone

TEM: Transmission Electron Microscopy

TUL: Technical University of Łódź

UHSA: Ultimate Homotopic Skeleton Algorithm

USW: Ultrasonic Spot Welding

VHTR: Very High Temperature Reactor

ZS: Zirconia (ZrO_2)-Silica (SiO_2)

I. DEFINITION AND OBJECTIVES OF THE RESEARCH PROJECT

This research work concerns the three-dimensional microstructural modification of different types of engineering materials related to the influence of external conditions which are or may be applied during their servicing, and potentially lead to their decay. The present chapter first introduces background related to typical degradation processes that occur in materials science and the state-of-the-art X-ray tomography. Then, it relates the two together to show that this technique is a very useful tool to characterise various degradation processes. Some limitations, especially in terms of data quantification are also mentioned, which introduce the work presented in this manuscript. in particular, the aim is to reflect the strong bound that exists between 3D image processing and the extraction of microstructural parameters that are key points to the understanding of the materials response to a degradation process.

I.1. Introduction

Any structure is made of one or more materials. The choice of the materials is usually made after listing a set of requirements that the structure should fulfil, including the weight, the price and the resistance to a mechanical/chemical environment [Ashby 2005]. The latter point is a real key issue in industry since it can have a serious economic impact if the structure does not satisfy this requirement in a short time window. Profitability is directly bound to the potential of the structure to last as long as possible, even under serious external working conditions. Since destructive tests are always costly (even though they are necessary), considerable time is usually devoted to justify the choice of a material structure via numerical simulations. However, knowing the microstructure of the material in use (or possible candidate for the structure) and understanding how it behaves during servicing is another key issue. Moreover, it is a valuable input for modelling processes since many sophisticated models require such information so that the properties and, even lifetime of the structure can be predicted.

I.2. State-of-the-art and uncovered problems

The expression "degradation process" is not very common in the materials science community. The damage process is rather more used. However, it is our belief that this expression does not cover all potential effects that a material/structure can undergo in an environment. Indeed, whereas a damage process is mainly associated with a mechanical effect, a degradation process is rather used in a broader sense of the phrase. The word "degradation" refers to "a decline in the appearance, structure, or properties, of a material or substance"

which may be caused either by damage or by environmental conditions. Another way to distinguish both terms is to say that damage can be the result of degradation. The following parts of this chapter describe some of the most common degradation processes found in materials science applications. The aim of this part is not to list all different types of processes which can be defined as part of degradation processes, but mainly those which have been of interest in our past and current research activities.

I.2.1. Examples of degradation process in materials science

I.2.1.1. Degradation as a result of mechanical loading

This type of degradation often occurs during servicing of metallic or ceramic structured materials in aeroengine, nuclear or civil engineering applications. The principal properties which undergo degradation are mechanical properties. The type of degradation is normally related to the type of solicitation, such as constant load (creep), monotonical increase/decrease of load (tensile/compression) or repeated loading (fatigue). The degradation that is introduced to the material is rather referred to as "damage" in the materials science community. The way the structure is loaded also influences the type of failure: axial or multi axial load, bending.

In the case of uniaxial tensile load, the damage of the structure is composed of three steps: creation of new surfaces (initiation step), usually voids, which then increase in size (propagation step) and ultimately merge together (coalescence step), which leads to the total failure of the structured material. One can find a good synthesis of the different steps in numerous references [Monteillet and Moussi 1986; Thomason 1990; Llorca 2000] Usually, the initiation of these degradation events occurs locally within the structure and most of the time it involves the interaction between two phases of the material. Indeed, structured materials usually contain heterogeneities (also called micro heterogeneities due to their micrometer size) which have been deliberately introduced into the material before fabrication or, generated during the strengthening phase, such as mechanical or heat treatment. in both cases, the initial intent is to strengthen the material or generate good properties that the materials assembled together do not originally possess (as in the case of composite materials). It can also occur that unwanted heterogeneities are introduced due to the formation process (small porosities during fabrication processes, microcracks during heat treatments, defects due to machining…). Concerted efforts are made to detect, study and eliminate their potential harmfulness. The apparition of degradation in such structures will usually be of three types: fracture of the heterogeneity, decohesion (debonding) between two phases, or creation of holes in the vicinity of the heterogeneity. The type of degradation is directly dependent on various factors that can be either morphological (shape of heterogeneity, orientation with respect to the

tensile direction, their spatial distribution, etc…) or mechanical ones (internal stress/strain components, interface energy…).

The degradation process caused by fatigue is different. It is mainly governed by cracking which usually occurs at the surface (or in its vicinity). The crack usually propagates towards the other side of the sample and the propagation phase is usually separated into two domains: the short crack domain in which the crack path is strongly dependent on the microstructure, and the long crack domain in which the crack path is less affected by the microstructure. The crack tends to initiate at defects (porosity near the surface, precipitates …) or where the stress concentration is higher, as in the case of a structure containing notches. a lot of factors influence the fatigue- lifetime, including [Vasudevan et al. 2001; Schijve 2009]:

- stress magnitude and stress concentration caused by part geometry,
- quality of the surface: roughness, scratches,
- surface residual stress: if compressive stress is at the surface, it will enhance the lifetime. For instance, this can be introduced before servicing using the laser peening technique [Masaki et al. 2007]. However, unwanted processes, such as uneven cooling, can produce tensile stress which will encourage crack growth,
- material type: some materials such as steel are more resistant to fatigue than others such as aluminium,
- size, frequency and location of internal defects such as porosity or shrinkage voids generated during material fabrication, as it can be found in aluminium cast-alloys [Ludwig et al. 2003],
- grain size: the finer the grain, the longer the fatigue-lifetime.

The interaction with the microstructure is even more pronounced for the so-called short cracks, i.e. cracks which have the same order of magnitude as the microstructure, such as grain size. in recent years, numerous studies have been carried out to characterise such cracks in different metallic materials such as aluminium, steel and titanium alloys. Only few are listed here [Ludwig et al. 2003; Ferrie et al. 2005; Sadananda and Vasudevan 2005; Hoppel et al. 2006; Ferrie and Sauzay 2009; Birosca et al. 2010]. Most of these studies are also good examples of fatigue modelling and comparison with experimental data in terms of crack propagation and crack front shape.

I.2.1.2. Degradation as a result of chemical reaction: thermal oxidation

Oxidation is one of the standard chemical reactions and it corresponds to the process of combining oxygen with some other substance or a chemical change in which an atom loses electrons. When this reaction liberates significant

amounts of heat (exothermic) or requires a massive amount of heat to proceed (endothermic), one speak of thermal oxidation. The thermal oxidation process may be used in microtechnology to produce a thin layer of oxide (usually silicon dioxide) on the surface of a wafer (semiconductor). in that case, the process is thoroughly controlled and the oxidizing agents are selected depending on the process (dry oxidation with molecular oxygen, wet oxidation with water vapour). However, in many cases, the thermal oxidation will occur during the material servicing and may contribute to the degradation of the structure, especially if it is subjected to high temperatures. The reaction is especially prejudicial in the case of materials composed of carbon since the reaction between carbon and oxygen is exothermic and thermodynamically favoured [Kelly et al. 2000]. Graphite is therefore a type of material which can be prone to thermal oxidation if the structure is porous. This is of crucial importance since graphite is used in a variety of nuclear reactor types; principally as moderator, reflector, fuel sleeve and fuel tube materials. The oxidising environments of special interest are air (oxygen), carbon dioxide and steam (water).

The oxidation process can be described as a series of physical and chemical steps:

(i) Transport of oxidant to the graphite surface.

(ii) Adsorption of oxidant onto the graphite surface (physisorption[1]).

(iii) Formation of carbon-oxygen bonds (chemisorption[2]).

(iv) Formation of carbon-hydrogen bonds in reduction reaction.

(v) Breaking of carbon-carbon bonds.

(vi) Desorption of carbon monoxide, or other product.

(vii) Transport of reaction products away from the graphite surface.

Obviously, the reaction takes place in the porous body of graphite and most of the oxidation is the result of species activated in the open porosity. The oxidation rate will therefore be directly linked to the desorption of carbon monoxide (step (vi)); hence the decrease of the number of carbon atoms at the porous superficial surface and the increase in the porosity volume. It is a standard convention to correlate oxidation with weight (or mass) loss.

---

[1] Physisorption or physical adsorption is a type of adsorption in which the adsorbate adheres to the surface only through Van der Waals (weak intermolecular) interactions.

[2] Chemisorption or chemical adsorption is a type of adsorption in which a molecule adheres to a surface through the formation of a chemical bond, as opposed to the Van der Waals forces which cause physisorption.

It is highly improbable that the thermal oxidation rate will occur evenly at the pore surface since studies [Johnson et al. 1982; Kelly et al. 2000] have shown that:

- Different parts of the structure may react at different rates; the binder being more reactive than the grist particles (see presentation of the material and microstructure in Section II.2.1).
- Edge atoms are more reactive than basal plane atoms.
- It may also be the case that the gas composition varies in non-transport pores.
- Effect of a given gas composition varies with pore shape.

The degradation, which is mainly linked to the evolution of the porosity network, is responsible for property changes of the material. For instance, this reduces thermal conductivity as well as Young's modulus and strength. The ability to characterise the oxidation induced evolution of the porosity network and correlate it with changes in thermal conductivity is important for the understanding of the core component thermal behaviour. This can be done by experimental means but also using analytical or numerical modelling. For instance, since the pioneering studies carried out by Maxwell in the 19th century on electric conductivity (summarised by Euler [Euler 1957]), a large number of analytical models have been proposed in literature to estimate the effective thermal conductivity based on porosity [Euler 1957; Knudsen 1959; Meredith and Tobias 1962; Schulz 1981; Rice 2005]. Experimental characterisation of the porosity network is therefore essential for both experimental and simulation studies.

I.2.1.3. Degradation occurring during the combination of mechanical loading and chemical reaction: Stress Corrosion Cracking

In several applications where a structure is subjected to loading, the degradation process is not directly initiated by the mechanical loading itself, but rather by its combined effect with the environment. Unless an application is designed to run in a vacuum chamber, the environmental conditions surrounding the structure may have an undesired effect on its properties. For instance, liquid and/or gas in pipelines can damage structures, usually by corrosion, a chemical reaction which corresponds to the loss of an electron of the metal reacting with water and oxygen. Corrosion involves two chemical processes: oxidation and reduction.

Corrosion can be concentrated locally to form a pit (hole) or crevice, or it can extend across a wide area to produce general degradation. Because of its high economic impact, a lot of solutions have been proposed to limit corrosion, including passivation, special surface treatments, corrosion inhibition and cathodic protection [Davis 2000]. The former solution corresponds to the

spontaneous formation of a hard non-reactive surface film that prevents further corrosion. It is commonly used to protect metals like aluminium, stainless steel or titanium exposed to water or air at moderate pH level. However, this strength can also be their weakness since local passivity breakdown can occur, especially in the case when the thin layer is not uniform in thickness or contains defects. Under favourable corrosion conditions, this can lead to pitting or intergranular corrosion, essentially due to local depletion of the elements of some alloys. For instance, in the case of austenitic stainless steel, chromium depletion occurs as a result of chromium-carbide precipitation [Gertsman and Bruemmer 2001]. The depletion will mainly occur at the grain boundary, which will lead, in the case of austenitic stainless steel, to intergranular corrosion rather than pitting. If the structure is under load, cracks will initiate at these local sites and then propagate at a very high rate until failure of the structure occurs. in the case of austenitic stainless steel, the crack will propagate between the different grains composing the microstructure of the alloy (in other words, at the grain boundaries). This type of degradation process is called intergranular stress corrosion cracking. Microstructural studies have shown that the crack could be better controlled by producing a specific microstructure, and more specifically by controlling grain boundaries. Indeed, by applying special mechanical heat treatment, one can facilitate the growth of special grain boundaries with low misorientation (low CSL) that are more resistant to cracking than their counterparts [Lin and Pope 1993; Trillo and Murr 1999; Gertsman and Bruemmer 2001; Shimada et al. 2002]. These special grain boundaries can delay the overall failure of the material by locally bifurcating, then stopping the crack, or create the so-called bridge ligaments. However, very few studies have focused on the characterisation of these features, especially the latter one, because they can be confounded with simple crack bifurcation in 2D observations. Three dimensional characterisation, if possible carried out in situ, is therefore needed.

I.2.2. State-of-the-art X-ray tomography

I.2.2.1. A technique that responds to the limitations of 2D observations

As it has been mentioned above, the microstructure plays a fundamental role in the degradation process in structured materials. The correlation between the two is never straightforward to identify, hence an experimental analysis of such correlation is in most cases necessary before considering an analytical/numerical prediction of the phenomenon. One of the most popular techniques to study the influence of the microstructure on the degradation process is imaging, microscopy imaging being the most frequently employed. a wide range of instruments have been developed for decades to cover a range of scale that goes from the millimetre scale (using OM) down to the nanometre scale (using TEM). The possibility of coupling surface observations with in *situ* experiments allows one to observe the microstructure changes with the degradation process

in "real time". This often provides a good insight into the phenomenon studied, usually qualitative, but these 2D microscopy techniques suffer certain drawbacks:

- Problem with sample preparation. a necessary condition to use these techniques is to have a mirror-like surface, usually after prior manual or electro-polishing. However, this can be problematic when the sample is very fragile or when the surface presents defects like holes, which can play a fundamental role in the understanding of the degradation process. in the latter case, the polishing step may plug them, especially if the material is relatively ductile, which can dramatically hinder the study of the degradation process.
- Problem with quantification. Studies have shown that surface analysis may result in a quantification which shows discrepancy in the results obtained for the bulk of the sample. For instance, damage can be studied from surface observation during in situ tensile tests. It has been shown that the information obtained, although valuable qualitatively, can be misleading quantitatively because of effects of the surface on the stress field [Buffiere et al. 1999]. Some methods, such as stereology, serve to extract 3D quantification from 2D observations. This particular method, however, cannot provide valuable results linked to connectivity or tortuosity in the case of a complex microstructure. For instance, in porous materials, one phase – the pores – may form very tortuous channels within the microstructure. With 2D observations, two branches of the same pore, observed on the surface, could be interpreted (after the image processing and analysis) as separated features.

These drawbacks can be avoided using X-ray tomography, an imaging technique which allows one to perform three dimensional and non-destructive observations of the microstructure. Initially developed for medical applications in the 1970s, X-ray tomography has gained in popularity in the last decade with the emergence of its applications in other fields of science, including earth science, biology and materials science. This is mainly due to large improvements of the systems, especially in terms of spatial resolution and X-ray detectors. As a matter of fact, a traditional CT scanner has a typical spatial resolution of 2-5 mm, whereas the new generation of X-ray tomography systems have a spatial resolution in the order of the micrometer scale, and even below (0.3-0.7 μm). This is mainly due to the use of 3rd generation synchrotron radiation sources and the development of high-tech detectors. a simple search in a scientific database[3] shows that the number of articles related to materials science applications has increased dramatically, from less than 50 in the 80s to 900 in the last decade. The applications have also spread beyond the boundaries of synchrotron facilities with the commercialisation of laboratory

[3] Website link: www.scopus.com (website consulted 14th July 2010).

X-ray systems. An X-ray tomography system is therefore becoming routine equipment for materials science investigations, just as SEM and TEM. a good example to illustrate: the University of Manchester has recently inaugurated the HMXIF[4] which is equipped with 5 different X-ray tomography instruments, allowing experiments on various scales of samples (from the centimetre scale down to the nanometre scale) and weight, and covering different fields of science (from biomedical to palaeontology and, obviously, materials science).

Nowadays, most of all different types of materials have been tested with the help of X-ray tomography and citing all of them would be endless. Nevertheless the most important researchers that have popularised the technique in the last decade can be acknowledged, and especially those related to metallic materials. The team from INSA-Lyon (France), led by Prof. J-Y Buffiere and Prof. E. Maire was one of the first to investigate damage mechanisms in metal matrix composites and in metallic foams [Buffiere et al. 1999; Babout et al. 2001; Buffiere et al. 2001; Maire et al. 2003]. At the same time, in the same region, a team from INPG (Grenoble, France) investigated semi-solid materials [Martin et al. 2000; Limodin et al. 2007]. It was also in this period that studies on damage mechanisms in engineering metallic materials started to develop at the University of Manchester in collaboration with INSA-Lyon [E. Maire et al. 2001; Preuss et al. 2002; Mcdonald et al. 2003; Sinclair et al. 2004]. Most of these experiments were carried out with synchrotron facilities, but since then, with the development of laboratory kits, the number of studies has considerably increased. There have been works performed on foams [Mcdonald et al. 2006; Maire et al. 2007], ceramics matrix composites and cements [Douarche et al. 2001; Rattanasak and Kendall 2005; Elaqra et al. 2007; Morales-Rodriguez et al. 2009], polymers [Montminy et al. 2001; Shen et al. 2004; Miyoshi et al. 2008; Fischer et al. 2009; Wismans et al. 2009] and of course metallic materials [Gonzalez et al. 2000; Hamilton et al. 2002; Kadar et al. 2004], to mention a few.

I.2.2.2. X-ray tomography setups

In general terms, the concept of a third-generation computed tomography system typically includes an X-ray source and an X-ray detector situated on the opposite side of the object of interest. in medical applications, the X-ray source and the detector are diametrically mounted on an annular disk which rotates around the patient, while the systems of interest (synchrotron and laboratory X-ray tomography) are more flexible with the possibility of both translating the sample and the detector, as shown in Figure I-1a. With the use of a cone beam, this has the advantage of changing the magnification of the image: the closer the sample to the X-ray source, the higher the magnification. in that case, spatial resolution

[4] Website link: http://www.materials.manchester.ac.uk/research/facilities/moseley/

is governed by the size of the X-ray source because of penumbra effects. Other systems, such as synchrotron X-ray tomography, mainly use a parallel beam (see Figure I-1b), which implies that without additional setup, no magnification change is possible. However, the spatial resolution can be tuned using different types of detector. An X-ray detector usually consists of a scintillator which converts X-rays to visible light, and an optical system which projects the photon beam to a CCD camera.

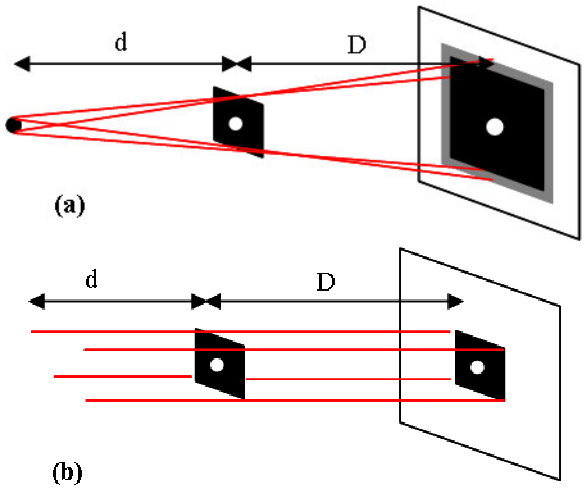

Figure I-1. Schematic illustration of projection systems. (a) cone beam (b) parallel beam

In both configurations, radiographs (i.e. projection images over the detector which correspond to the absorption/attenuation of the X-rays by the sample under investigation) are acquired at different angle steps, A, in the range of sample rotation between 0 and π. The number of radiographs, Nr, is therefore equal to:

$$Nr = 180/A \qquad \textbf{Eq. I-1}$$

for a parallel beam and

$$Nr = (180 + FA)/A \qquad \textbf{Eq. I-2}$$

for a cone beam which takes into account the fan angle FA, i.e. the angular spread of the X-ray beam to "illuminate" the scintillator area. The set of radiographs are then used to reconstruct the volume of the material under investigation using the FBP algorithm [Feldkamp et al. 1984; Kak and Slaney 1987].

Figure I-2 and Figure I-3 show the synchrotron X-ray microtomography[5] system of the ID19 beamline at the ESRF (France) and a laboratory system developed by X-Tek and which used to be owned by the SDC unit of the MMSC (the School of Materials – The University of Manchester, UK), respectively. These systems are roughly representative of the current technology. The results presented in this dissertation have been acquired with the use of these two systems.

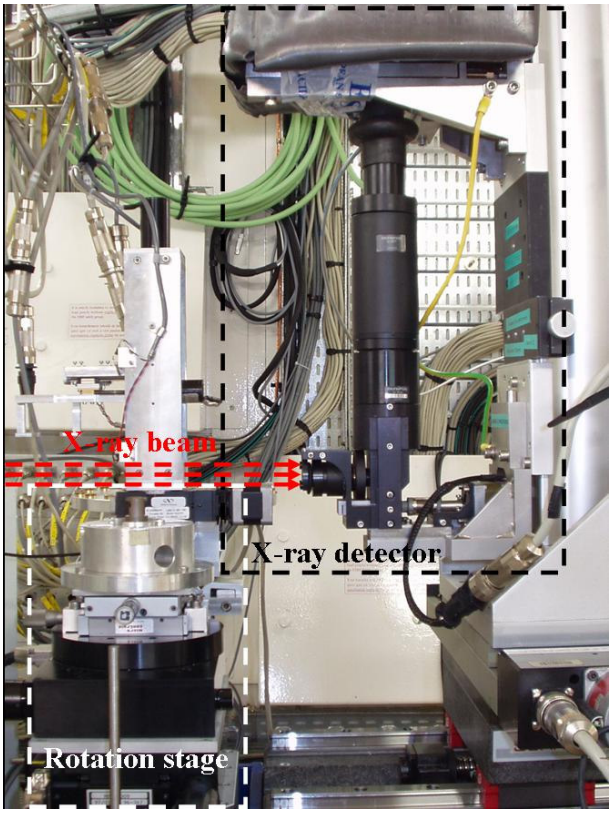

Figure I-2. Lateral view of the X-ray tomography setup developed at ID19 beamline (ESRF). Picture taken by the author with consent of the equipment's owner (i.e. ID19 beamline; head of Unit: dr J. Baruchel)

[5] Microtomography means that the spatial resolution of the system is of the order of the micrometer scale (i.e. between 0.5 to 5 μm).

Figure I-3. X-tek HMX X-ray tomography system. (a) lateral view of X-ray gun and rotation stage showing schematic representation of X-ray cone beam (b) general view of the hutch (c) detectors (aluminium / beryllium scintillators coupled with 1024x1024 CCD camera). Pictures taken by the author with consent of the equipment's owner (i.e. SDC-MMSC; head of Unit: Prof. P.J. Withers)

Table I-1 shows typical examples of setups used with these two systems during experiments that will be discussed later in chapters II and III, i.e. with graphite and stainless steel samples, respectively. Normally, a higher resolution involves a larger set of radiographs to be backprojected in order to minimize the error in the reconstructed image as we go away from the centre of the detector during the interpolation process [Kak and Slaney 1987]. The exposure time is directly linked to the energy and flux of the X-ray beam that arrives at the detector. Between the X-ray source and the detector, X-rays have been absorbed by the sample and this absorption is governed by the Beer-Lambert law:

$$N_i(E) = N_0(E)e^{-\int_{\Delta s}\mu_E(s)ds} \qquad \textbf{Eq. I-3}$$

where $N_0(E)$ and $N_i(E)$ are the numbers of incident and transmitted photons for beam energy E, respectively, and $\mu_E(s)$ is the local attenuation coefficient along a straight line path s between the X-ray source and a point in the scintillator plane. One can see that with the use of the FBP algorithm, the reconstructed volumetric image is a direct signature of local attenuation coefficient of the material. The local attenuation coefficient depends on the local composition and the energy of the incident beam. in the photoelectric domain (E < 200 keV), the attenuation coefficient follows the expression below [Attix and Roesch 1968]:

$$\mu_E = \frac{\kappa\rho Z^4}{E} \qquad \textbf{Eq. I-4}$$

where κ is a constant, ρ and Z are the local density and atomic number, respectively. This law assumes a monochromatic beam (constant energy). In the case of a polychromatic beam, the average energy has to be integrated over the full energy spectrum of the X-ray incident beam. One can easily see from the above equation that the attenuation of the beam is highly dependent on the atomic number of the material: a heavy material such as steel absorbs far more X-rays than light alloys, such as aluminium, or carbon materials like graphite. For the former material, a higher energy and a longer exposure time are usually the necessary conditions to have enough flux travelling through the material. However, two extreme conditions have to be disregarded while setting the energy level of the X-ray beam and exposure time: the material is either too opaque or too transparent to the X-rays. The contrast of the reconstructed images is normally considered satisfying if the ratio $N_i(E)/N_0(E)$ in Eq. I-3 is between 20 and 50 %. If more than 80% of the beam is absorbed by the material, it is considered opaque to the X-rays and the reconstructed volumetric image is too dark. Inversely, if less than 50% of the beam is absorbed by the material, it is considered nearly transparent to the X-rays and then again, a problem will occur during image processing and data analysis.

Table I-1. Typical tomography parameters for the two setups. S: sample type – BT: X-ray beam type – E: X-ray energy – R: resolution – t: acquisition time / radiograph – A: rotation step – Nr: number of radiographs – Nf: number of frame/radiograph – T: scan duration

S	XCT	BT	*V(kV)* / E(keV)	R(µm)	t(s)	A(°)	Nr	Nf	T(min)
Graphite	X-Tek	Polychromatic cone beam	*25-225*	13	0.16	0.3	620	32	~50
Stainless steel	ID19	Monochromatic parallel beam	10-60	0.7	1.5	0.12	1500	1	~50

I.2.2.3. Recent developments in X-ray tomography

In recent years, a series of new techniques and setups has emerged to compensate some drawbacks of the classical X-ray tomography techniques. They include phase-contrast tomography [Cloetens et al. 1997] and the derived holotomography [Cloetens et al. 1999], DCT [Johnson et al. 2008; Ludwig et al. 2008] and X-ray nanotomography [Withers 2007]. All these techniques are mainly concerned with increasing the level of information by obtaining better image quality, providing extra information on crystallography in polycrystalline materials or increasing the spatial resolution down to the nanometer scale.

Phase-contrast tomography simply involves setting the distance from the sample and the detector so that it is large enough to generate the so called Fresnel diffraction fringes. These correspond to phase jumps related to the interface between two materials even when these phases show very similar x-ray attenuation, such as in the case of Al and Si in Al/SiC composites [Buffiere et al. 1999]. By recording a few scans at different sample-to-detector distances and combining them back, the so-called X-ray holotomography scan is obtained that reveals different phases of a material with similar density as if a strong X-ray attenuation occurred. This technique has demonstrated its usefulness in the case of studying the elastic-plastic response of aluminium matrix composite reinforced with Al_2O_3 particles [Kenesei et al. 2005]. Despite the simplicity of the setup, both methods imply that the X-ray beam should be coherent and monochromatic, which restricts its use to synchrotron tomography.

Recent advances in synchrotron based X-ray imaging and diffraction techniques have offered interesting new possibilities for mapping 3D grain shapes and crystallographic orientations in different classes of polycrystalline materials. DCT is a monochromatic beam imaging technique combining the principles of X-ray micro-tomography and 3DXRD. DCT provides simultaneous access to 3D grain shape, crystallographic orientation and attenuation coefficient distribution at the micrometer length scale, on condition that there is absence of orientation and strain gradients inside the grains. The technique has already shown evidence of its usefulness to study grain coarsening in titanium alloys [King et al. 2010] or intergranular stress corrosion cracking in stainless steel [King et al. 2008].

Nowadays, devices have been developed to reach nanometer scale resolution as reviewed in [Withers 2007]. Despite promising prospects, especially in the field of biomaterials and micro-electronics, the technique is still barely used in materials science, mainly due to the sample size constraint (less than 100 μm), but also because of a low level of X-ray energy (<20 keV) and a long acquisition time (typically a week). However, one can cite recent works performed on porous media materials that used such a technique [Li et al. 2009; Ostadi et al. 2010].

I.2.3. From volumetric image acquisition to material property modelling: a 4 step process illustrated by the study of damage mechanism in a model metallic material

The work presented in this section is an exemplar of a *model* particle-composite material use to study and to model initiation and growth of damage using X-ray microtomography. This type of material is usually called a *model material* since it is designed to represent a simplified microstructure of engineering materials. The microstructure is usually enlarged and controlled as much as possible to facilitate the observation and the study of the degradation phenomenon.

The materials are not fabricated and optimised for performance, but rather for research purposes, thereby researchers always keep in mind that the phenomena studied can be beneficial to optimise engineering materials. It is also a perfect example to illustrate a case study where quantification from 3D images is unambiguous owing to the image processing step which is greatly facilitated and simplified by a thorough selection of materials. Indeed, this results in highly contrasted and detailed images. Most of the results presented in this section have been published in [Babout et al. 2001; E. Maire et al. 2001; Maire et al. 2002; Babout et al. 2003; Babout et al. 2004c].

I.2.3.1. Step 1: Selection of materials and realisation of experiments

Since the aim of the study was to use 3D approach to revisit general analytical and numerical techniques that predict damage initiation and propagation in metallic materials, the different phases of the model metallic material had to be carefully chosen. This was crucial to satisfy both mechanical and physical requirements set by the type of damage to be visualised/analysed (i.e. particle cracking/debonding) and the tool used to achieve that goal (i.e. X-ray tomography). Therefore, model composites have been fabricated by a powder metallurgy route [Maire et al. 2002]. Two types of aluminium matrices were chosen, Al and Al2124, that exhibit different mechanical properties: the former being more ductile, while the latter presenting a larger tensile strength. They were mixed with two different volume fractions of hard and large spherical ZS particles, namely 4 and 20%. The size of particles was screened between 40 and 60 μm in order to make them 20-30 times larger than the spatial resolution of the microtomography system (2 μm). This combination was a good consensus between sufficient attenuation contrast for X-ray tomography investigation and satisfying mechanical incompatibilities to generate particle damage.

In situ monotonic tensile tests coupled with synchrotron X-ray microtomography were carried out at ID19 beam line on different samples fabricated with the two types of matrices and volume fractions mentioned above. a view of the tensile device used for the experiments is shown in Figure I-4. It is worth mentioning that this machine was specially designed[6] more than a decade ago for X-ray tomography experiments and it is still frequently in use. Typical results are presented in the following sections.

[6] The owner is the MATEIS laboratory, formerly known as the GEMPPM laboratory (INSA-Lyon, France).

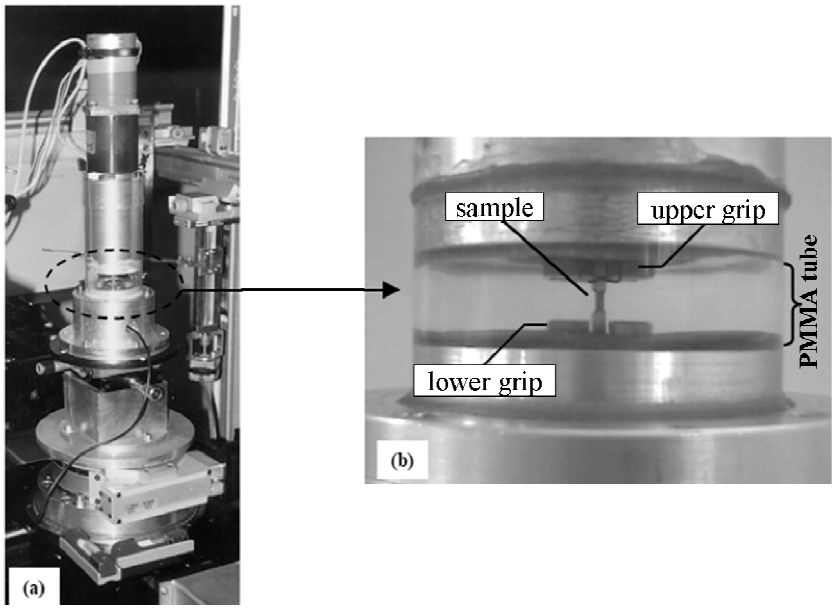

Figure I-4. (a) General view of the machine installed on the goniometer of ID19 microtomography beamline at ESRF to study in situ damage process during monotonic loading. (b) Zoomed view around the PMMA tube

I.2.3.2. Step 2: Preparation of the image analysis – the volumetric image processing step

The choice of materials greatly facilitated the volumetric image processing, especially the segmentation of the different phases, e.g. the matrix (Al or Al2124), the particles (ZS) and voids (air). This is illustrated in Figure I-5 which shows the strong difference in the intensity level between the different phases. This has allowed one to unambiguously select a segmentation threshold. Morphological parameters of the particle and voids generated during damage process were important to characterise, including particle size and shape distribution, the particle volume fraction (both global and local) as well as the size and volume fraction of damage-induced voids.

The local volume fraction of particles was characterised using the SKIZ method [Russ 1995] as shown in Figure I-5c. Since particles had to be analysed separately for statistical purposes, it was crucial to separate any particles in contact, especially in materials with 20% volume fraction. This was done using a watershed even if it appeared that over-segmentation did occur, especially in elongated particles and large clusters of connected particles. This resulted in flooding edges which did not correspond systematically to the correct contact surface between the particles. in that case, manual separations were carried out.

The different image analysis results obtained from these 3D images concluded that the composites fabricated satisfied the requirement specified by the context of the study. For instance, it was verified that the local reinforcement volume fractions were found to be 4.7% ± 2.3% and 19.8% ± 7.0% for the composites reinforced with 4% and 20% of ZS, respectively.

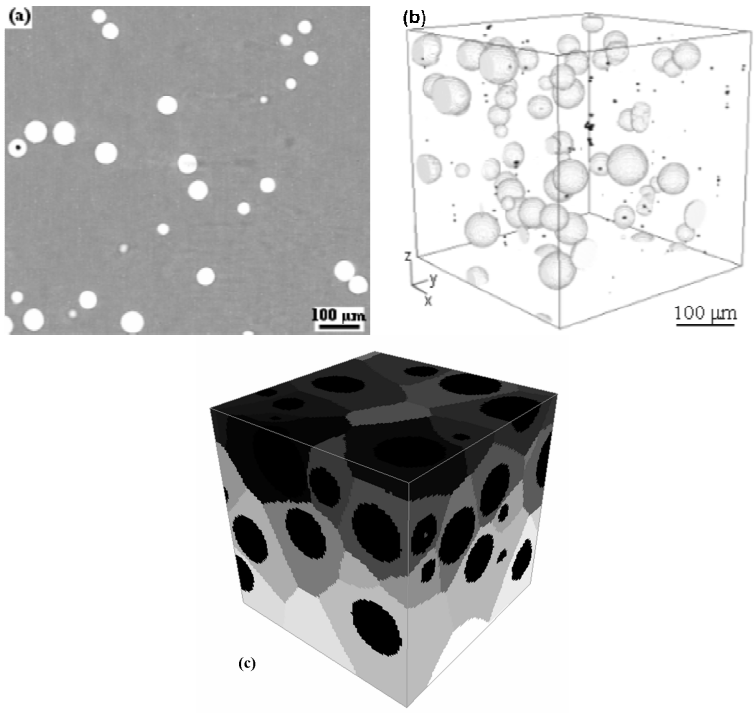

Figure I-5. (a) Reconstructed images of an internal section of the model material Al2124 + 4%ZS at the initial state. (b) Corresponding 3D rendering of the reconstructed volume. The matrix has been removed in the picture. Black spots correspond to pre-existing holes formed during extrusion of the material. (c) 3D representation of the SKIZ for material with 20% of particles. Figures (a) and (b) published in [Babout et al. 2004c]

I.2.3.3. Step 3: Understanding the image – qualitative and quantitative volumetric image analysis

From a qualitative point of view, Figure I-6 and Figure I-7, which present the same reconstructed images at different deformation steps of Al + 4%ZS and Al2124(T6) + 4%ZS, respectively, depict unambiguously three different phases of damage, e.g. initiation, growth and coalescence. The types of mechanism differ for the two materials: decohesion mainly occurs in the soft matrix material (Al+4%ZS), while the main failure mechanism is particle fracture in the hard matrix material (Al2124+4%ZS). It is noteworthy that the

same trend was observed in a corresponding matrix reinforced with 20% of ZS particles. The qualitative analysis of Figure I-6 also shows that some pre-existing cavities at the particle/matrix interface start to grow when the critical strain is attained (Figure I-6b-d). This phenomenon corresponds to a growth threshold (a pre-existing void which starts to grow during the tensile test). This result confirms what was already presented and discussed in an earlier paper [Babout et al. 2001]. At that time, it was concluded that in these model materials the growth threshold could be regarded as an initiation threshold. While the damage sites were found to be uniformly distributed along the sample z-axis, coalescence, as expected, occurred locally in the region of the highest strain, e.g. in the necking region. This is clearly evident owing to the strain gradient curves adjoined to Figure I-6d-e and Figure I-7d. All these results also confirm those observed using microscope imaging.

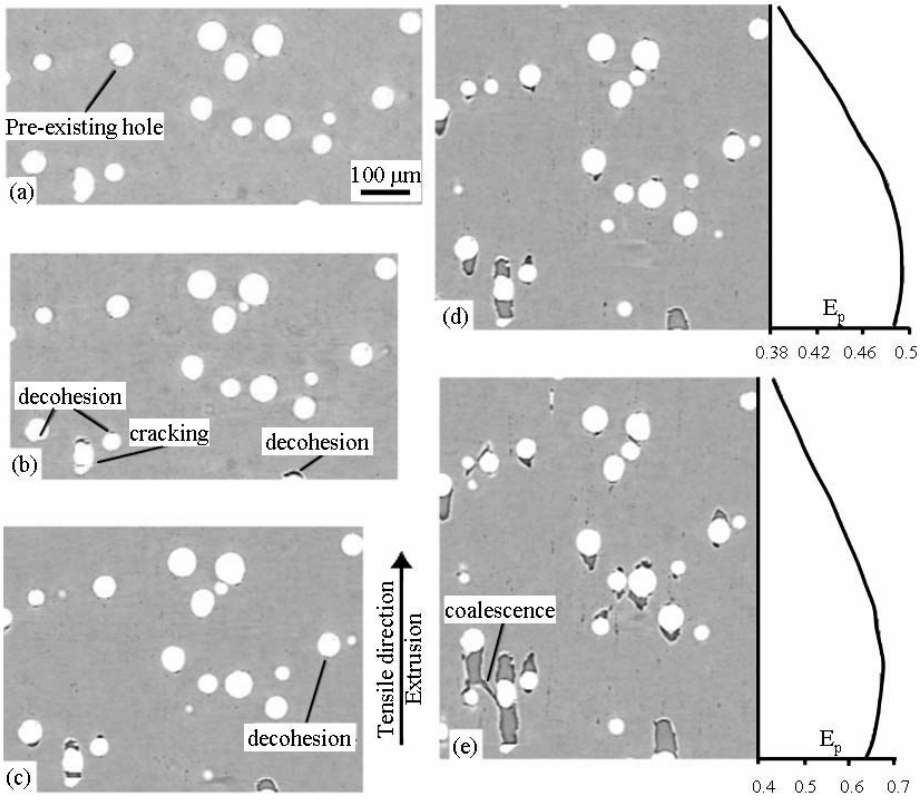

Figure I-6. Reconstructed images of the same internal section of the model material Al + 4%ZS at five different relevant plastic deformation steps (a) initial state; (b) Ep = 0.13; (c) Ep = 0.28; (d) ‹Ep› = 0.42 (necking); (e) ‹Ep› = 0.60 (necking). When necking occurs plastic strain gradient curves, obtained using the sample section profile, are given with the corresponding images. Figures published in [Babout et al. 2004c]

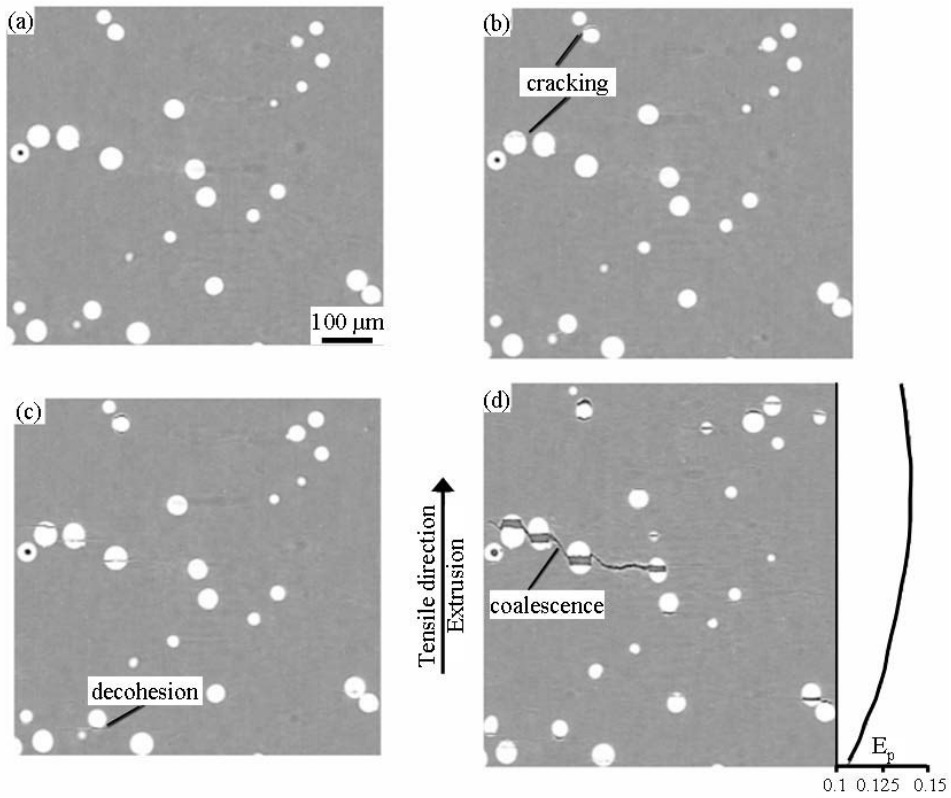

Figure I-7. Reconstructed images of the same internal section of the model material Al2124 + 4%ZS at five different relevant plastic deformation steps (a) initial state; (b) Ep = 0.030; (c) Ep = 0.052; (d) ‹Ep› = 0.126 (necking). a plastic strain gradient curve, obtained using the sample section profile, is given with the last image to convey the presence of necking in the sample. For the last step, the angle bracket refers to an average value of the plastic strain. Figures published in [Babout et al. 2004c]

The data obtained from the tomography scans were used for quantitative analysis. It was focused on the separated effects of matrix hardness and particle volume fractions on the evolutions of numerical and volume fractions of damaged particles as a function of the plastic strain [Babout et al. 2004c]. The growth of damage in soft matrix composite reinforced with 4% of ZS particles was also studied, both locally and globally, in 3D. It was also compared with the analytical model [Babout et al. 2001], as presented in the next sub-section.

I.2.3.4. Step 4: Comparing experimental results with predictions – the modelling step

The data obtained in the study presented could be unambiguously used or compared with analytical and numerical models due to the marked contrast

between the different phases. Indeed, the volume of the voids created by particle debonding in Al+4%ZS could be easily selected using a simple histogram-based segmentation, followed by labelling. The evolution of the volume expansion as a function of the plastic strain could be compared with classical and modified Rice and Tracey models for the first time [Babout et al. 2001]. Another prediction has combined experimental results: Weibull statistic and finite element modelling to compute different local fields, in the particle and along its interface with the matrix (e.g. average normal stress in the particle, the maximum hydrostatic stress at the particle/matrix interface). They were calculated to correspond to specific uniaxial deformation for which the initiation of damage by particle cracking and particle/matrix decohesion were observed [Babout et al. 2004c]. The different experimental results obtained for the different materials in use also guided the development of a simple analytical model. The aim was to predict the type of damage (i.e. particle cracking or debonding) based on mechanical characteristics of both phases, i.e. matrix and particles [Babout et al. 2004a].

I.2.4. Open or unsolved problems

The example presented in the previous section is among the "best case scenarios", where the quality of the 3D images, together with the relative simplicity of the material microstructure, greatly facilitate the study of degradation and its correlation with the microstructure. Similar examples can be found in the literature, such as studies on model fibre composites [Preuss et al. 2002; Mcdonald et al. 2003; Sinclair et al. 2004; Schilling et al. 2005] or particle composites [Weck et al. 2008a; Weck et al. 2008b]. Most of degradation studies that involve the use of X-ray tomography concerns the development of damage and appearance of new surfaces, i.e. cracks or debonding. The segmentation of these surfaces is usually facilitated by the good attenuation contrast with the microstructure, except at early stages when their width can be lower than or of the same order of magnitude as the spatial resolution. It has been mentioned earlier that phase contrast can help in that respect (see Section I.2.2.3). However, a large number of contemporary degradation studies face the following problems:

- the X-ray tomography of materials can give rise to reconstructed images which are very difficult to analyse. This can be caused by poor contrast between phases due to absorption coefficients of the same magnitude (e.g. fibre composites, particles and matrix or phases in an alloy [Maire et al. 2008; Sumita et al. 2010; Wright et al. 2010]) or within phases, especially in the less absorptive one, if the absorption coefficients differ too much. Poor contrast can be also the result of spatial resolution of the system not adapted to microstructural features such as inclusions in alloys [Zhang et al. 2009].

- the other main challenge is simply due to complex microstructures that are difficult to apprehend in 3D [Hodgkins et al. 2006; Birosca et al. 2010].
- the problem to solve is even more challenging when the previous problems are combined. It is sometimes neither possible to improve the quality of the image because of physical limitations, nor to fabricate a simplified version of the material to facilitate its study and the degradation process associated with it.

In the case of the previous limitations, the study is frequently limited to a qualitative investigation of the images and when performed quantitatively, it is often done manually and without the help of advanced image processing algorithms. Moreover, in a large number of studies, the quantitative analysis of degradation processes mainly focuses on the apparition of new surfaces, but rarely correlates them to the microstructure [Proudhon et al. 2006; Maire et al. 2008; Turnbull et al. 2009; Zhang et al. 2009; Sumita et al. 2010]. This is usually linked to the difficulty to reveal microstructural features using X-ray tomography because of the first problem mentioned above. Without the help of other characterisation methods, this may constraint the general understanding of the phenomenon.

In general, materials scientists mainly use a histogram-based segmentation method or other methods that are part of an imaging software package to isolate new surfaces from the rest of the tomography data. in many cases, the method is sufficient to quantify the degradation process. However, the investigation may be difficult to be carried on further, especially to characterise feature shapes and to correlate them to the microstructure. a lot of image processing approaches have been developed and presented in many books [Serra 1982; Russ 1995; Nikolaidis and Pita 2001; Soille 2003; Petrou and Garcia Sevilla 2006] and articles [Kong and Rosenfeld 1989; Mallat 1989; Niblack et al. 1992; Pal and Pal 1993; Hyvarinen and Oja 2000; Abramoff et al. 2004; Sezgin and Sankur 2004] to cite a few. Nevertheless, they are unknown most of the time to materials science researchers, who have little background in image processing. There is also little evidence that they collaborate with image processing specialists. Therefore, there is a need for more interdisciplinary connections as materials science and computer science researchers share a common interest in X-ray tomography data.

I.3. Objectives and definition of the thesis

The aim of this scientific project is to show evidence that the previous problems, i.e. low contrasted images or challenging microstructures, can be treated using dedicated 3D image processing and analysis algorithms. This is illustrated by three different examples of degradation processes. It is worth mentioning that the experimental parts of the different works at the moment of their studies were

unique since they were the first ones carried out using X-ray tomography. The case studies which illustrate how these problems have been solved are presented, according to our judgement, from the simplest to the most complicated work, in terms of image handling. This does not mean that the analysis of the degradation process, which is also presented in the different examples, is in the same order.

The main aim of the project is to present the qualitative analysis of the degradation phenomena and their interaction with the microstructures studied. Then, after the microstructural features that influence the degradation process have been identified, the study is put into a computer science context. The novel image processing or image analysis algorithm that has been developed for further materials science characterisation is presented. It is worth mentioning that new algorithms have been developed, all based on advanced image processing and analysis concepts. All the cases presented also show the evidence of interdisciplinary connections between computer science and materials science, thanks to the use of X-ray tomography, for the better comprehension, as in our case, of degradation in engineering materials. It should be borne in mind that this can also be extended to other applications.

This dissertation will first present two different cases where the main limitation is linked to challenging microstructures and whose solutions, in terms of image processing or analysis, have been considered in order to allow the quantification of the degradation phenomena that take place in these engineering materials. The first example concerns the study of thermal oxidation in graphite used in the nuclear industry. The second one deals with the study of intergranular stress corrosion cracking in stainless steel, a type of metallic material widely used in the nuclear industry.

Finally, the author presents the recent work which actually marks, within the presentation of these examples, the most challenging situations that has been faced so far, where the two main limitations listed in the previous section are combined, i.e. poor contrast and complicated microstructure. This generates a set of 3D images that are very difficult to tackle. This part will present preliminary results on the image processing of 2D images and the possible methods to be considered in the future.

II. 3D ANALYSIS OF COMPLICATED POROSITY NETWORK IN NUCLEAR GRAPHITE SUBJECT TO THERMAL OXIDISATION

The state-of-the-art example detailed in the introduction chapter presented a perfect example of a highly contrasted 3D image due to a large difference of density between the components of a metallic material and a well-defined porosity network. Even though this condition is highly desirable, it is not possible to satisfy it for all the experiments which involve X-ray tomography imaging. and to be more precise, the previously presented case can be considered an exception.

The main reason is that most of the materials are the so called engineering materials, with the aim to exhibit special properties for the type of servicing conditions they are exposed to in real life. It is sound to think that these materials are not designed to primarily fulfil the requirements of the X-ray tomography. It is rather the matter of the following questions that must be answered: does my material exhibit the physical and microstructural properties which are suitable for X-ray tomography imaging?

Graphite, the engineering material presented in this chapter, partly satisfies the requirements of X-ray tomography. As one will see, the study is hindered by two factors. Since graphite is a very low density material (~2.26 g/cm^3 for solid graphite), the contrast between porosity and carbon is not as high as it could be expected. Moreover, the material, even though composed of only one basic element, Carbon, has a very complicated microstructure, especially in terms of the porosity network, which spans from pores of a nanometre scale to very large cavities of the order of a few hundred micrometers.

In the following chapter the strategy that was used to analyse the porosity network is presented, which is known to play a fundamental role in graphite mechanical and thermal properties. Everything is put into the context of the study which aims to investigate the behaviour of such materials in nuclear reactors. This is a summary of results presented in various papers [Babout et al. 2005; Babout 2006; Babout et al. 2006b; Babout et al. 2008]. The author was the main investigator of this work carried out essentially in collaboration with Dr T.J. Marrow and Dr P.M. Mummery from the MMSC, where he spent over two and a half years as a PDRA. More specifically, he personally carried out all tomography experiments, performed measurements of thermal conductivity of graphite samples and developed the different algorithms to analyse the porosity network. Finally, he proposed and developed the analytical model used to predict the degradation of thermal properties during thermal oxidation of graphite. The work was sponsored by the Health and Safety Executive (NII) (Grant GRA/GNSR/4).

II.1. Context of the study

Polygranular nuclear graphite has been used as a core structural component and moderator for fast neutrons in AGR, Magnox and RBMK (this type of reactor was involved in the Chernobyl accident) reactors. It is also a major component in the latest designs for Generation IV VHTRs. in carbon dioxide cooled, graphite moderated nuclear reactors, such as Magnox and AGR, the dual effects of fast neutron irradiation and radiolytic oxidation which occur during normal operation lead to graphite dimensional and material property changes. For example, thermal properties change due to an increase of internal porosity by radiolytic oxidation [Brocklehurst et al. 1970; Maruyama et al. 1995]. This reduces thermal conductivity as well as Young's modulus and strength. The ability to characterise the irradiation induced evolution of the porosity network and to correlate this with the changes of thermal conductivity is important for understanding the core component thermal behaviour. Although radiolytic oxidation and thermal oxidation are known to have different effects on microstructure evolution [Burchell et al. 1986], in order to avoid the difficulties associated with the examination of irradiated graphite samples, thermal oxidation is often used to simulate the changes that are caused by radiolytic oxidation. This process has been described in Section I.2.1 and is, therefore, not developed herein. The studies on thermally oxidised graphite are also useful to demonstrate the level of information that might be obtained, using the same methodologies, from irradiated samples that have been trepanned from reactor cores.

Therefore, the author's work has focused on the following points:

- Calculation of density and weight loss of graphite samples using X-ray tomography.
- 3D characterisation of the porosity network and its classification into different classes of pores, depending on the type of pore (isolated or continuous) and geometrical parameters (shape, aspect ratio and orientation).
- Modelling of the thermal property of graphite which implements characteristics from the porosity network.
- Comparison between model and experimental measurements of thermal property to validate the theoretical approach.

The use of X-ray tomography to characterise the porosity network, instead of the classical methods, such as mercury porosimetry [Thrower et al. 1982], electromechanical approaches [Calas-Blanchard et al. 2003] and the conventional optical and scanning electron microscopy techniques [Pickup et al. 1986; Breval et al. 2002] was motivated by the following fact. This is the only technique that can handle very fragile and highly porous samples, such as graphite, and analyse density changes and porosity network, both locally and globally.

II.2. Material description and experimental setup

II.2.1. Material

PGA graphite has been chosen for the study. This is an anisotropic grade of nuclear graphite used as a moderator in the UK Magnox reactors. The material is a mixture of graphitised tar-pitch binder with small coke grains of an average size lower than 300 μm (also called "flour"), and “filler” particles – also referred to as inclusions hereafter – which correspond to graphitised large needle coke grains (~0.5-1 mm in size). The needle coke grains tend to be aligned parallel to the length of the graphite block. The PGA samples were provided by Nexia Solutions (Berkeley, UK) with different degrees of thermal oxidation. Every sample had been machined into a cylindrical shape, with a diameter of 12 mm and a height of 6 mm, prior to thermal oxidation. Two groups of samples were defined as WG and AG in accordance with the orientation of inclusions with respect to the revolution axis of the sample:

- WG: major axis of inclusions parallel to the cylinder axis (commonly defined as “With Grain”).
- AG: major axis of inclusions perpendicular to the cylinder axis (defined as “Against Grain”).

II.2.2. X-ray tomography setup

The microstructural observations that the author has carried out were made with the X-Tek HMX-225 laboratory tomographic imager shown in Figure I-3. (Section I.2.2). The instrument has a spatial resolution of 9-10 μm generated at the source of the X-ray fan beam. The experimental setup is schematised in Figure II-1. The samples are positioned at a distance of 100 mm from the X-ray source to generate a pixel size of 13 μm on the CCD screen. a copper target was used for the creation of X-rays as it has a characteristic Kα emission at an energy of 9 keV. in addition, a 0.25 mm thick aluminium filter of was used between the target and the sample to soften the polychromatic beam and to reduce the low energy effect. This limits the beam hardening and the resulting cupping effect artefact [Russ 1995]. The camera is equipped with a beryllium foil detector that is sensitive to the low energies and appropriate for low density materials, such as graphite. The samples were maintained on a rod holder of 12 mm diameter using a folded adhesive tape ring of the same diameter, which allows the samples, even in a very fragile state at high weight loss, to be firmly held during the stage of rotation and translation.

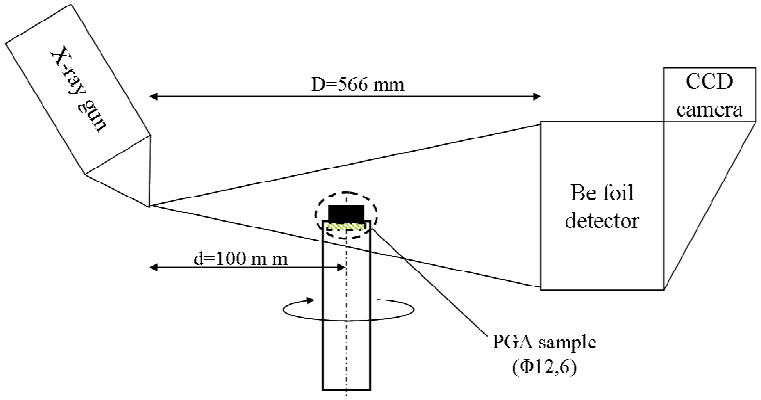

Figure II-1. Schematic representation of the X-ray tomography set-up. Figure published in [Babout et al. 2005]

The determination of local density requires a calibration step. Indeed, the tomography voxels represent a 3D map of the linear attenuation coefficient, μ. For a given material and a given energy in the photoelectric domain (i.e. energy < 200 keV) this factor is proportional to the density of the material, ρ [Attix and Roesch 1968; Baruchel et al. 2000]. The relationship is quite straightforward to define in our case as the material contains only one phase, e.g. carbon. The usual method to determine this relation is to produce and examine a ''step wedge'' on a fully dense graphite sample. The step wedge method consists in measuring the transmitted intensity of the beam through different thickness of the material. The linear attenuation coefficient is then easily determined as it corresponds to the slope of the linear function given in Eq. II-1:

$$\ln(I_0/I) = \mu x \qquad \textbf{Eq. II-1}$$

where I_0 is the incident beam intensity, I the transmitted beam intensity and x the homogeneous thickness of the material. The ratio ρ/μ is then used as a calibration factor to convert from local attenuation to local density at every single voxel of the material.

$$\rho(x,y,z) = \frac{n(x,y,z)}{\alpha}\left(\frac{\rho}{\mu}\right)_{HOPG} \qquad \textbf{Eq. II-2}$$

where $\rho(x, y, z)$ is the local density at a 3D-cartesian coordinate (x, y, z) of the sample volume, $n(x, y, z)$ the corresponding 2^{16} intensity level values. The parameter α is a scale factor for the reconstruction process, which corresponds to the proportional relationship between a local grey level and a local linear attenuation factor calculated from the calibration experiment described by Eq. II-1. An example of a calibration curve is shown in Figure II-2.

For this calibration purpose, a set of HOPG samples was used ,which exhibit a density very close to the crystal density of graphite (2.2 g/cm^3 compared with 2.25 g/cm^3). Later on, the same strategy was adopted by other authors to estimate real density values for other types of a graphite sample [Berre et al. 2008a].

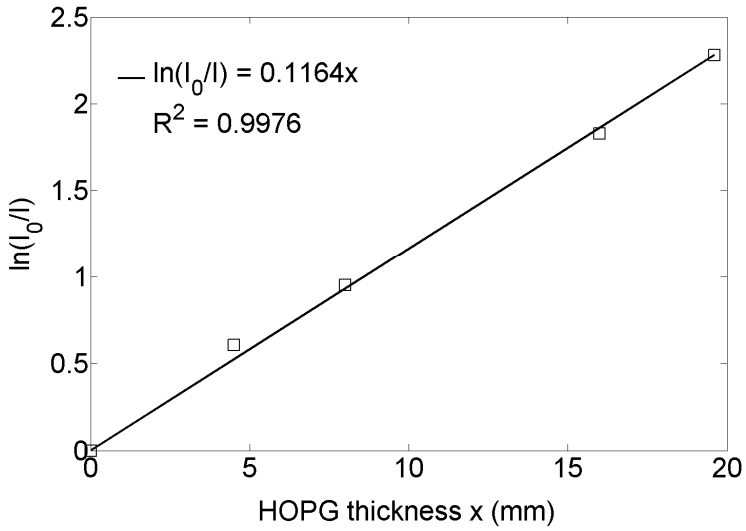

Figure II-2. Calibration measurements: evolution of the attenuation ratio (I_0/I) as a function of HOPG thickness. Figure published in [Babout et al. 2005]

The weight loss undergone by the samples during thermal oxidation can be estimated on the basis of density measurements obtained using X-ray tomography. This method is more precise than simple weight measurements (gross weight loss) since it may happen that the oxidation is not uniform and occurs to a greater extent at the surface than in the bulk of the sample. This results, in the worst case, in an overestimation of the weight loss. The corrected bulk weight loss (CWL) from the density measurement is simply governed by the following equation:

$$\%CWL = 1 - \frac{\rho}{\rho_0} \qquad \textbf{Eq. II-3}$$

where ρ_0 is the density of virgin PGA graphite and ρ the density of thermally oxidised graphite sample. Table II-1 summarises the results of weight loss measurements of the samples studied during this study. The samples are grouped according to the main inclusion orientation.

Table II-1. The tested samples for WG and AG orientations. Bulk weight loss values were obtained by X-ray tomography (1) and in some cases using helium pycnometry (2). Gross weight loss is obtained from initial and final mass, assuming constant volume. Table published in [Babout et al. 2008]

	WG						AG			
Sample name	WG0	WG1	WG2	WG3	WG4	WG5(*)	AG0	AG1	AG2	AG3
Bulk weight loss (%) (1)	–	4.5	12.6	14.1	19.6	23	–	1.2	17.3	19.6
Bulk weight loss (%) (2)	–	4.6	–	–	–	–	–	3.9	20.3	–
Gross weight loss (%)	–	17	15.2	15.1	24.9	29.6	–	20.3	25	21.6

II.3. Experimental results

II.3.1. Qualitative observation of microstructural changes due to thermal oxidation

Figure II-3 presents the reconstructed images of graphite samples at different weight loss. One can see, from Figure II-3a, a relatively good contrast between graphite (dark gray) and porosity (black). However, the matrix and inclusion phases of graphite are hardly distinguishable. It is therefore not possible to segment both phases in virgin graphite. However, as weight loss increases, filler particles (inclusions) become more visible (Figure II-3c). This is because most of the oxidation takes place in the matrix. Contrarily, the porosity network becomes more and more difficult to distinguish as the exposure to thermal oxidation increases. For instance, one can see from the image of the virgin samples different types of pores (calcination cracks in inclusions, entrapment pores in the matrix). The microstructure of WG samples after 4.5% of bulk weight loss is also shown in Figure II-3b. The microstructure does not exhibit strong changes, as compared to the virgin sample. The main difference resides in the roughness of the sample itself that increases significantly between the two oxidation steps. This is the main reason for the explanation of the last discrepancy between gross and bulk weight loss values in Table II-1.

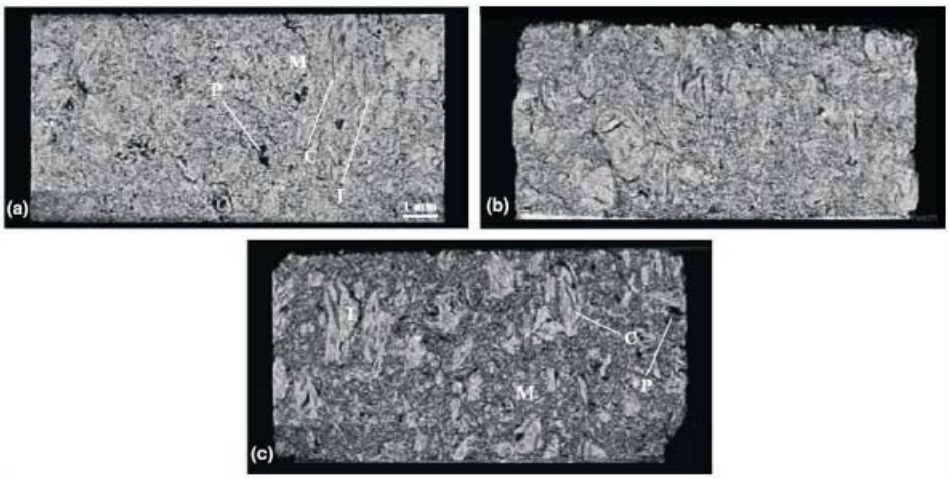

Figure II-3. Longitudinal reconstructed slices of ''WG'' samples at different sample weight losses. (a) WG0 (virgin), (b) WG1 (4.5% CWL), and (c) WG5 (23% CWL). The labels denote: ''I'', inclusions (i.e. large filler particles), ''C'', calcination cracks, ''M'', matrix (i.e. tar-pitch and flour particles) and ''P'', porosity from entrapped gas. Figures published in [Babout et al. 2005]

One can also see the evolution of the microstructure and the changes of density from the density histograms, as shown in Figure II-4. The average density clearly decreases with an increase in weight loss. The spread of the density also increases with weight loss, and a second peak becomes apparent above a weight loss of ~20% (samples WG4 and WG5). This has the effect of increasing the contrast between the matrix and the inclusions.

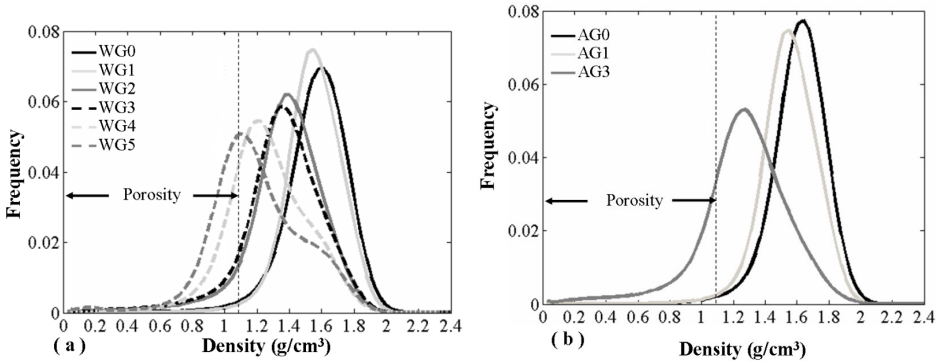

Figure II-4. Density histograms of (a) WG and (b) AG samples. Figure (a) published in [Babout et al. 2008]

II.3.2. Quantitative analysis

If one consider the histograms shown in Figure II-4, the segmentation of the porosity network and the inclusions is not straightforward as there is no clear distinction between the density profiles that represent these phases. However, the segmentation of these phases is of great importance from the modelling point of view. The following sections present the strategies developed by the author that were adopted to achieve these goals.

II.3.2.1. Inclusion segmentation

From the modelling point of view, the knowledge of inclusion content and morphology can be a key issue when calculating effective properties. For instance, it is known [Nightingale 1962] that the anisotropy of mechanical, thermal and electrical properties is reduced as the filler particle size is increased. The determination of the volume fraction of large filler particles (inclusions) in the sample, assuming it is constant across the samples, was performed using the WG5 sample. This sample presents the largest weight loss and displays the best contrast between the matrix and the inclusions (see Figure II-3).

The method that has been chosen involves selecting a large number of two-dimensional regions, slice by slice, independently in both phases, namely the inclusions and the matrix phases (i.e. mixture of pitch, porosities and flour particles in the range size of the tomographic spatial resolution (i.e. 13 μm)). The author encourages readers to refer to [Babout et al. 2005] for more information about the software used and the selection method. Note that the different areas in the large coke filler particles free of cracks or porosities were selected so that only the highest densities would be taken into account. With both phases displayed and the corresponding histograms normalised, an expression which corresponds to the following simple mixture law is used to fit the histogram of the WG5 sample

$$h = (1 - f)h_{matrix} + fh_{inclusion} \qquad \textbf{Eq. II-4}$$

where h_{matrix} and $h_{inclusion}$ are the histograms of the two phases, and f the volume fraction of dense large filler particles. The best fit corresponds to a volume fraction of inclusions of about 23%. The value found with this method is close to what can be found in the literature [Nightingale 1962], yet one should keep in mind that the real content is proprietary information.

The segmentation of the filler particles can also be very useful for numerical modelling of various local graphite properties (e.g. mechanical, thermal, electrical) under the influence of oxidation (thermal or radiolytic).

The previous results have shown that the filler particles become distinguishable when weight loss due to thermal oxidation increases, since the oxidation mainly affects the matrix. The segmentation of the filler particles is then made possible, but still the direct threshold segmentation, as shown by the example in Figure II-5, leads to non-satisfying result in terms of noise (too many filler particles present in the matrix segmented) and feature labelling (too few features labelled because a large interconnection occurs between segmented voxels that are supposed to correspond to inclusions). Therefore, the following pre-processing method has been applied to extract large filler particles. This method is also described in [Babout et al. 2006b].

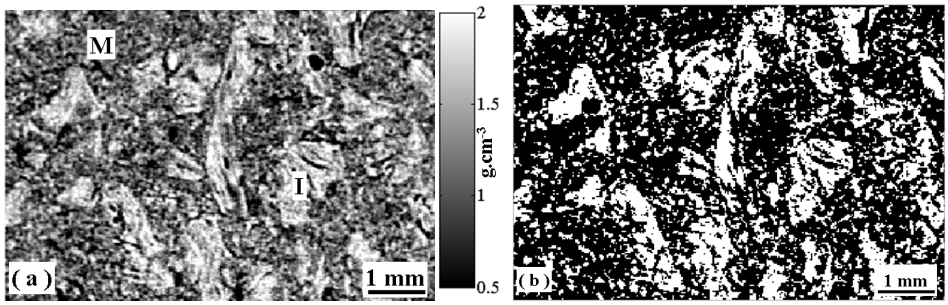

Figure II-5. Example of simple threshold segmentation of WG5 sample. (a) raw image with corresponding density scale. (b) segmented image with density threshold set to 1.4 g/cm^3. Figures published in [Babout et al. 2006b]

The method consists in applying a smoothing filter to each voxel that composes the 3D image. The grey level value of the voxel is replaced by the average value of the surrounding kernel. The boundary problem associated with the voxels that lie nearer to the edge of the volume than the half-width of the box is solved by assuming that the volume edges are mirrors, so that each plane containing these voxels is duplicated beyond it. This ‘‘kernel’’ operation of neighbourhood averaging, commonly used in image treatment for noise reduction [Russ 1995], allows the data to be smoothed and reveals more clearly the average density fluctuation throughout the specimen. As thermal oxidation rate increases, the contrast between the matrix and the inclusions is enhanced. This is shown in Figure II-6a-c for different kernel sizes (i.e. 7, 11 and 15 voxels). Naturally,

the larger the averaging volume (box), the more homogeneous the density map. Moreover, the smoothing action reduces significantly the interconnectivity (or interlinkage) between the inclusions. Since the kernel operation is isotropic, although the labelled inclusions suffer from an inevitable reduction of size, which leads to a decrease in their volume fraction, they mainly retain their morphological properties. An example is shown in Figure II-6d delineating the contours of the labelled inclusions superimposed on the original microstructure. As a consequence, the size of the box must be chosen with respect to the characteristics of the architecture to be quantified. Therefore, a criterion has been established to choose the optimal box size for the task of inclusion labelling, which minimises interlinkage and the error in calculating the inclusion volume fraction. Firstly, the interlinkage parameter *IP* can be defined, as in Martin et al. [Martin et al. 2000], as the ratio between the volume of the largest labelled inclusion and the corresponding total volume of inclusions. Secondly, the second parameter *f**, representing a normalised volume fraction difference, can be defined as follows:

$$f^* = \left| f - f_{th} \right| / f_{th} \qquad \textbf{Eq. II-5}$$

where f is the volume fraction of the inclusions segmented for different values of box size, and f_{th} the volume fraction of the inclusions calculated above, i.e., 23%.

Both dimensionless parameters are calculated for different averaging box sizes. Their evolutions as well as the product and the average of *IP* and *f** are shown in Figure II-7. One can see that, in contrast to the product criterion, the average criterion presents a single minimum value, which corresponds to an optimal box size of 180-190 μm. a 3D representation of the inclusions after the volume treatment with the box size of 182 μm is shown in Fig. 6a. The resulting segmented 3D volume is suitable for converting into a 3D mesh for the subsequent FEA, for example, in order to examine the influence of oxidation (thermal or radiolytic) on various local graphite properties (e.g., mechanical, thermal, electrical).

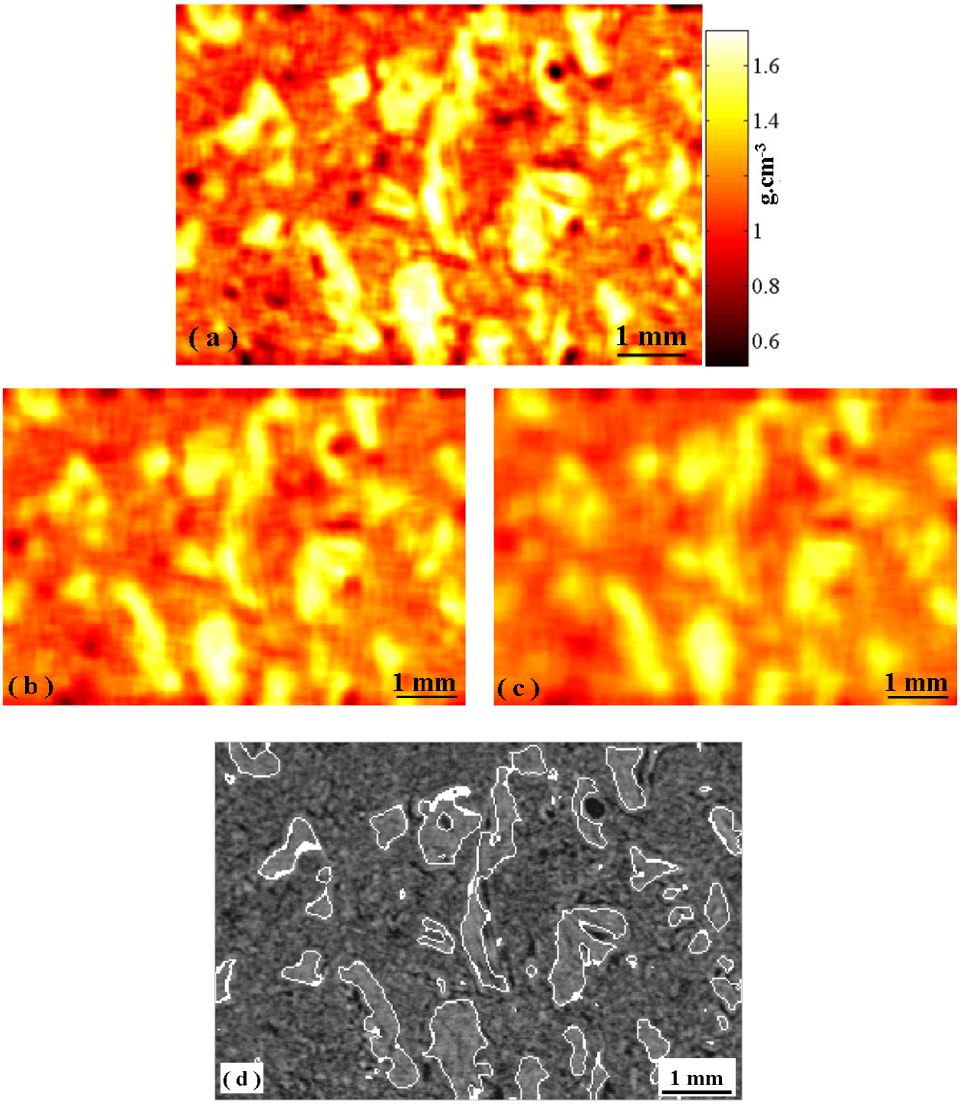

Figure II-6. Density maps corresponding to Figure II-5a with different box sizes. (a) a = 182 µm, (b) a = 286 µm, (c) a = 390 µm. (d) Inclusion contours superimposed on the microstructure of Figure II-5a after operating the averaging kernel (a = 182 µm) followed by threshold segmentation. Voxel size = 26 µm. Figures published in [Babout et al. 2006b]

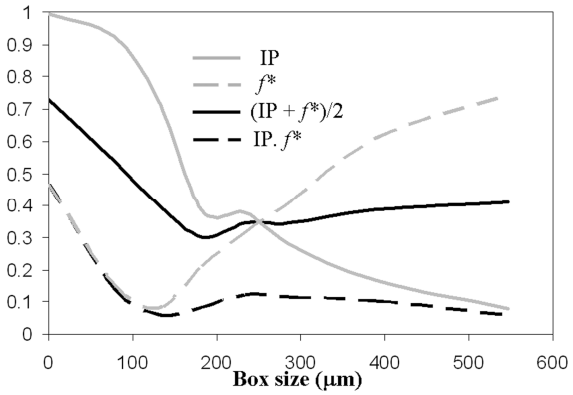

Figure II-7. Evolutions of average and product criteria for different averaging box sizes applied to sample WG5. *IP*: inclusion interlinkage parameter. *f: normalised inclusion volume fraction difference. Labelling process after threshold density set to 1.4 g/cm^3. Figure published in [Babout et al. 2006b]**

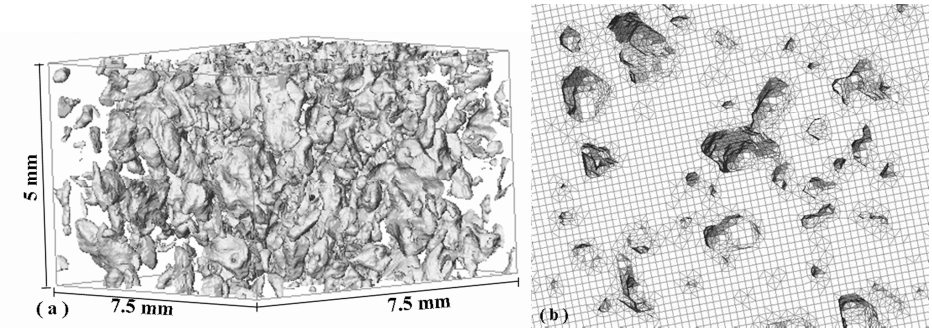

Figure II-8. (a) 3D representation of the inclusions after binary thresholding of WG5 with box size a = 182 µm. The extrusion direction is vertical. (b) View of one of the 3D mesh faces of the volume corresponding to WG5 after the averaging kernel. Mesh with hexahedral and tetrahedral elements (tetrahedral elements at the boundary between the matrix and the inclusions). Figures published in [Babout et al. 2006b]

The method presented above is an illustration of the exercise and the quality of the computing conversion. The model, that has been developed and which is summarized in Section II.4, endorses an analytical approach that considers directly the microstructure and morphological parameters that are obtained from volumetric image analysis. However, it is worth mentioning that other authors employed a similar approach using three-dimensional multi-phase finite element models, based on X-ray tomography images of thermally oxidised graphite, to calculate changes in mechanical properties such as Young's modulus, compressive and tensile strengths [Berre et al. 2008a; Berre et al. 2008b]. Their results proved to be in good agreement with the experimental data.

II.3.2.2. Porosity classification

II.3.2.2.1. Segmentation of porosity

The selection of appropriate segmentation methods is important. Segmentation of the observed porosity from the microstructure could be achieved by selecting a nominal threshold value and assessing visually whether the segmented features are representative of the material. However, this standard method is manual and may lead to subjective threshold selection, especially when one can see from the density histogram that there is no clear distinction between the density peaks of each phase (porosity and graphite). To overcome this problem, the threshold density value is determined in the following manner.

The density distributions (Figure II-4) show that most of the voxels contain some un-resolved porosity, which reduces the element density. a criterion was selected to quantify this by defining the fraction of porosity f_i in a voxel i to be directly correlated to the voxel density ρ_i and the graphite single crystal density ρ_{cryst}, using Eq. II-6.

$$f_i = 1 - \rho_i / \rho_{cryst} \qquad \textbf{Eq. II-6}$$

If this fraction of porosity was to be reduced to an equivalent single spherical pore of diameter d_i, the fraction of porosity in the voxel f_i could then be expressed using Eq. II-7, where a is the size of a voxel

$$f_i = \frac{\pi}{6}\left(\frac{d_i}{a}\right)^3 \qquad \textbf{Eq. II-7}$$

The criterion that the author proposed for determining the fraction of porosity from tomography data is that a voxel will be assigned as a pore if the virtual sphere representing its porosity extends beyond the voxel bounds. Eq. II-7 demonstrates that this corresponds to the case where f_i is larger than $\pi/6$ (i.e. ~52%). The equivalent criteria arise in geometric percolation models, such as Runge's approach [Euler 1957]. in the studied case, the threshold value to segment the porosity is found to be equal to $(1-\pi/6)\rho_{cryst}$, which is close to 1.07 g/cm^3 (ρ_{cryst} = 2.25 g/cm^3).

The volume fraction of the segmented porosity f for the two groups of samples was thus calculated for this common threshold value of 1.07 g/cm^3. This volume fraction is the ratio between the number of voxels segmented by this threshold and the total number of voxels in the volume studied. The shrinkage of the sample due to surface loss during oxidation does not affect the calculated value. The evolution of this ratio with the bulk weight loss x obtained using X-ray tomography is shown in Figure II-9 for the WG and AG samples. This figure

also shows the theoretical evolution. The data was found to fit an exponential relationship. The volume fraction of total porosity observed at the virgin state (0% weight loss) was found to be 1.8%. This value remains in substantial discrepancy with the normal value of 22%, calculated on the basis of density measurements. As the weight loss increases, the discrepancy decreases. The highest fraction of porosity observed was approximately 40%. These values correspond to porosity which is large enough to be resolved by the X-ray tomograph (spatial resolution of 9-10 µm generated at the source of the X-ray fan beam). All un-resolved pores, e.g. pores with a size which is far more lower than the voxel size, cannot be segmented and therefore are not taken into account in the calculation of the pore volume fraction after segmentation. One can see that when samples have a lower size and therefore the voxel size is lower ("6-12 µm" samples in Figure II-9), the volume fraction of segmented pores increases, but is still considerably smaller than the theoretical value (volume fraction of ~5 and 10% for scans with voxel size of 12 and 6 µm, respectively). This discrepancy is more pronounced for a low weight loss sample than a higher one. This change is attributed to the fact that coalescence occurs between pores as the weight loss increases (see Section II.3.2.2.2) and unresolved pores coalesce together to form interconnected pores with a size larger than the voxel size. This is of course our suggestion and complementary experiments carried out on the same sample at different weight loss will provide additional information on how the porosity network changes.

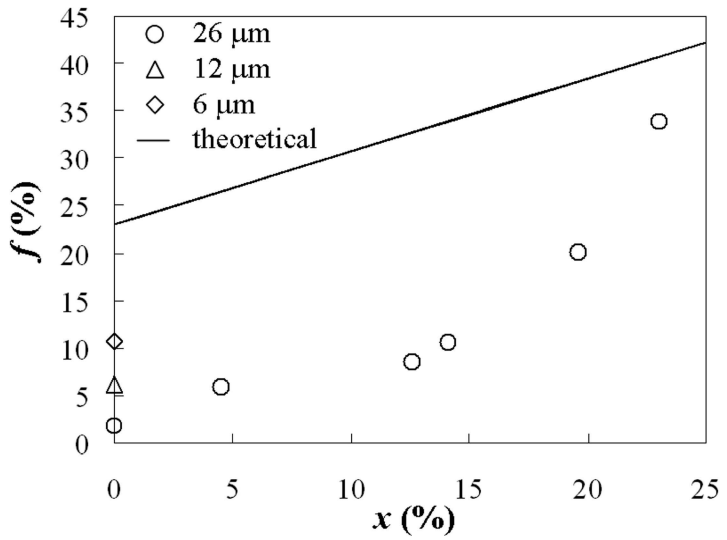

Figure II-9. Comparison of the volume fraction of labelled pores *f* for the different weight losses *x* of WG samples with the theoretical evolution. Volume fractions calculated for other sizes of virgin WG samples that match lower voxel sizes (6 and 12 µm) are also plotted. Figure published in [Babout et al. 2008]

II.3.2.2.2. Isolated vs. Continuous: the IB method

The porosity network in graphite is very complicated since it is composed of different types of pores [Nightingale 1962]: (a) calcination cracks, attributed to volume shrinkage during calcination, (b) large gas entrapment pores in the matrix, usually formed during the baking and (c) narrow, slit-like pores which develop on cooling from the graphitisation temperature (~3000°C). These pores vary in size, shape and orientation and can be also isolated, or interconnected. in the latter case, the connected pores result in very tortuous shapes. The classification of these pores and the evaluation of their respective proportion in the graphite material are important to be characterised in order to simulate the thermal properties of the material.

The methodology that the author has proposed and programmed to classify the pores in the two groups of isolated and continuous phases is based on detecting the different branches which "shape" their respective morphology. This detection consists in calculating the number of intersections between a growing three-dimensional cubic box and the considered phase, or, in other words, the number of times the box crosses over the corresponding phase. The parameter calculated is very sensitive to the irregularity and tortuosity of the pores, and thus can be used to discriminate them by their shape. An illustration is shown in Figure II-10 for the case of a fictitious object representing a porosity.

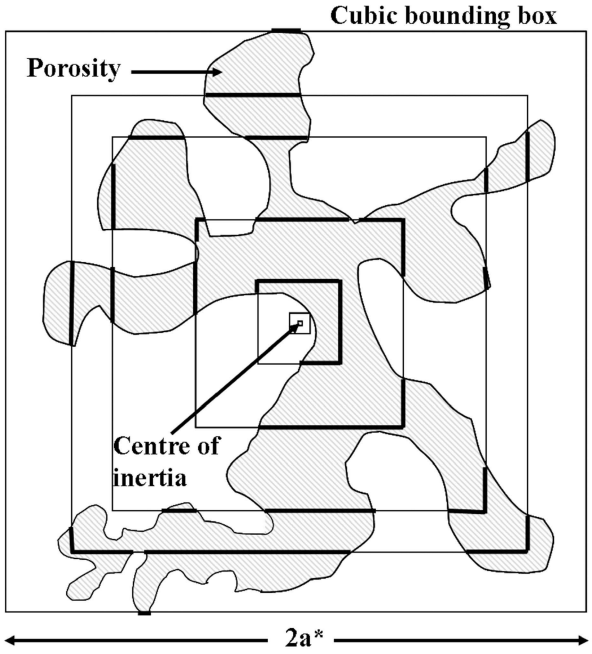

Figure II-10. 2D Illustration of the IB method to classify pores as isolated or continuous (interconnected) phases

The methodology is based on the following procedure, also described elsewhere [Babout 2006]:

1. *Apply a threshold to the volume of interest V to segment the porosity*
2. *Label the phases with 26-connectivity neighbours*
3. *Extract parameters from N labels (Voxel List, Volume, Centroid, Bounding box)*
4. *For each label i*
   a. *Initialise the number of intersection n_i to zero*
   b. *Calculate the surrounding cubic box (max. dimension of the bounding box)*
   c. *For each increment j which corresponds to a growing box, from the centroid position of the label to the surrounding cubic box*
      i. *Select the temporary volume $V_{i,j}$ which corresponds to the intersection between the growing box and the label i*
      ii. *Repeat steps 1-3*
      iii. *If the number of temporary label $n_{i,j}$ is null or no voxel in $V_{i,j}$ is equal to zero, skip the rest of the loop and return to step c*
      iv. *Add the number of new temporary label $n_{i,j}$ to n_i*
      v. *Divide n_i by the number of increment which does nor satisfy step iii to calculate the temporary average number of intersection $\langle n_i \rangle$*
   d. *if $\langle n_i \rangle \leq 6$, the phase corresponding to label i is classified as isolated. Otherwise, the phase is classified as continuous.*

The step *c.iii* is included in the procedure to guarantee a good estimation of the average number of intersections. Indeed, any increment corresponding to a box which does not intercept the phase is not taken into account in the average calculation. Otherwise, the number of paths is greater, so the average number of intersections is decreased. This case happens when the centre of mass is located outside the corresponding phase. Moreover, any increment corresponding to a box which is contained within the phase is also rejected from the calculation, because it contradicts the definition of the intersection method. The omission of the previous condition has also a direct effect on the average number of intersections. in the simple case of a sphere, $\langle n \rangle$ is equal to 3.1 without the rule, while $\langle n \rangle$ is equal to the maximum number of intersections, i.e. $n = 6$, when it is taken into account.

In step *d* of the algorithm, the average number of intersections $\langle n_i \rangle$ is compared with a reference value. Instead of being defined arbitrarily, the reference value corresponds to the maximum intersection of a growing box around a sphere, i.e. $n = 6$. The sphere has been chosen to characterise, among all the standard geometrical shapes, the transition between isolated and continuous pores, because it presents the highest average and maximum numbers of intersections with a cubic box.

The method has been programmed in Matlab. The computational time mainly varies with the size of the reconstructed volume and the volume fraction of segmented porosity. a volume with a size of 300x300x200 voxels and ~30 vol.% of segmented porosity is generally treated in 5 min. with a 1.66 GHz processor.

The case of two different types of segmented pores are presented in Figure II-11, with the corresponding profiles of intersected branches shown in Figure II-12. What is visually guessed is confirmed by the calculation: Pore 1 is classified as continuous since its average number of intersections is around 15, while Pore 2 is classified with our method as isolated as its average number of intersected branches is lower than 5.

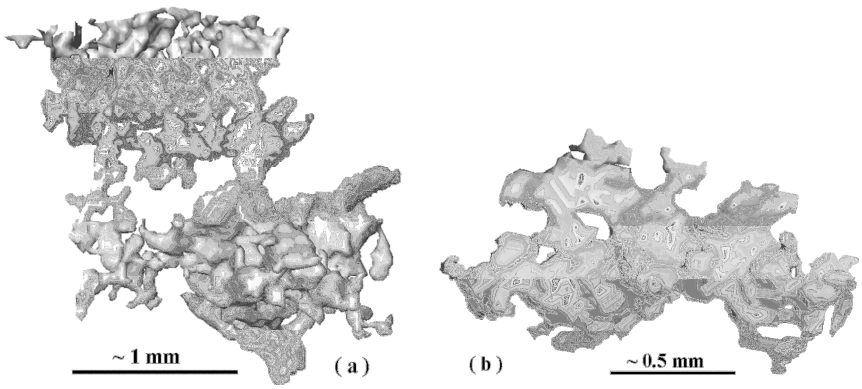

Figure II-11. Examples of different geometries of pores observed in thermally oxidised PGA graphite (sample WG2). (a) refer to Pore 1 in the text. (b) refers to Pore 2 in the text. Figures published in [Babout et al. 2008]

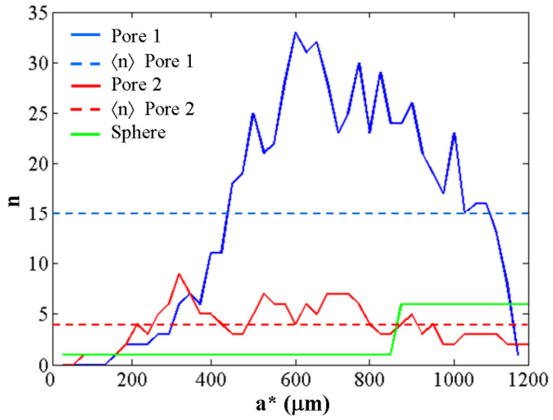

Figure II-12. The average number, <*n*>, of intersections with the bounding box and a pore, and the total number of intersections with different pores as a function of the box dimensions (half-length). Pores 1 and 2 are of same size and are illustrated in. Number of intersections for a sphere of same size as the pores is also shown. Figure published in [Babout et al. 2008]

The IB method has mainly been designed to study the effect of thermal oxidation on the observed pore structures of WG and AG. The evolutions of the total volume fraction of continuous pores, f_{cont}, and isolated pores, f_{iso} are shown as a function of the corresponding volume fraction of the observed porosity, f, in Figure II-13. The volume fraction of the observed continuous pores rises with increasing porosity and saturates close to 100% as f increases. The total percentage of the isolated porosity remains relatively stable up to 10-15% of the total percentage of the connected porosity, then decreases with the increasing weight loss. More than 99% of the observed pores are continuous when f is close to 35%.

The effect of weight loss on the calculated pore size distribution, for the two classes of the observed pores, is shown in Figure II-14. Representative data for WG0, WG2 and WG4, with weight losses of 0, 12.6 and 19.6% are shown, in terms of the pore equivalent diameter, d^* (i.e. The diameter of a sphere with the same volume as the pore). One can see that the isolated pore size distributions are very similar in all the samples, varying between 10 and 100 μm. On the other hand, the continuous pore size distributions show significant increase in equivalent diameter with weight loss.

Another interesting evolution to look at is the fractions of open and closed pores. Open pores are those that connect to the exterior of the sample. Both open and closed pore groups may include both connected and isolated pores. The population of the open porosity has been estimated for the isolated and continuous groups as follows. The segmentation and labelling of the original volume defines the open porosity (i.e. voxels with density less than 1.07 g/cm^3) that is connected to the surface of the sample. a direct comparison of this feature with the identified isolated and continuous pores allows classification of each pore as open or closed. Figure II-13 shows the evolution of the open porosity f_{open} and the closed porosity f_{closed} for all the sets of samples as a function of the overall porosity content f. The data from the AG and WG samples is combined, as it shows no significant differences. One can notice that the evolution of open and closed pores is largely similar to the evolution of continuous and isolated pores, respectively. The relative fraction of the isolated pores that are classified also as open pores remains constant (~10-15%), while the relative fraction of the open pores that are continuous steeply increases and approaches 100% for f larger than 10% (i.e. all the continuous porosity appears open). Therefore, it can be suggested from inspection of Figure II-13 and Figure II-14 that the observed increase in the size and volume fraction of continuous pores in the PGA samples is connected with the development of open porosity within the material. Accordingly, the decrease in the volume fraction of isolated pores is believed to be governed by coalescence phenomenon between closed isolated pores and continuous pores, the coalescence being pore size independent.

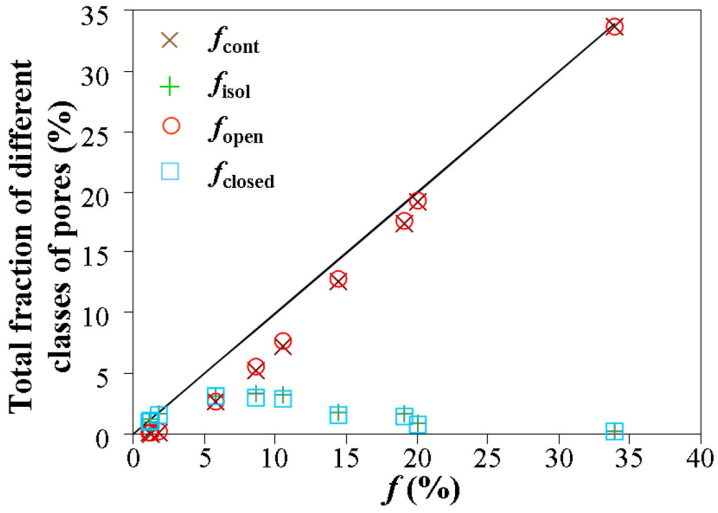

Figure II-13. Variations of total volume fractions of continuous/isolated pores and open/closed pores. The linear line corresponds to the function $f = f$ where f is the total volume fraction of porosity. The samples WG and AG are not considered separately in this particular case. Figure published in [Babout et al. 2008]

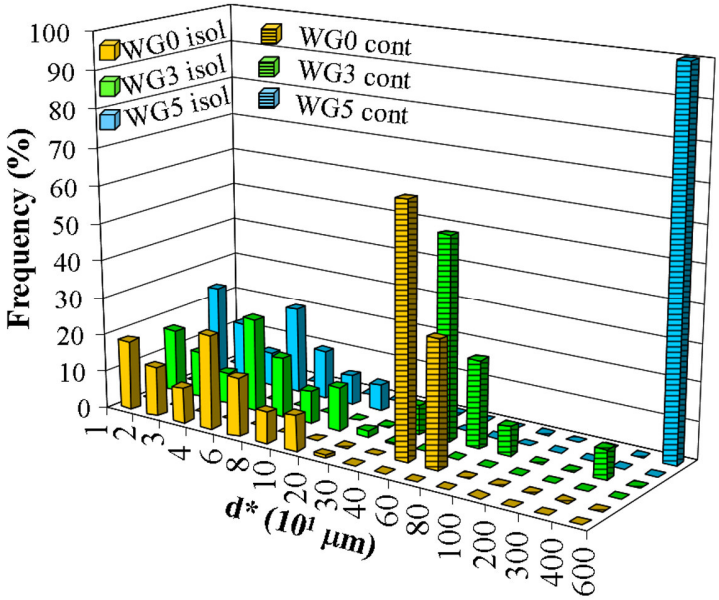

Figure II-14. The equivalent pore size distribution for isolated and continuous pores, for three different WG samples: WL = 0%, WL = 14.1% and WL = 23% (WG0, WG3 and WG5). The isolated pore size distribution does not vary significantly with weight loss, whereas the continuous porosity distribution shows increasing pore size. Figure published in [Babout et al. 2008]

II.3.2.2.3. Morphology of isolated pores

The identification of individual pores by the analysis of X-ray tomography data allows one to make classification of pore shape. The morphology of pores, in terms of their aspect ratio and orientation, has been previously related to mechanical and physical properties of materials [Buffière et al. 2001; Hyun et al. 2001; Cernuschi et al. 2004]. The shapes of continuous pores are highly complex, and no attempt has been made to describe them. Therefore, attention has been focused on isolated pores.

Large numbers of isolated pores are observed in the studied volumes (typically up to 17000 identifiable pores). in the un-oxidised graphite, the isolated pores represent almost 100% of the total porosity, and their morphology can therefore be expected to be potentially relevant to material properties at low to moderate weight loss. a sub-classification of the isolated pores has been applied and adapted for implementing in analytical or numerical models [Rice 1996; Boccaccini 1998; Roberts and Garboczi 2000; Cernuschi et al. 2004]. Suitable sets of parameters need to be selected to define correct bounds for classification. This has been done by inspection of the data.

Figure II-15 presents data for all isolated pores, in the form of scattergrams for different combinations of morphological parameters. The aspect ratios for each pore (F_{ab}, F_{bc} and F_{ac}) are obtained from the three principal dimensions a, b and c (with $a > b > c$) of an *equivalent ellipsoid*[7]. ($F_{ab} = a/b$ etc). The principal orientation θ of a given pore is obtained from the moment of inertia tensor of the pore. It is defined as the angle between the vertical axis of the sample (or the revolution axis of the cylindrical sample) and the Eigen vector $\boldsymbol{V_{aa}}$ of the smallest Eigen value, I_{aa}, of the moment of inertia, after Eigen decomposition. The scattergrams (Figure II-15a to Figure II-15c) with the pore equivalent diameter (d^*) with F_{ac}, F_{ac} with pore orientation θ and aspect ratio F_{ab} with F_{ac} appear compact and homogeneous. They do not reveal any correlation between the covariates which may be used to define different classes of isolated pores. There is, however, some correlation between
F_{ab} and F_{bc} (Figure II-15d), which has been chosen to establish a shape classification of the isolated pores based on the ellipsoid morphology. The classification has been applied using boundaries to divide the pores into three different sub-groups, based on the following criteria:

[7] The *equivalent ellipsoid* of a body is the homogeneous solid ellipsoid, centred at the body's centre of gravity, with the same Eigen value and Eigen vectors as the body.

- Prolate (a >> b and b ~ c.): F_{ab} “large” ($F_{ab} > \alpha$) and F_{bc} “small” ($F_{bc} < \beta$).
- Oblate (a ~b and b >> c): F_{ab} “small” ($F_{ab} < \alpha$) and F_{bc} “large” ($F_{bc} > \beta$).
- Spheroid (a ~ b ~ c): F_{ab} and F_{bc} both “small”. ($F_{ab} < \alpha$) and ($F_{bc} < \beta$).

The values of α and β were selected by inspection of the distribution of aspect ratios shown in Figure II-15d and are both arbitrarily set to 2.5. Comparable values have been previously used to classify aggregate particles into different classes of shapes [Uthus et al. 2005]. The few remaining points (less than 0.5% of the isolated pores) which do not satisfy the above criteria (fourth rectangle in Figure II-15d) are classified as prolate or oblate, using the following criteria:

- $\forall(F_{ab} > \alpha, F_{bc} > \beta), (F_{ab}-\alpha) < (F_{bc}-\beta) \Rightarrow$ oblate.
- $\forall(F_{ab} > \alpha, F_{bc} > \beta), (F_{ab}-\alpha) > (F_{bc}-\beta) \Rightarrow$ prolate.

This is graphically equivalent to associating these points with the closest region in Figure II-15d. The relative fractions of continuous and isolated pores and the different fractions of isolated pore types are summarised in Table II-2 as a function of thermal oxidation weight loss. The spheroid sub-group is the largest component of the isolated pores. The relative fractions of the isolated pore subgroups do not vary significantly with weight loss. The AG samples show a variation of the spheroid and oblate sub-groups, but this is not repeated in the WG samples of the same virgin microstructure. This suggests that thermal oxidation process does not have a measurably different effect on the different isolated pore classes, as would be expected. The same conclusion can also be proposed for the evolution of the maximal aspect ratio, which also does not vary significantly with weight loss. The corresponding standard deviations are relatively large since the classification of isolated pores was organised only into three simple shapes. However, one can see that the scatter in the aspect ratio also remains relatively constant. These observations, however, concern different samples and different weight loss. a more accurate assessment of the effects of oxidation on isolated pore morphologies may be achieved with the same sample scanned by X-ray tomography observed with progressive oxidation. in the present analysis, the measured pore classifications has been used to evaluate their effect on thermal properties of graphite.

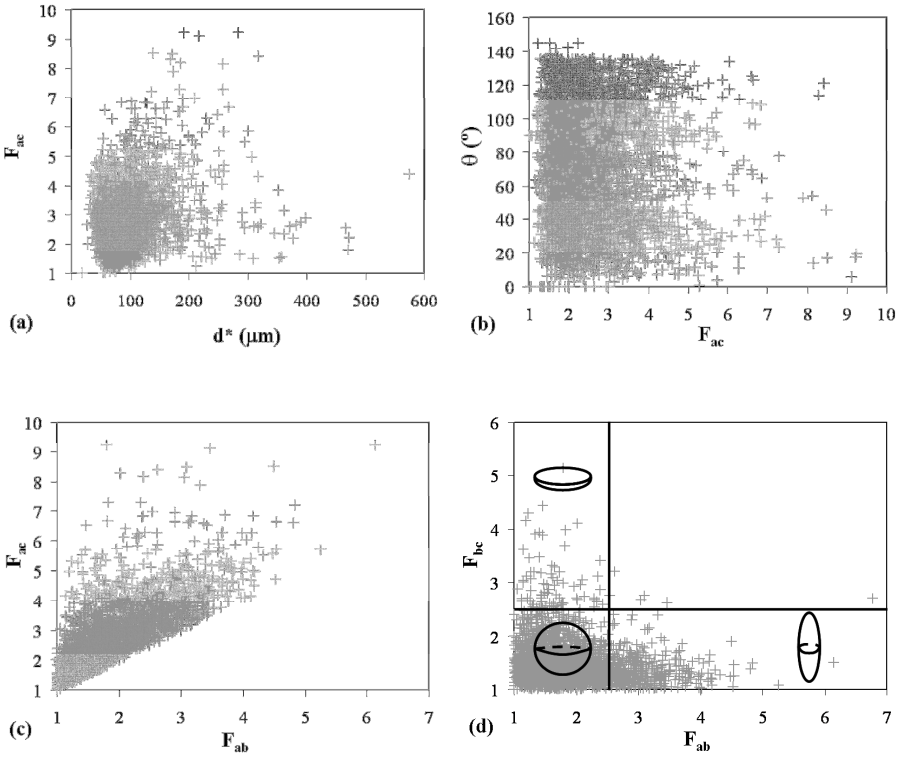

Figure II-15. Morphology scattergrams for isolated pores from sample WG0. (a) aspect ratio F_{ac} vs. equivalent diameter, (b) orientation / vertical axis of sample vs. aspect ratio F_{ac}, (c) aspect ratio F_{ab} vs. aspect ratio F_{ac}, (d) aspect ratio F_{ab} vs. aspect ratio F_{bc}. The figure also shows the selected sub-classification of isolated pores in three ellipsoid shapes: oblate (upper left zone), spheroid (lower left zone) and prolate (lower right zone)

Table II-2. Mean maximal aspect ratio $\langle F_{ac} \rangle$ with corresponding standard deviation (in italic) and fractions of the different ellipsoid shapes of isolated porosity (f_{isol1}, f_{isol2}, f_{isol3}) for different studied samples. The relative fractions of isolated (f_{isol}) and continuous (f_{cont}) porosity determined from the intersection method are also given. The fractions of the different ellipsoid shapes are relative to the total fraction of isolated porosity. The mean aspect ratio for oblate sub-group is expressed inversely so all ratios are defined in accordance with the revolution axis (revolution axis for spheroid and prolate: along "a" axis – revolution axis for oblate: along "c" axis)

Samples		Porosity Ratio		Spheroid		Prolate		Oblate	
	WL (%)	f_{isol} (%)	f_{cont} (%)	$\langle F_{ac} \rangle$	(f_{isol1}) (%)	$\langle F_{ac} \rangle$	(f_{isol2}) (%)	$\langle F_{ca} \rangle$	(f_{isol3}) (%)
WG	0	93.8	6.2	2.27 / *0.62*	73.6	4.35 / *1.19*	16.2	0.15 / *0.13*	10.2
	4.5	53.9	46.1	2.29 / *0.63*	71.6	4.37 / *1.21*	18.0	0.16 / *0.13*	10.4
	12.6	38.8	61.2	2.25 / *0.60*	78.4	4.27 / *1.20*	14.2	0.15 / *0.13*	7.2
	14.1	31.3	68.7	2.27 / *0.62*	81.5	4.30 / *1.29*	12.5	0.15 / *0.14*	6.1
	19.6	4.3	95.7	2.29 / *0.62*	79.1	4.20 / *1.12*	14.0	0.16 / *0.14*	7.0
	23	0.7	99.3	2.29 / *0.66*	71.4	4.83 / *1.81*	14.3	0.17 / *0.12*	14.3
AG	0	94.5	5.5	2.42 / *0.69*	66.5	4.61 / *1.22*	11.0	0.16 / *0.12*	22.5
	1.2	100	0	2.27 / *0.63*	71.7	4.34 / *1.24*	11.8	0.16 / *0.13*	16.6
	17.3	12.6	87.4	2.38 / *0.65*	75.4	4.25 / *1.17*	18.3	0.15 / *0.14*	6.3
	19.6	8.6	91.4	2.36 / *0.61*	80.2	4.17 / *1.11*	14.0	0.16 / *0.14*	5.8

II.4. Modelling of thermal property: case of thermal conductivity

II.4.1. Considerations

In graphite, at the temperature of practical interest to nuclear engineers (i.e. lower than 1000ºC), the mechanism by which heat is transferred is mainly through phonon oscillations along basal planes of the crystalline lattice. It is therefore sensitive to crystallographic anisotropy and atomic bonding, and is reduced by defects and impurities, grain boundary or porosity. The latter one reduces the phonon mean-free path by phonon scattering which increases with increased temperature [Kinoshita and Munekawa 1997; Raghavan et al. 1998; Burchell 2001; Prasher 2006]. Among these types of scattering, it has been shown that thermal conductivity decrease is dominated by pore-phonon scattering, the effect being more important than grain boundary-phonon scattering down to grain size of 50 nm [Raghavan et al. 1998].

The chemical analysis of PGA shows that the amount of impurities is very small [White et al. 1984], typically measured in ppm. The scattering of phonon with impurities is more unlikely to be an important mechanism in PGA. The effect of grain boundary (or inclusion/matrix interface) on thermal conductivity is difficult to quantify in the complicated microstructure of polygranular nuclear graphite. Indeed, different grain boundary-phonon scattering could occur, including between flour and binder in the matrix, or between flour and needle coke grains. However, past studies have shown that the decrease of thermal conductivity due to phonon scattering at grain boundary starts to be significant for grain size lower than 100 µm [KINOSHITA and MUNEKAWA – 1997]. Drawing on this result and considering the size of the grains for the matrix and the inclusion in PGA (see Section II.2.1), it has been assumed that the only scattering effect which markedly decreases thermal conductivity in PGA is the one between pores and phonon.

II.4.2. Model Description and results

The model that the author has developed [Babout et al. 2008] focuses on the effect of porosity on thermal conductivity. The influence of the different classes of porosity at different scales has previously been examined [Brocklehurst et al. 1970; Randrianalisoa and Baillis 2007], and it was concluded that thermal conductivity is sensitive to the structure, size and orientation of isolated and interconnected porosity.

From the pioneering studies carried out on electric conductivity by Maxwell in the 19th century (summarised by Euler [Euler 1957]), a large number of analytical models have been proposed in the literature to calculate effective thermal conductivity: purely empirical approaches [Knudsen 1959], phase

morphology-dependency models based on parameters, such as pore shape (aspect ratio) and pore orientation [Meredith and Tobias 1962; Schulz 1981] and geometrical models based on the porosity arrangement, the pores being defined as isolated or continuous (or interconnected) [Euler 1957; Rice 2005]. The simple model developed by Euler [Euler 1957] is of particular interest when modelling porous materials with both isolated and continuous pores. Brocklehurst et al. used this approach to model thermal conductivity of radiolytically oxidised graphite samples [Brocklehurst et al. 1970]. The models fitted the experimental data well for pore volume fractions up to 48%. However, the relative content of continuous and isolated pores was assumed, rather than experimentally determined.

The approach proposed by Euler has been chosen to model thermal conductivity in thermally oxidised graphite, with the main difference being the experimental quantification of the porosity network using X-ray tomography. The model has been thoroughly described in [Babout et al. 2008] and the main characteristics are recalled hereafter.

The Euler's approach, based on Runge's geometrical model (also presented in [Euler 1957]), considers two bounds which correspond to two extreme cases: periodical arrays of spherical pores or solid spheres to model isolated or continuous porosity. For a fractional porosity ε, the corresponding expressions of bounds noted Y_1 and Y_2 are:

$$Y_1 : k/k_s = (1-\varepsilon)/(1+0.5\varepsilon) \qquad \textbf{Eq. II-8}$$

with $\varepsilon \leq \pi/6$ according to the limitation of Runge's geometrical model and

$$Y_2 : k/k_s = \pi(r^2 - 0.25) \qquad \textbf{Eq. II-9}$$

where r is the solution of the expression

$$1-\varepsilon = \pi\left(-\frac{8}{3}r^3 + 3r^2 - \frac{1}{4}\right) \qquad \textbf{Eq. II-10}$$

In the former equations, k_s is the thermal conductivity of the solid body (258 and 181 W/m/K for k_s corresponding to the WG and AG samples, respectively). Y_1 corresponds to the Maxwell-Eucken upper bound for porous materials (i.e. in a two phase material, when the ratio between k_r and k_m, the thermal conductivities of the reinforcement (or pore) and matrix, respectively, is small compared to the whole). The lower bound Y_2 corresponds to the conductivity of the equivalent circular cross-section of the conductive channels.

Based on the assumption that the relative fraction of isolated and continuous pores – f_{isol} and f_{cont} respectively – are known, both bounds can be combined in a simple mixture law:

$$\frac{k(f)}{k_s} = f_{isol} Y_1(f) + f_{cont} Y_2(f) \qquad \textbf{Eq. II-11}$$

where f is the fractional porosity at a given weight loss. Since f is underestimated after the segmentation of the 3D images, the corrected value which is shown in Figure II-9 was preferred. However, the values of isolated and continuous pores were those estimated thanks to the IB method.

In order to estimate the influence of the morphology of isolated pores, the upper bound *Y1 of* the first model (Eq. II-11) is replaced in the second model (model 2) with an expression that mixes the three types of shapes – spheroid, prolate and oblate – specified in Section II.3.2.2.3. The expression follows the equation proposed by Meredith and Tobias [Meredith and Tobias 1962] which predicts thermal conductivity for randomly oriented ellipsoidal pores:

$$\frac{k}{k_s} = \left[\frac{2 - f^*}{2 + (W-1) f^*}\right]\left[\frac{2(1-f^*)}{2(1-f^*) + W f^*}\right] \qquad \textbf{Eq. II-12}$$

where

$$W = \frac{1}{3}\left(\frac{1}{2S_F} + \frac{2}{1-S_F}\right) \qquad \textbf{Eq. II-13}$$

where f^* is the volume fraction of a type of the isolated pore and S_F a shape factor depending on the aspect ratio F_{ab} (F_{ab} – S_F curve can be found in [Cernuschi et al. 2004]).

The results derived from both models have been also compared with the experimental measurements of thermal conductivity that the author carried out using a laser flash technique [Parker et al. 1961]. One can see from Figure II-16 which compiles data for the WG and AG samples that the models consistently underestimate the experimental data, but give a good estimation of the experimental trends. in particular, the model predicts that a transition will occur between the upper bound behaviour (i.e. mostly isolated porosity) to lower bound behaviour (mostly connected porosity) with increasing weight loss by thermal oxidation, due to the change in the relative proportion of isolated and continuous porosity. These results are in agreement with the study by Brocklehurst et al. [Brocklehurst et al. 1970], which showed that the thermal conductivity changes observed with radiolytic oxidation could not be accounted

for by considering only the isolated porosity. That analysis assumed that radiolytic oxidation occurred due to the enlargement of pores, and that the relative proportion of isolated and continuous porosity was constant. This analysis of thermal oxidation by X-ray tomography shows that the ratio of isolated to connected porosity changes with weight loss. However, no experimental estimation of the fraction of continuous porosity in radiolytically oxidised graphite has yet been reported.

The predictions of extended model (model 2) are similar to those of the Euler model (model 1) for the WG and AG samples, with a tendency to underestimate the thermal conductivity. The similarity is due to the lack of significant variation in the relative proportions of pore shapes between the different samples, and the large fraction of spheroid pores compared to the other classes (average relative fractions from WG and AG samples: $\langle f_{spheroid} \rangle = 0.75$, $\langle f_{prolate} \rangle = 0.15$ and $\langle f_{oblate} \rangle = 0.1$). It is worth noting that Eq. II-12 is relatively insensitive to the value of the shape factor S_F for $0.2 < S_F < 0.5$ (i.e. spheroid and prolate porosity) but it is sensitive to low values of S_F, corresponding to oblate pores. The model may therefore be of greater interest for the analysis of microstructures with a larger content of oblate pores, such as Gilsocarbon graphite.

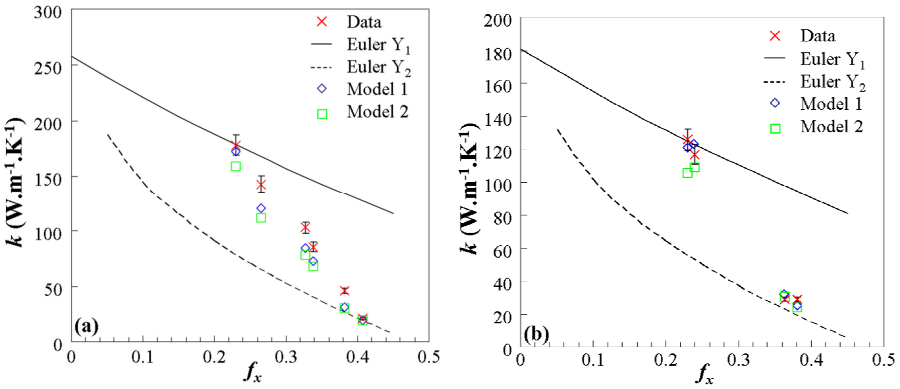

Figure II-16. Comparison between experimental thermal conductivity and the two porosity models for the PGA samples. (a) WG samples, (b) AG samples. Uncertainty bars of the experimental data are also displayed. Figures published in [Babout et al. 2008]

II.5. Conclusion

In this chapter, to the best of the author's knowledge, the first application of direct measurements of the detectable porosity content obtained using X-ray tomography to analytical thermal conductivity models has been presented. The porosity data obtained from the thermally oxidized samples of PGA nuclear graphite have been classified in two different families of continuous (or interconnected) and isolated porosity, using a new computational approach

called the ‘‘intersected branch method”. This method is based on the calculation of the intersection between a cubic box and a 3D feature. a sub-classification into three families has been also adopted to separate the shapes of features classified as isolated porosity. Because of the wide range of the porosity size and the weak contrast that may occur between porosity and graphite, a special approach has been used to select the segmentation threshold, based on the real density value and a decision making criterion to determine whether a voxel is mainly composed of porosity or of pure graphite.

A good agreement was found between experimental thermal conductivity data and the Euler-based model. Since this model only takes into account the relative volume fractions of isolated and continuous pores, it indicates that thermal conductivity is strongly sensitive to these fractions in the graphite tested. A transition in thermal conductivity may occur between an upper bound (isolated porosity) and lower bound (continuous porosity) with the increasing weight loss.

The comparison between the model and the experimental data suggests that the method is well suited to predict thermal conductivity changes resulting from thermal oxidation. The methodology might be usefully applied to other types of nuclear graphite with a more pronounced population of oblate pores, such as Gilsocarbon graphite. This could be also seen as a tool for the study of property changes due to porosity caused by radiolytic oxidation. Moreover, the methodology that has been presented in this chapter will be useful to study the effect of thermal oxidation on the mechanical properties, such as modulus and tensile /compressive strength, since it is known that these properties are very sensitive to the distribution of large pores. This could be also compared with FEM approaches.

At the present time, it is worth mentioning that a long-term collaboration between the MPC (School of Materials, The University of Manchester, UK) and the NRG (Petten, the Netherlands), is under way and aims at the characterisation over time, of the influence of radiolytic oxidation on a wide range of nuclear graphite samples. Two years ago, the author carried out X-ray tomography scans on the samples prior to their placement in a laboratory reactor and the next scan should be planned in a couple of years, after decontamination approval. This study will allow to carry out the direct statistical and morphological comparison on the same samples, with a particular task to investigate how the graphite microstructure, and particularly the porosity network, is affected by the neutron radiation exposure. Coupled with other physical and mechanical non-destructive measurements, this will offer a unique set of data to apprehend and monitor graphite behaviour during nuclear servicing.

III. BRIDGE LIGAMENTS DETECTION IN SENSITIZED STAINLESS STEEL DURING INTERGRANULAR STRESS CORROSION CRACKING

In the following chapter the novel strategy used to analyse a development of IGSCC in stainless steel with a special focus on bridge ligaments is presented, which is believed to play a fundamental role in the corrosion resistance of this material. This is a summary of the results presented in various papers [Babout et al. 2006a; Babout et al. 2006c; Marrow et al. 2006; Janaszewski et al. 2007; Babout and Janaszewski 2009; Janaszewski et al. 2009, 2010]. This work was initially carried out by the author at the MMSC. The author has actively participated in the X-ray microtomography experiment campaign which was organised at the ESRF and he was the main investigator of the corresponding 3D microstructural analysis. After his research period in Manchester as a PDRA, the author proposed to carry on the study at the CED (Technical University of Łódź) in order to strengthen the collaboration with the MMSC. The continuation of this study has focused on 3D image processing and has been done in collaboration with Dr M. Janaszewski. From Septembre 2009 to March 2010, the author had the opportunity to return to the MMSC within the frame of DENIDIA, a 4 year European project from the FP6 Marie Curie Transfer of Knowledge scheme coordinated by CED (Contract no.: MTKD-CT-2006-039546). He had the opportunity to use the algorithm presented in this chapter to further analyse quantitatively bridge ligaments in stainless steel and their failure evolution during IGSCC.

III.1. Context of the study

Austenitic stainless steels represent more than 70% of the stainless steel production and can be found in a myriad of applications ranging from major appliances, to construction materials for building facades (the pinnacle of New York's Chrysler Building being a famous example). They can also be found in more-advanced engineering applications, such as the ones used in aeronautics or in nuclear reactors. The considerable interest they arouse is mainly due to their corrosion resistance, favourable mechanical properties at low and high temperatures, ease of fabrication and a relatively low cost. Their corrosion resistance results from the ability to passivate, i.e. to generate a chromium-rich oxide film at the surface preventing it from environmental aggressions. However, passivity breakdown can occur in some environments and metallurgical conditions, resulting in localized corrosion phenomena, such as pitting and intergranular corrosion (see Section I.2.1). These problems have been observed in BWR and RBMK reactors where stainless steel is used in the core of the reactor [Ting 1999; Scott 2000]. Generally, IGSCC occurs in pipe

weldments and is due to the initiation of the crack in chromium-depleted regions of strained material [Ryan et al. 2002; Shimada et al. 2002; Wasnik et al. 2002; Takaya et al. 2004]. Intergranular stress corrosion cracking (IGSCC) of austenitic stainless steels can therefore occur as a result of chromium depletion at the grain boundary which is typically due to chromium-carbide precipitation [Gertsman and Bruemmer 2001]. The degree of susceptibility is mainly controlled by the extent of chromium depletion at the grain boundary [Wasnik et al. 2002].

The initiation and propagation of the IGSCC are both dependent on the grain boundary susceptibility, with the crystallographic structure playing a major role [Lin and Pope 1993; Lin et al. 1995; Palumbo et al. 1998; Trillo and Murr 1999; Gertsman and Bruemmer 2001; Shimada et al. 2002; Wasnik et al. 2002]. Investigations into the nature of susceptible grain boundaries are mainly based on a post-mortem crack path characterisation. From these studies it is clear that certain grain boundaries are highly resistant to IGSCC by disrupting easy pathways through the microstructure. This resistance has been correlated with lower energy states, due to the grain boundary structure [Trillo and Murr 1999; Kokawa et al. 2000]. However, little was known on how this disruption occurred for lack of techniques to investigate the bulk of materials. Surface observations of the fully sensitised stainless steel revealed the possibility of disruption by bridge ligament. Crack bridging is a common phenomenon in the brittle fracture of materials, such as ceramics [Marrow et al. 1993] or fibre reinforced composites [Bennett and Young 1997], whereby the isolated regions of the material link the opposing faces of a crack and restrict its opening. However, to the best of our knowledge, it has never been reported for stress corrosion cracking.

The study of IGSCC is very challenging due to the complex interaction between the microstructure, the environment and the mechanisms of localised corrosion and the environmentally assisted cracking. The present study has focused on the qualitative and quantitative characterisation of resistance to cracking by analysing bridge ligaments. For the sake of unambiguous characterisation of these material features and their evolution over time, the data was obtained in situ by coupling a stress-corrosion test with X-ray microtomography observations. The author has taken an important role in the set-up and the conduct of the experiment. The present study has been focused on the following points:

- Qualitative observation of the development and failure of crack bridging ligaments in 3D. The author has been the main investigator of this task.
- Segmentation of features in a 3D digital image which correspond to bridge ligaments for future quantification. The author has been the main coordinator of this task.

III.2. Material description and experimental setup

III.2.1. Material

Stainless steel 302 was used for the study since its composition is very close to that of the most common grade 304 applied in the nuclear industry. It has the same corrosion resistance and a higher strength, but most of all, it is most commonly found in strip and wire forms. The latter point is of a practical interest since the sample used for the experiment had a diameter of 400 μm.

Even though this material is corrosion resistant, the sample was fully sensitised at 650°C for one hour so as to produce chromium depletion. The wire was spot welded to 3 mm diameter steel grub screws to form a tensile specimen. The sample was lacquered, expect along 0.5 mm of length exposed to the corrosive environment. The sample was tested in 0.15 M potassium tetrathionate ($K_2S_4O_6$) (pH 2) since tetrathionate solutions are known to attack chromium depleted zones [Horowitz 1983].

III.2.2. X-ray microtomography and set-up

The results presented in this chapter have been obtained at the ESRF, on the ID19 beam line, described in Section I.2.2 (see Table I-1 for setup details). The distance between the sample and the detector was fixed at 40 mm in order to generate some phase contrast [Cloetens et al. 1997] (see Section I.2.2.3 for more details).

The specimen presented above was mounted in an environmental cell, within a specially designed 5 kN tensile machine, developed by J.Y Buffière and P. Michaud (MATEIS and GCP, INSA Lyon, France, respectively). The tensile machine base was fixed to a stage where rotation and translation can be precisely controlled. in the stress corrosion setup developed for this work, (Figure III-1), an inner PMMA tube (40 mm diameter, 2 mm wall thickness) is used as a solution container, while the second, larger one (70 mm outer diameter with 1 mm wall thickness) provides the load transfer between the lower and upper grips in the tensile machine. This system allows a full rotation of the device during a tomographic scan as PMMA is transparent to X-rays for the beam energy used (i.e. 30 keV).

The progress of the in-situ stress corrosion test was made in the following way (a more precise description can be found in [Babout et al. 2006a]): prior to loading, the sample was connected for a few seconds to a platinum cathode in order to polarise it, and to initiate stress corrosion. Cracking then propagated in the sample under an applied stress of approximately 100 MPa and open circuit conditions. Each tomography scan was performed under steady state conditions, obtained by simultaneously reducing the stress to 10 MPa and cathodically polarising the sample via a connection to a high purity aluminium anode.

Cracking was reinitiated by re-applying a higher stress under open circuit conditions.

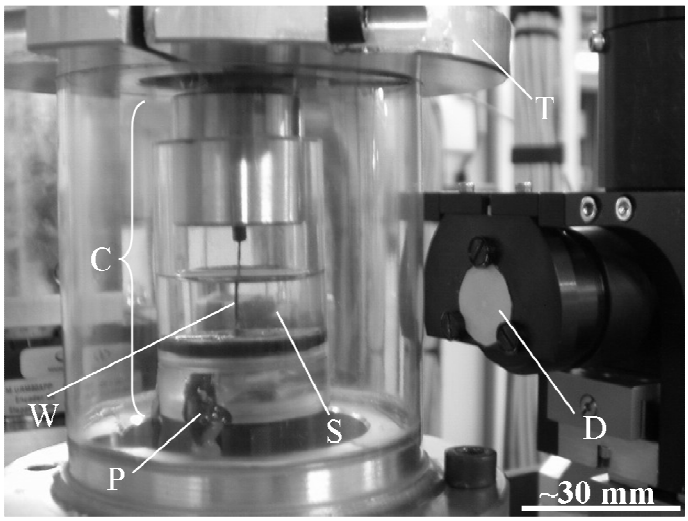

Figure III-1. X-ray microtomography set-up on ID19-ESRF. "W": 302SS wire, "P": platinum counter electrode, "C": environmental cell, "S": $K_2S_4O_6$ solution, "T": tensile machine, "D": detector. Figure published in [Babout et al. 2006a]

III.3. Experimental results

III.3.1. Qualitative observation of stress corrosion cracking and detection of bridge ligaments

III.3.1.1. Two dimensional sections of the crack path

The evolution of damage observed from the outer surface of the sample at the mesoscopic scale can be processed by 3D rendering of the material, after the virtual removal of voxels corresponding to the cracks. Figure III-2 shows the opening progress of two large cracks at three observation stages, which have initiated at two different heights of the wire and from the opposite side of the surface. This results in a large bending of the wire between the two cracks, as the strain increases, especially between steps 2 and 3 (corresponding to Figure III-2b and c, respectively). The propagation of the lower crack led to the failure of the specimen. This 3D representation gives a clear picture of the location and extent of cracking in the sample from the outside, but two dimensional sections of the material provide complementary information that allows one to analyse the interaction of the crack with the microstructure in the bulk of the sample.

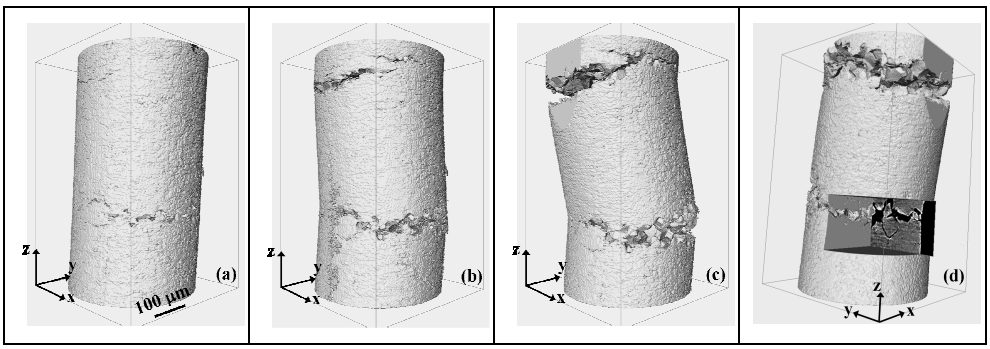

Figure III-2. 3D rendering of the sample wire showing the extent of intergranular cracking at the three observation stages. (a): scan 1, (b): scan 2 and (c): scan 3. The outer surface of the wire can be displayed by virtually removing the voxels corresponding to the crack. (d): rotation of (c) anti-clockwise around the z-axis which also shows a local clip of the isosurface to highlight the two dimensional sections of interest presented in Figure III-1. Figures published in [Babout et al. 2006a]

A sequence of images, which are the reconstructed slices of the same region of the sample in the three successive scans, are shown in Figure III-3. At scan 1, the image is 185 µm wide and 145 µm high. This region, which is also shown in Figure III-2d, corresponds to a radial slice normal to the x-axis around the lower crack identified in Figure III-2. These images demonstrate for the first time, to the best of our knowledge, the development of the intergranular stress corrosion crack in the specimen [Babout et al. 2006a]. a number of discontinuities in the two-dimensional images, denoted L1 to L4, can be identified. These can be shown to be bridges or ligaments linking the opposing faces of the crack using the Amira software [Visage Imaging 2008], by translating the viewing slice backward and forward around the regions of interest. For example, a set of slices at different x coordinates, around ligament L3 at scan 1, are presented in Figure III-4. The slice at the relative position "x = +7" corresponds to Figure III-3a. The sequence clearly shows that the bridge L3 links two crack regions C1 and C2, between the position "x = -3.5" and "x = +10.5". The sequence also reveals another bridge, noted L'3. It is worth mentioning that this method is fast and easy to use for detecting bridges, but like any manual inspection, is prone to error and misleading interpretations. As it will be seen later in this chapter, the development of a dedicated image processing algorithm is one way to reliably attest the presence of a ligament.

The progressive failure of the bridging ligaments at the different stages of the experiment can be observed using the same method. One can see in Figure III-3

that ligament L3 failed between the first and the second scan, L1 has failed between the second and the third scan, while ligament L4 is still present, but reduced in size. It also seems that L2 fails between the second and the third scan. However, a look at the evolution of the surrounding crack width between stage 2 and 3, compared to the one localised around L1 that dramatically increases, suggests that a ligament is still present.

The crack opening displacement of the main crack increases during the experiment, but the opening of the secondary cracks tends to remain constant, indicating that they are shielded from the applied stress. a detailed investigation by slice translation shows that these cracks may be arrested, e.g. at CA1, CA2 and CA3 (see Figure III-3c).

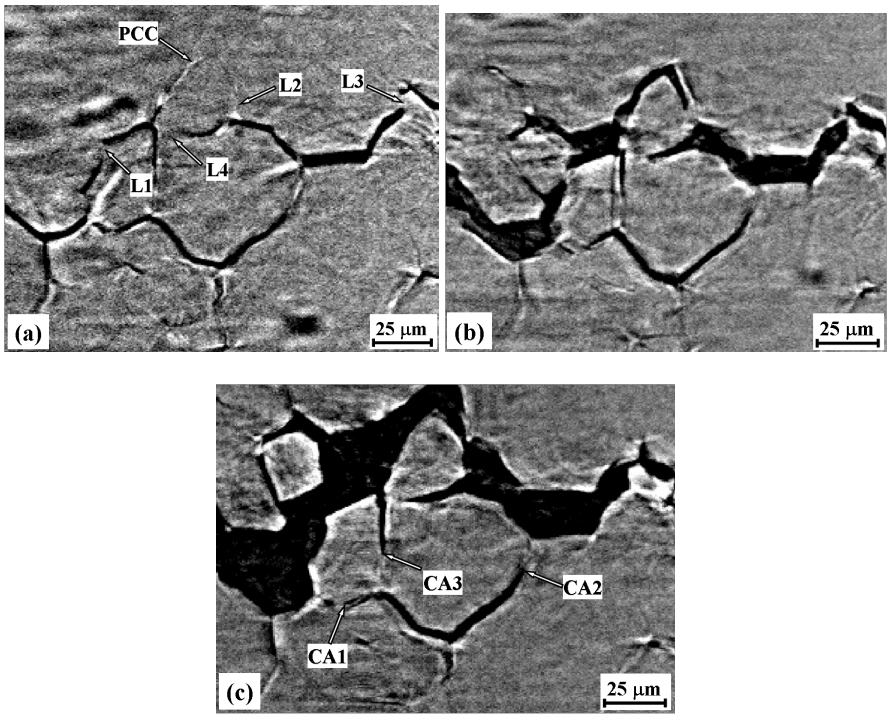

Figure III-3. Sequence of longitudinal sections at the same region in the wire, demonstrating the development of intergranular cracking. The insert in (a) shows the wire sample with lacquered zones (hatched) and the location of the sequence in the exposed zone. The tensile direction is also shown. (a): scan 1, (b): scan 2 and (c): scan 3. PCC indicates a sub-resolution Phase Contrast Crack in (a). Figures published in [Babout et al. 2006a]

Although most of the bridges are clearly distinguishable in Figure III-3a, L2 is less pronounced in scan 1 since the width of the crack above the bridge is small, compared to the spatial resolution. At that stage, L2 corresponds to a crack arrest rather than to a bridge ligament. However, the thin white fringe, generated because of the phase contrast [Cloetens et al. 1997] indicates a sub-resolution crack, which is labelled PCC (Phase Contrast Crack) in the figure. The significant white fringes around the wider parts of the other cracks also arise from the phase contrast. The width of this phase contrast layer increases with the crack size. It is also dependent on the distance between the sample and the detector [Cloetens et al. 1997]. Although phase contrast is useful to identify sub-resolution cracks, it also causes grey level saturation around the well defined parts of the crack path, which can influence the automatic segmentation of the data. However, in general, the fringe width does not exceed 5 µm, which is reasonable, compared to the spatial resolution of 0.7 µm. The selected distance of 40 mm therefore appears to have been a good compromise. a shorter distance could not be achieved because of the outer Perspex tube of the tensile stage.

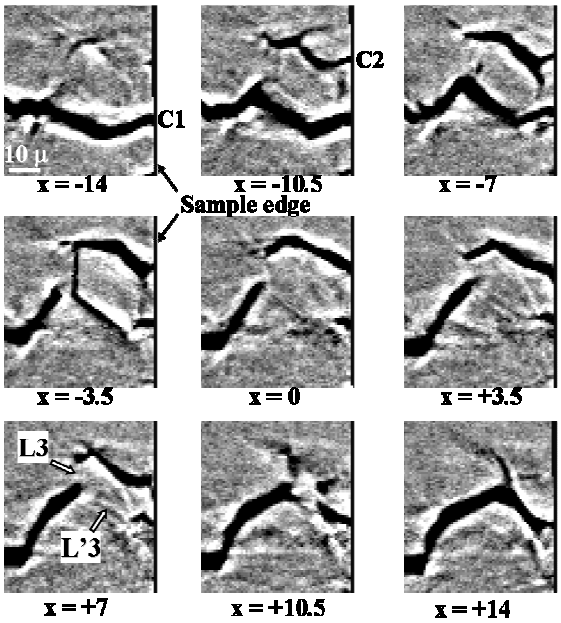

Figure III-4. a series of 9 reconstructed slices around ligament L3 (defined in Figure III-3). The relative position of each slice is given in µm. The relative position "x = +7" corresponds to Figure III-3. C1 and C2 are regions of the crack. Figures published in [Babout et al. 2006a]

III.3.1.2. Three dimensional visualisation of the crack path

The 2D reconstructed views reveal most of the information needed to study bridging ligament development and failure during stress corrosion cracking. A three-dimensional visualisation further assists the interpretation of the crack path and the ligament shape and size. However, the visualisation of a large volume can be difficult to achieve, because of the complexity and tortuosity of the crack path. For this reason, only selected ROIs were analysed in detail. The 3D isosurface rendering of the material from scans 2 and 3 around ligaments L1, L2 and L4, which are defined in Figure III-3a, is shown in Figure III-5. The selected volume had the dimensions 40 x 90 x 120 µm along the principal directions (x,y,z). The cracks were made transparent by removing their low attenuation voxels via the segmentation of the data set. The visualisation of sub-resolution cracks, detected by phase contrast, cannot be easily achieved by such segmentation but can be done by manual inspection of the data. This was not necessary in the selected volume because no sub-resolution cracks were observed.

Seven features, which are deduced from their shapes to correspond to different grains, are numbered in Figure III-5a. The ligaments L1 and L4 and crack arrest locations CA1 and CA3 (observed in Figure III-3) are also identified, as is a number of other ligaments indicated by dashed arrows. The three dimensional visualisation shows more clearly the range of bridging ligament morphologies. The ligament L1 is a small region located at the junction of grains 1 and 5. The ligament L4, between grains 2 and 3, spans the length of their boundary in the *x* direction, over a distance of approximately 30 µm with a curved shape. This can be visualised by observing in Figure III-5b the truncated oblique slice ABCD, defined in Figure III-5a, around the ligament. The failure of ligament L1 between the second and the third scan can be observed, whereas L4 is shown to remain intact, although reduced in size.

The complex failure sequence along the grain boundaries in three dimensions can be illustrated by observing the cracking development around L2. It lies between grains 2 and 7, and is shown in the oblique slice EFGH. The location of this slice is defined in Figure III-5a and Figure III-5d for scans 2 and 3, and the slice is shown in Figure III-5c and Figure III-5f. The location of ligament L2, defined in Figure III-3b, is indicated in Figure III-5c (black line). The pattern of cracking around the ligaments shows that there is an interaction with two further grains. These are identified as grains 8 and 9 in Figure III-5b. a possible boundary between grains 2 and 8 is marked by a dashed curve in Figure III-5c. Although the 2D slice investigation suggested that L2 was a bridge ligament, the combined use of the oblique view with the 3D rendering contradicts this observation. in the same manner, the failure of L2, which was suggested from Figure III-5c, is the subject of controversy since the oblique slice shown in Figure III-5f still reveals a portion of the material at the position of L2.

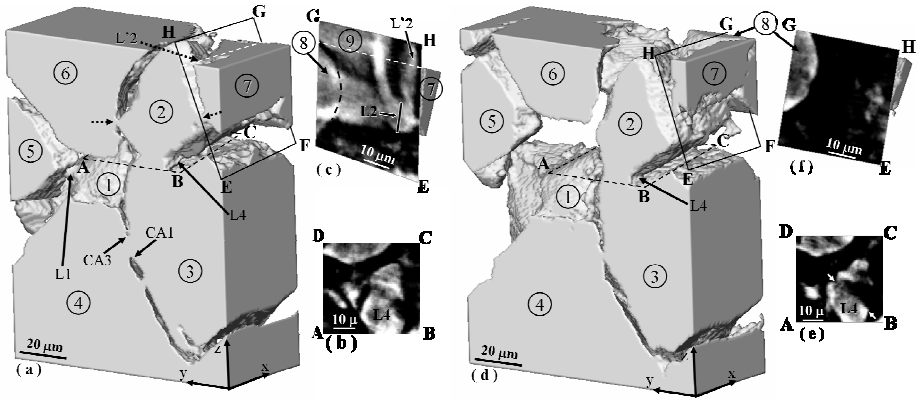

Figure III-5. 3D rendering of a region of interest (ROI) around ligaments L1, L2 and L5 at scans 2 and 3. (a): scan 2 showing 7 different grains and other ligaments (dashed arrows). (b): The oblique slice ABCD displayed on (a) containing L2. (c): The oblique slice EFGH displayed on (a) containing L5. (d): scan 3 showing the same grains of (a) after ligament failure. (e): The oblique slice ABCD for scan 3. (e): The oblique slice EFGH for scan 3. Figures published in [Babout et al. 2006a]

III.3.1.3. Conclusion regarding qualitative observations

The following conclusions can already be drawn based on the results presented above:

- The 2D slice translation is an effective tool to rapidly analyse areas and to detect features of interest in the volume (in the case presented – bridge ligaments). However, the judgment can be prone to error when the feature has a complicated shape and spans over a wide number of slices.
- In ambiguous cases, the 3D isosurface of a volume surrounding the feature of interest, coupled with the use of oblique slice translation can help in the bridge detection. However, because of the complexity of the crack path, only small volumes can be selected, which makes the qualitative analysis quite long-lasting.
- In both cases, the detection is merely qualitative and the estimation of feature properties can only be done manually, which is also very time-consuming.

Automatic detection is therefore the most appropriate solution to both unambiguously localise the bridge ligament and extract the morphological properties relevant for the study, e.g. size, shape and orientation of ligaments and also width of the surrounding crack. The description of the possible approaches and algorithms that have been implemented is presented in the next section.

III.3.2. Quantitative analysis of bridge ligaments

III.3.2.1. Which notion describes best a bridge ligament: notion of a hole

A better way to visualize a bridge ligament is actually to render the voxels that correspond to the crack. However, the processing of the full crack isosurface is far more difficult to obtain than that of the solid material shown in Figure III-2, because the crack, which initiates at the surface of the sample, must be labelled differently than the connected surrounding air, which presents a similar grey level value (i.e. zero attenuation). Simple volume cropping is not possible because of the cylindrical shape of the sample. Therefore, the author has applied another method [Babout et al. 2006c]. It consists in selecting, at two different heights of the sample surrounding the crack, three points along the corresponding perimeters in order to calculate the respective radius and coordinates of the centre. in the case of a non-bent part of the cylinder, intermediate radius and centre coordinates can be easily interpolated from this set of parameters. Then, an Euclidean distance criterion is used to classify background voxels as part of the crack label if the distance to the centre is smaller than the radius at the given height of the given voxel. Under the supervision of the author, a new algorithm has been recently developed [Kornev et al. 2010], based on oriented anisotropic Gaussian filtering and continuous maximum flows [Appleton and Talbot 2006], that is more robust and efficient than the previous algorithm. Indeed, it is not dependent on the shape of the original 3D object and can deal with non a convex object such as a bent beam. Moreover, it generates a minimal surface that both encloses the original 3D object and the crack, so that the latter one can be easily separated from the surrounding air.

One can see from Figure III-6 that bridge ligaments correspond to “holes” in the crack. Even if they are clearly distinguishable, holes themselves do not correspond to features that can be detected using connected components search algorithms (from the topological point of view, a hole is not a subset of the 3D space). a definition of the detection of a 3D hole can be found in [Kong 1989]. According to the definition, the presence of a hole in an object O is detected whenever there is a closed path of voxels in O that cannot be deformed into a single voxel. The following section describes two methods that have been considered in order to detect the holes.

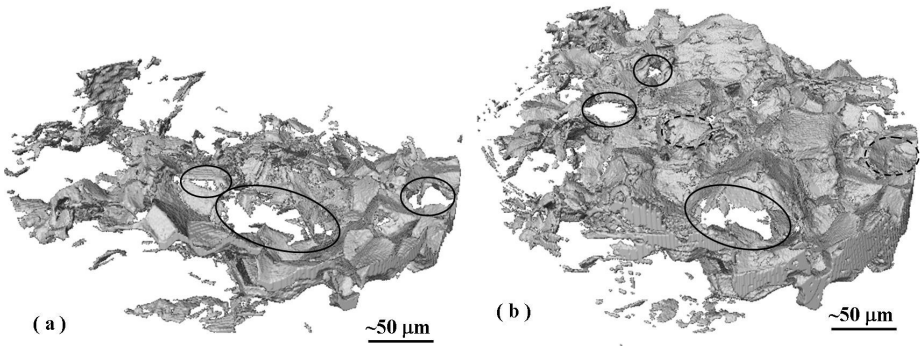

Figure III-6. 3D rendering of crack (a) scan 1 (b) scan 2. Continuous and dashed ovals locate bridges and bridge failure, respectively. Figures published in [Babout et al. 2006c]

III.3.2.2. First approach to detect a hole using SS coding: advantages and limitations

The first approach to be developed [Janaszewski et al. 2007] was based on the following microstructural observation: when a crack encounters a bridge, it splits into two branches, then merges again where the bridge ends. in a similar manner, a set of connected points forming a 1D or 2D curve that "moves" toward a hole will split into two new sets of connected points when a hole is crossed, then merge again when the hole is passed.

The simulation of the movement of the crack can be processed using voxel-coding [Zhou and Toga 1999], a recursive voxel-by-voxel propagation and assignment of values to voxels within a volumetric object O starting from a seed voxel S. The purpose of voxel-coding procedure is to extract geometric features of objects and it was extensively exploited earlier, e.g. [Borgefors 1986; Niblack et al. 1992]. The values are defined on the basis of the type of neighbourhood of the voxels surrounding the seed, or more generally, of the voxels surrounding each voxel coded during the previous iteration step. in a classical cubic grid, three types of neighbours are defined: F-neighbours which share a face, E-neighbours which share an edge and V-neighbours which only share a vertex with a given voxel. The coding is similar to a discrete minimum distance transform. It follows the following scheme, assuming that a voxel p of the object O has been coded with the value n during the last iteration. a voxel q of O, neighbour of p, will have its value increased by 1, 2, or 3 if and only if it is a F-, E- or V-neighbour of p, respectively, and the new value is lower than the actual one. The last rule is necessary to avoid redundant recoding. The coding is completed when there is no more voxels to be processed, or a special constraint is met (for instance, a particular voxel has been met). An example of such voxel-coding is shown in Figure III-7.

The voxel-coding transforms an object into a collection of clusters. a *cluster* is defined as a set of connected object voxels of the same voxel-code. in addition, some cluster types of great importance can be considered. a *merging cluster m* is a cluster which has more than one neighbour with the same code value of one less than *m's*. The *m's* neighbours of code one less are called *predecessors* of *m*. a *dividing cluster d* is a cluster which has more than one neighbour with the same code value of one larger than *d's*. The *d's* neighbours of code one larger are called successors of *d*. This is illustrated in Figure III-7 where clusters 9 and 10 are dividing clusters since they present two successors of value 10 and 11, respectively.

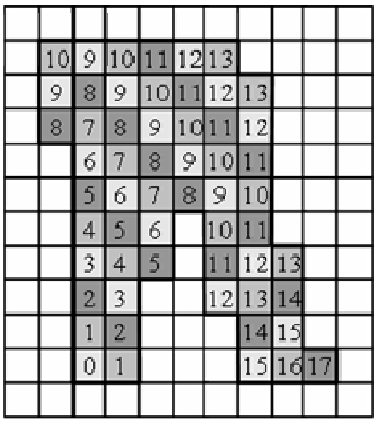

Figure III-7. Illustration of voxel coding on artificial 2D image. The seed point for the coding propagation has value 0. Clusters 9 and 10 are dividing clusters. No merging cluster detected. Figure published in [Janaszewski et al. 2007]

Drawing on the previous definition, a dividing cluster will detect the beginning of a hole in the crack, and a merging cluster, its end. However, the second feature is the only reliable one to detect the bridge since the dividing cluster can also detect branches, as shown in Figure III-7.

The method works relatively well in bridge detection, as shown in Figure III-8, because the clusters have a ribbon-like shape that is not so large, compared to the size of the bridge. The detection method could encounter some problems in the case of a cluster far larger than the bridge. in such a situation, the bridge will not divide a cluster into two, but just generates a hole inside it.

Despite promising results, the method was abandoned for the following reasons:

– the method only detects bridges, but fails to localise them. It is possible to localise the bridges more precisely by iteratively retrieving the predecessors between a merging cluster and a dividing cluster. Indeed, a merging cluster determines the occurrence of at least two paths of adjacent clusters which end in one common dividing cluster. The location can be based on the

construction of a graph in which the dividing and merging clusters correspond to the nodes and paths of consecutive clusters which, in turn, connect the merging and dividing clusters from the edges of the graph. a more complicated step afterwards would be to extract, from the corresponding paths, the border voxels that surround the hole.

- Another issue is that a merging cluster may detect more than one hole when the number of predecessors is larger than 2. Another similar difficulty will arise when a cluster from the path is also a merging cluster, as it can be seen in Figure III-8. a selection of the border voxel will be evidently more complicated.
- Assuming that the extraction of border voxels has been performed, the last difficulty resides in selecting the voxels of the holes. This can be done using the approaches based on Dijkstra's shortest path algorithm [Cormen et al. 2001] between all the voxels surrounding the hole, but this method does not guarantee that the process will accurately fill the hole.
- The main reason for rejecting the development of this algorithm is rather more personal. The author has had the chance, together with Dr M. Janaszewski, to collaborate with Prof. M. Couprie from the A3SI laboratory (ESIEE, Paris-France) within the DENIDIA project. This laboratory is a leading centre in the field of discrete geometry and 3D image processing. Dr M. Janaszewski had the privilege to do research in this laboratory for 6 months. During this time, a hole closing and filling algorithms were being developed. As a co-author, but the main designer of the work, the author will only present the main characteristics of the approach, discussed in the next sections.

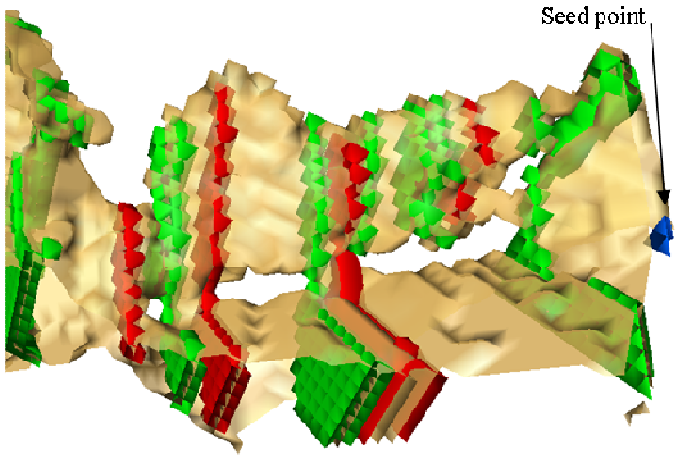

Figure III-8. Illustration of bridge detection using voxel-coding. The crack is in yellow, the seed point in blue, the dividing clusters in green and the merging clusters in red

III.3.2.3. Hole closing and filling using a discrete geometry approach

III.3.2.3.1. Topological notions

The different algorithms that will be presented later in this section are based on topological notions [Kong and Rosenfeld 1989]. The most relevant one that is central to our approach is the notion of topological number, introduced by Bertrand [Bertrand 1994; Bertrand and Malandain 1994]. This is the calculation of the number of connected components in the geodesic neighbourhood of a particular voxel p being disregarded. This number is calculated both for an object O ($T_{p,O}$) and for the background B ($T_{p,B}$). One important rule to remember is that the connectivity that is used for the foreground and the background has to be different so as to avoid what is called "connectivity paradox" [Kong and Rosenfeld 1989]. The geodesic neighbourhood is an important parameter for the topological number calculation since it predefines which neighbours of p in O (or B) are considered (e.g. F-, E- or V- neighbors). Bertrand has shown that the geodesic neighbourhood actually depends on the combination of connectivity used for the foreground and background [Bertrand 1994]. For 18- and 26- connectivity, the geodesic neighbourhood takes into account all types of neighbours. However, the 6-connectivity for O (or F) associated to 18- or 26-connectivity for F (or O) will give rise to different geodesic neighbourhoods:

- 6 with 18: all types of neighbours of p in O (or F) are considered (e.g. F-, E- and V- neighbors).
- 6 and 26: F-and E-neighbours of p in O (or F) are taken into account.

A set of special points can be defined based on their topological numbers [Malandain et al. 1993]:

- interior points and border points will have $T_{p,B} = 0$ and $T_{p,B} \neq 0$, respectively.
- 1D- and 2D- isthmus points will have $T_{p,O} \geq 2$ and $T_{p,B} \geq 2$, respectively.
- simple points will have $T_{p,O} = 1$ and $T_{p,B} = 1$.

The latter type of points is actually of a great importance in the hole closing an algorithm since deleting these points does not change the topology of the object of interest. This is an important property worth considering during image transformation (e.g. thinning transformation) which must preserve some topological features.

III.3.2.3.2. Hole closing algorithm

The algorithm of hole closing was actually developed by Aktouf et al. [Aktouf et al. 2002]. It is mainly based on the notion of a topological hull that can be simply described as follows: it is a subset of the space S containing the object of interest O and in which each point is an interior point or a 2D isthmus for S. The method deletes simple points from a bounding box that contains O which are not interior points and 2D isthmus, from the furthest point to the closest one of the object O using an ordering list based on Euclidean distance. The procedure is repeated until idempotence. An illustration of the approach is shown in Figure III-9. Each pixel (or point) in the images is represented with 3 numbers in the following subscript notation: $_{T_{p,B}}D_{T_{p,O}}$, where D is the squared Euclidean distance from the closest point of the object O. Figure III-9c shows that after the deletion of points with a distance equal to 18,13, then 10, one point at distance 9 becomes a 1D/2D isthmus and therefore cannot be deleted. The deletion procedure continues until all the points that connect the two parts are non-simple points.

The method has shown some limitations in the closing of the hole when irrelevant branches which are close to the hole may significantly alter the shape of the hole. For this reason, the original algorithm has been modified in the following way [Janaszewski et al. 2010]:

- step 1: application of the standard hole closing algorithm from Aktouf et al.,
- step 2: geodesic dilation of the hole closed in the previous step,
- step 3: application of the UHSA [Couprie et al. 2007] on the hole contour. The UHSA sequentially deletes simple points from the input object until stability. In this way it deletes all branches of the input object,
- step 4: second application of the standard hole closing algorithm on the new hole contour, free of defects.

At this stage, the holes are closed and the principal objective of the procedure is met; thus, the bridge ligaments can further be characterised. However, another step of the algorithm has been devised in order to fill the holes so that it becomes a signature of the crack thicknesses that surround them.

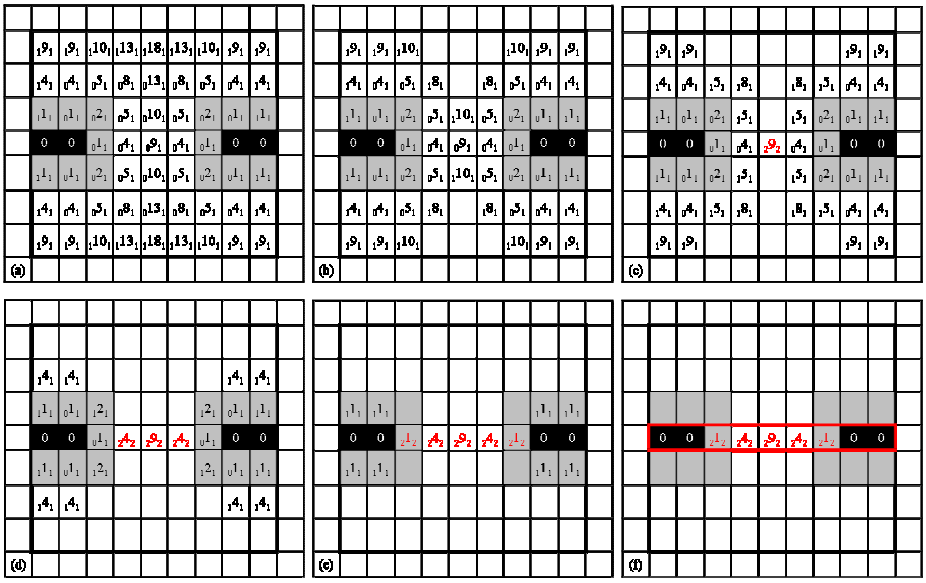

Figure III-9. 2D illustration of topological hull algorithm applied to the medial axis (black) of an object (grey). (a) Squared Euclidean distance map that also shows the topological numbers at each point for the object (the bounding box) and the background. (b) Deletion of simple points for distances 18, then 13. (c) Deletion of simple points for distance 10. First non-simple point (in red) after recalculation of the topological numbers. (d) Deletion of simple points for distance 9, 8 then 5. (e) Deletion of simple points for distance 2. (f) Deletion of simple points for distance 1. The set of points included in the red rectangle corresponds to the topological hull. Figures (a), (c) and (f) published in [Babout et al. 2010a]

III.3.2.3.3. Hole filling algorithm

The concept behind the hole filling algorithm is that a filling volume should fit the shape of the corresponding object's hole in the same way the two pieces of a puzzle match each other. To do so, the algorithm has been designed with the following steps:

– step 1: filtered Euclidean skeleton [Couprie et al. 2007]. This step extracts the skeleton of the object (the crack) with two special constraints: the points which compose the medial axis [Remy and Thiel 2005; Saúde et al. 2009] of the object, and a bisector angle criterion [Couprie et al. 2007] that actually selects a set of points that the skeleton needs to consider. in such a way, the skeleton is homotopic to the object and it is only composed of non-simple

points. Each point of the skeleton is represented by its closest distance to the background (this, in other words, corresponds to the radius of the maximum ball, centered on the point that fits inside the object);

- step 2: the hole closing of the previous section is applied to the skeleton;
- step 3: this step realises the propagation of the thickness of an object represented by the values of its filtered skeleton voxels into hole closing patches. The algorithm, at each iteration step, calculates a new value for each voxel of a hole closing patch as an average value of voxels from its neighbourhood which belongs either to the hole closing patch itself or to the filtered skeleton, until idempotence;
- step 4: for each point of the hole closing patch, the surrounding background voxels which remain at the Euclidian distance smaller than the value of the point are added to the object. Thus, the volume of the hole, constrained by the surrounding object, is filled.

An exemplar of the algorithm on a portion of the crack at scan 2 is shown in Figure III-10 which corresponds to a part of Figure III-3 situated around ligaments L1 and L4. This has been presented in [Babout et al. 2010a]. Portions of the Euclidean filtered skeleton and holes closed and filled are superimposed to the original image, in grey, light grey and white colours, respectively (Figure III-10a). The isosurface highlights the location of the holes after the hole closing algorithm along the crack (Figure III-10b-c). One can see that the holes are correctly closed. An example of the hole filling result, corresponding to ligament L4, is shown in Figure III-10d where one can see that the thickness is larger than one voxel (this is also very clear in Figure III-10a). One can also see from these results that the ligament L2, supposedly detected using 2D visual inspection, is not retrieved by the algorithm, confirming what was guessed from the 3D inspection. However, a hole has been closed, as shown in Figure III-10b, which has not been detected from the 2D visual inspection. All these results, put together, show how the approach of hole closing/filling provides priceless information about the crack development and its interaction with the microstructure.

Closing and filling holes is one issue. Correlating them with microstructural information of stress corrosion cracking and bridging ligament is another. The discussion about this correlation makes the objective of the following section.

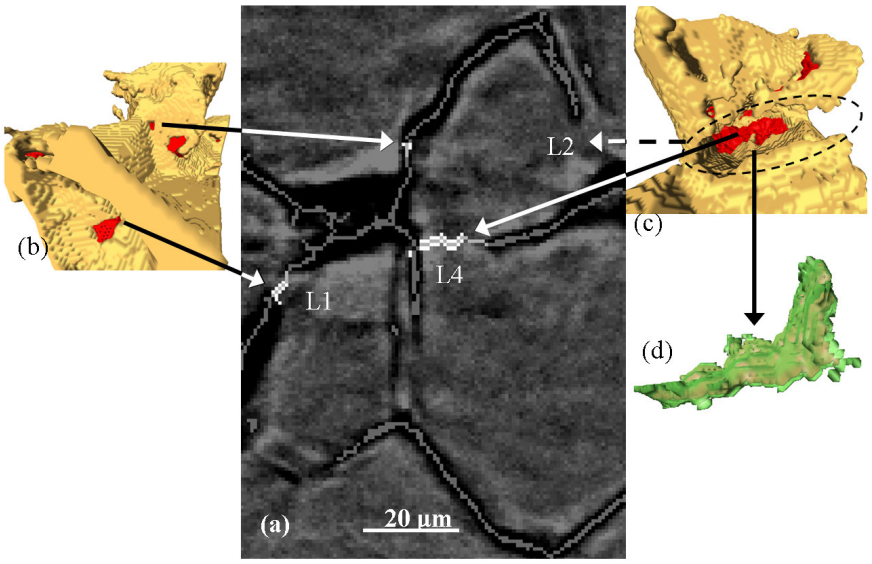

Figure III-10. Illustration of hole closing/filling algorithm on scan 2(a) zoom view around ligaments L1-L4 shown in Figure III-3. Skeleton of the crack (grey), holes closed (light grey) and filled (white) are also displayed (b) 3D rendering of the crack portion (yellow) surrounding L1 (red). Another bridge, located above L1 and L4 in (a) is also shown. (c) 3D rendering of the crack portion (yellow) surrounding L2 (red). Note that the portion of the crack which supposedly corresponded to L1 is not closed (dashed ellipse). L1 is therefore not a bridge. (d) superposition of the hole filling volume (green) on the hole closing patch corresponding to L4. See how it is thicker than the corresponding closed hole. Figures published in [Babout et al. 2010a]

III.3.2.4. From a hole to a bridge: considerations and analysis

The hole filling method processes a variety of objects that can actually be correlated to microstructural features (see Figure III-10):

- closed holes correspond, in theory, to grain boundaries that have not failed,
- the average thickness of the filled holes is associated with the thickness of the surrounding cracks and therefore linked to a parameter that reflects the crack opening displacement.

However, detecting a hole does not necessary mean that a real bridge is localised. Indeed, small holes can result from noise in the 3D image. Likewise, very large holes with a large tortuosity have nothing in common with the bridge ligament that usually corresponds to a small percentage of a grain boundary between two adjacent grains. For instance, trapezoidal and triangular ones are believed to be the two most frequent types of bridge shapes, the former being located between two twins forming on a single grain face, and the latter forming at a triple junction [Bystrzycki et al. 1993; Mahajan et al. 1997]. It is therefore

important to classify the holes in terms of their shapes and sizes, and only consider those which can be potentially regarded as bridges. After the inspection of the data, only the holes with a size comprised between 10 and 1500 voxels are retained. However, large holes of complicated shapes can actually result from the connections between smaller ones, which obviously makes the analysis more difficult.

This problem is illustrated in Figure III-11 where one can see that three holes, from which two may correspond to real bridges, are connected via thin isthmuses. Some of these junctions are probable, from the microstructural point of view, since an isthmus can occur at a junction of multiple grain boundaries. However, it can also happen that the crack is smaller than the spatial resolution and cannot be resolved between the bridges, resulting in such a thin connection. Therefore, an algorithm has been developed to detect the small isthmuses and delete them when appropriate. a detailed description of the approach can be found in [Babout and Janaszewski 2009]. The approach searches for points which correspond to 1D-isthmuses (e.g. point with topological number $T_{p,O} \geq 2$). Points are only deleted if one of the new features after separation has a volume larger than a threshold value (typically 5-10 voxels). This volume condition is set to avoid deleting thin objects. The main problem from this approach is that it does not treat larger isthmuses, as the one encircled in Figure III-11. This is one of the prospective works listed in the conclusion.

The data corresponding to the bridge ligaments in IGSCC can now be analysed in a more quantitative way. It is worth mentioning that this analysis has already began. An article has even been submitted to present results of bridge failure process over several tomography datasets, but also of the bridges that are detected along the main crack that propagated to the failure of the specimen [Babout et al. 2010b]. No more detail, except the one mentioned in the following section, are given since the article hasn't been accepted for publication yet.

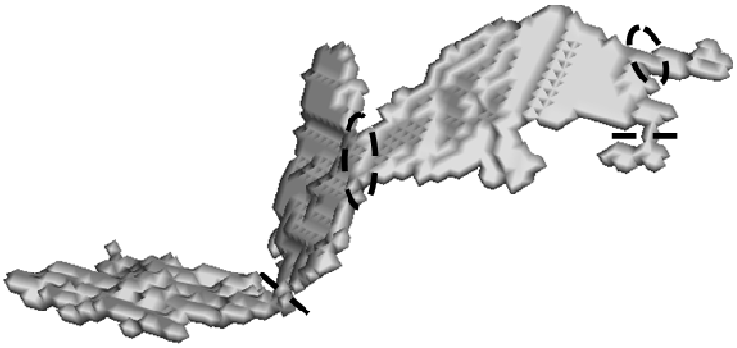

Figure III-11. Example of hole object with multiple 1-voxel thin connexions, also known as isthmuses (dashed lines). Encircled connexions present a larger width. Figure published in [Babout and Janaszewski 2009]

III.4. Conclusion and future work

This chapter has presented the unique results of the in situ observation of intergranular stress corrosion cracking in austenitic stainless steel, one of the standard materials used in the nuclear industry. One main focus of the study carried out by the author was to investigate, using X-ray microtomography, the development of bridge ligaments created along the intergranular crack path, in both a qualitative and quantitative way. The author has revealed that a qualitative inspection alone can lead to the erroneous detection of ligaments even during the coupling of traditional 2D viewing with 3D rendering. This finding led to the development of an algorithm to segment bridges based on a discrete topology approach. The author has been the main supervisor of this work. This method allows one to close holes in finite objects, as a bridge along a crack path actually corresponds to a hole. It constitutes an improvement over the previous version which can deal with the complexity of the input object, e.g. intergranular stress corrosion crack, but also defines the thickness of the hole, based on the thickness of the surrounding crack. Even though this information has no microstructural meaning, as a bridge corresponds to a grain boundary that has not failed during the crack propagation, hence it is a 2D surface, it can be correlated with a crack opening displacement.

Work is now in progress by the author to characterise the shapes, sizes and orientations of the bridges and their evolution as IGSCC develops. This considers a set of nine X-ray microtomography scans obtained during a new in situ IGSCC experiment. The novelty of the experiment has resided in the acquisition of a DCT scan [Johnson et al. 2008] (see Section I.2.2.3) before exposure of the sample to the corrosive solution. The technique provides valuable information about the crystallographic properties of the material, including grain boundaries and bridge ligaments [King et al. 2008] along the main crack that propagated to the failure of the specimen. Crystallographic properties of the bridges can be compared with the geometric ones mentioned above in order to further attest which ones may control the presence of the bridges during IGSCC in austenitic stainless steel. The unique comparison is under way in collaboration with the MMSC, which provides the data from both X-ray microtomography and DCT. Preliminary results on the quantitative analysis of geometrical properties of the bridges have been recently submitted by the author for publication [Babout et al. 2010b]. Meanwhile, a review article of which the author is a co-author, has been published in Decembre 2010 [Ludwig et al. 2010]. It focuses on the characterisation of polycrystalline materials by combined use of synchrotron X-ray microtomography and diffraction techniques such as DCT. It also has presented the first results of crystallographic properties of the bridges detected on the fracture surface of the sample and extracted using hole closing algorithm. The first analysis tend

to reveal that the bridging grain boundaries are associated with the presence of twinning in a grain, although they are not themselves low misorientation boundaries. The last stage of the study will be to combine all the data in a polycrystalline finite element model that has been developed by Jivkov et al. [Jivkov et al. 2006] to predict the crack propagation, with the final aim of better comprehension and improvement of the corrosion resistance in austenitic stainless steel.

IV. EFFECT OF LAMELLAR MICROSTRUCTURE IN TITANIUM ALLOYS DURING IN SITU FATIGUE TEST

The previous chapter has presented a typical example where the need to develop a new advanced 3D image processing algorithm to extract special features, such as holes in a crack was necessary in order to further analyse their effects on the mechanical/physical properties of the material. in the two previous chapters, the algorithms are applied to 3D binary images, assuming that all the features that need to be post-processed, are correctly segmented in the original grey-level input image. This is actually a situation that is the most frequently encountered in materials science applications of X-ray tomography. However, it may happen that the pre-processing segmentation is either obsolete or helpless because the features that need to be extracted from the image show a very complicated pattern. This is the case of e.g. textured images where the feature follows a given pattern, rather than it is differentiable from the rest of the image due to its specific grey level. Texture analysis has been mainly devoted to applications such as remote sensing, medical imaging, industrial inspection and document processing. However, some material microstructures, such as the one presented in this chapter, are good candidates for this methodology.

This chapter presents first attempts of the texture segmentation of lamellar colonies in titanium alloys. The results linked to the characterisation of mechanical properties of such alloys during monotonic/fatigue loading, as well as the 3D microstructural characterisation have been published in several proceedings and journal papers [Babout et al. 2004b; Babout et al. 2006c; Babout et al. 2009; Jopek et al. 2009; Birosca et al. 2010]. The author was the main coordinator and investigator of this work, when it was carried out at the MMSC. More precisely, this has concerned the preparation of *Ti-64* samples (including heat treatments), conduct of in-situ experiments during optical microscope and first X-ray microtomography observations, analysis and interpretation of experimental results. The work, that he has initiated, has later been carried on by Dr M. Karadge and Dr S. Birosca at the MMSC. Meanwhile, it has also been carried on at the CED of TUL, with a particular focus on image processing.

IV.1. Context of the study

Two-phase $\alpha + \beta$ Ti alloys are widely used by the aerospace, power generation and biomedical industries because of their excellent mechanical and corrosion resistance properties in addition to their relatively low density. The final microstructure of titanium alloys is largely controlled by the thermomechanical processing route. For applications where damage tolerance is required, the production of a fully lamellar microstructure enhances the fracture toughness

[Lutjering 1998; Lutjering and Williams 2007], which is achieved by processing the material above the β-transus. in addition, the cooling rates applied at the end of such a process play a defining role in terms of lamellae width, colony size and shape. It is believed that the most influential microstructural parameter on the mechanical properties of a fully lamellar microstructure is the α colony size, because it determines the effective slip length [Lutjering and Williams 2007]. For instance, applying high cooling rates results in a small colony size or eventually in a basket-weave structure, which increases the yield strength of the material [Lutjering 1998; Schroeder et al. 2001; Lutjering and Williams 2007]. Ductility is also influenced by the colony size, but also by the difference in strength that occurs between 'strong' fine martensitic lamellae and relatively 'weak' α layers on the former β grain boundaries [Lutjering 1998]. The crystallographic texture of the material also strongly affects the mechanical properties in those cases when Ti alloys are subjected to monotonic tension or fatigue. Indeed, studies showed that the colony microstructure in α + β Ti alloys exhibits the slowest crack growth rate, while the fastest rates are found in a fine-grained equiaxed microstructure [Sarrazin et al. 1994; Sarrazin-Baudoux 2005]. Many of these aspects are related to the crystallographic anisotropy of the hcp crystal structure of the α phase, with the ‹a› slip significantly easier than ‹c+a› slip [Lutjering and Williams 2007].

Most of the studies listed above have considered microstructural and crystallographic effects on materials properties. The aim of the present study was to focus on local aspects of the above-mentioned effects, and look more closely at the effect of both phases, α lamellae and remaining β grain boundaries on short crack propagation, but also on stress concentration at the level of the α colony. in order to characterise short crack propagation unambiguously, in situ fatigue testing using X-ray microtomography was performed. in this respect, the following points have been investigated:

- The use of lamellar pattern to analyse strain concentration during a monotonic tensile test using the image correlation technique and the correlation of results using EBSD mapping. This has been personally carried out by the author.
- The qualitative analysis of the correlation between 3D crack propagation and microstructural features such as α colonies and β grain boundaries. This has been personally carried out by the author.
- The development of a texture analysis algorithm in order to segment α colonies automatically in 2D and subsequently in 3D so as to be able to automatically correlate the short crack path with the microstructure later on. The author is the main supervisor of this task.

IV.2. Material description and experimental setup

IV.2.1. Material

The investigated materials have concerned two types of Ti lamellar alloy, Ti-64 (Ti-6Al-4V) and Ti-6246 (Ti-6Al-2Sn-4Zr-6Mo). They exhibit similar microstructural characteristics except the latter one presents a smaller β grain size and a denser lamellar colony. This is a necessary condition to allow the control of the crack growth in small samples for the synchrotron X-ray microtomography experiment. On the other hand, image correlation following the optical in situ tensile test was carried out on the Ti-64 sample.

In both cases a fully lamellar microstructure was obtained after homogenisation in the β phase field (1 hour at 1055°C for Ti-64 and two hours at 935°C for Ti-6246) under argon to avoid surface oxidation and a subsequent cooling (at a rate of 2°C/min for Ti-64 and water quench for Ti-6246). An annealing process was later applied to Ti-6246 (at 875°C during one hour, then furnace cooling) in order to obtain a lamellar microstructure, coarse enough to be revealed in the X-ray microtomography experiment.

From the heat-treated plates tensile and fatigue samples were cut. in the case of the optical in situ tensile test, the Ti-64 samples were mechanically polished using OPS to obtain a mirror surface finish prior to etching. The microstructure was revealed by Kroll etching (2 ml HF, 4 ml HNO_3 and 100 ml H_2O) which resulted in a high contrast optical micrograph with dark α lamellae and bright remaining β phase in-between, as shown in Figure IV-1. The shape of the Ti-6246 samples used for the X-ray microtomography studies was similar except that a small triangular notch (2 μm wide, 100 μm long and 20 μm deep) was milled from the surface of the gauge centre using a FIB facility in order to grow a crack in a well defined position.

IV.2.2. Experimental setup

The setup used for the in situ fatigue experiment is similar to the one used in the previous chapter, except that a special fatigue test machine, also developed at INSA-Lyon, was mounted on the rotation stage of the ID19 beam line at ESRF.

In the case of the in situ tensile test, the samples were mounted on a Deben 2 kN microtester and placed under an optical microscope which was equipped with a cooled 12-bit CCD Zeiss Axiocam camera controlled by the Zeiss Axiovision software. During the test, great care was taken to keep the sample in focus in order to avoid pseudo-displacements generated by the image correlation algorithm. The natural contrast variation provided by the microstructure was used to map the surface displacements to sub-pixels resolutions. The algorithm

used for strain mapping was developed by LaVision, Göttingen, Germany. It uses FFT cross correlation to compare sub-regions.

As the result of the analysis of both the tomography data and the image correlation for strain concentration, areas of interests were identified for further EBSD studies. All EBSD scans were carried out using a Sirion field emission gun scanning electron microscope. The operating voltage used was 20 kV to optimise the quality of the diffraction patterns. The microscope was fitted with an HKL-EBSD system and the obtained data was analysed using the Channel 5 software package.

IV.3. Experimental results

IV.3.1. Correlation between lamellar microstructure and mechanical properties: 2D and 3D considerations

IV.3.1.1. Strain mapping during monotonic tensile test

In this part of the work, which is presented in Babout et al. [Babout et al. 2004b], it was decided to follow the strain localisation in an area corresponding to the black frame seen in Figure IV-1a. This area exhibits a number of interesting microstructural features, such as the presence of β and α layer triple joint and β grains which contain a network of α-colonies with different orientations. As it can be seen in Figure IV-1a, the microstructure is a coarse, fully lamellar one which is in agreement with the applied heat treatment. The average β grain size, α colony width, α layer and lamellae widths, and width of the inter-lamellar β phase (β-lath) are listed in Table IV-1.

Figure IV-1a also indicates the different zones (white rectangles) in which the average local strains were calculated during loading. in order to relate the strain localisations to the crystal orientations of the lamellar colonies, the analysis was completed by EBSD mapping. The EBSD mapping was performed at the initial stage on the same surface area presented in Figure IV-1a, and the corresponding Euler orientation map is shown in Figure IV-1b. The orientation map indicates the corresponding 3D orientation of the hexagonal unit cell for each colony. in order to simplify the analysis of the EBSD map, the bcc crystal system corresponding to the β phase (presents only about 5% vol. in Ti-64) was not identified. During the measurement, more than 70% of the map was indexed and the procedure of noise reduction was applied.

Table IV-1. Average sizes of features defining the lamellar microstructure of Ti-64 after heat treatment specified in Section IV.2.2. The table presents also the pixel size of the features used for image correlation, i.e. The α-lamellar and β-lath matrix. Table published in [Babout et al. 2004b]

Microstructural features	Size (μm)	Size (pixel) in image used for image correlation process
β primary grain	2000	
α-colony	400	
α-layer width	10	20-25
α-lamellar width	7	
β-lath thickness	0.8	3-5

The local strain histories along the loading direction and perpendicular to it, i.e. The y-axis and x-axis respectively, are presented in Figure IV-2a and b. For the different zones, the curves are plotted as functions of the corresponding overall strain in the region of interest (black rectangle). One can notice that the zones 2 to 4 present similar average longitudinal deformation rates which are lower than the one calculated in zone 1. On the other hand, the four zones present different Poisson contraction rates, as shown in Fig. 4b.

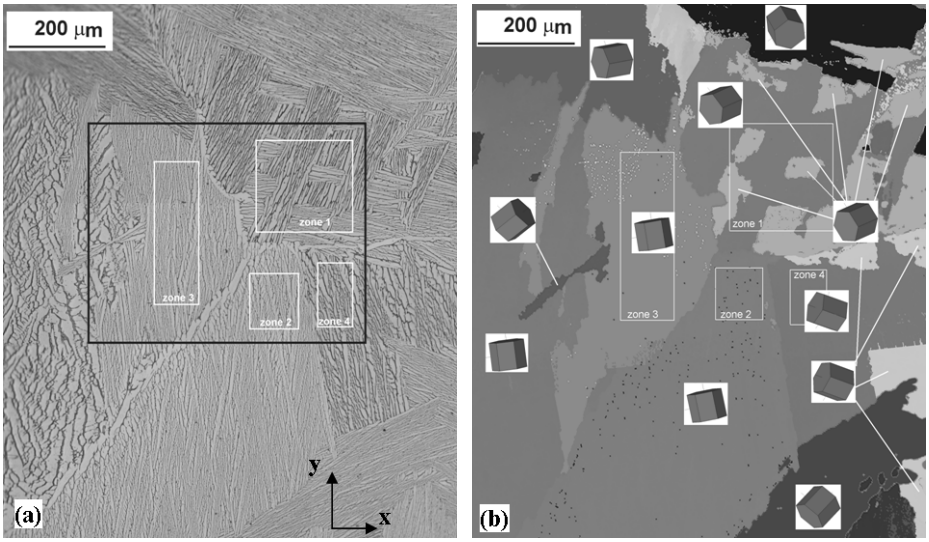

Figure IV-1. Ti-64 lamellar microstructure. (a) optical microscope image showing the ROI for image correlation (black rectangle) and the regions for average strain measurements (white rectangle). The straining direction is along the y axis. (b) EBSD map showing crystallographic orientation of hcp crystal system of α-phase. Figures published in [Babout et al. 2004b]

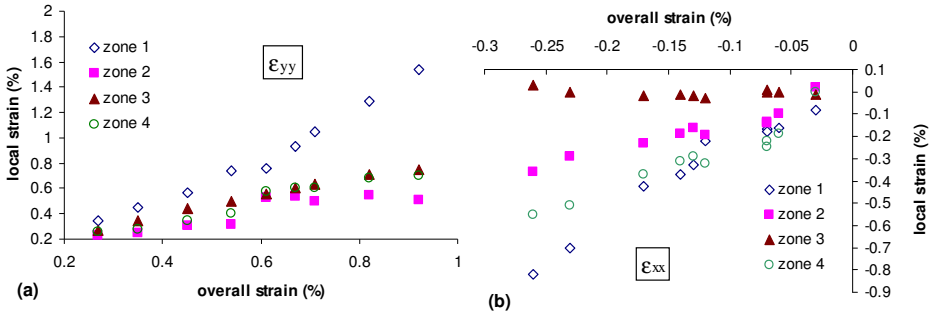

Figure IV-2. Evolution of the local strain components in different zones of the ROI as a function of the average overall strain component. (a) ε_{yy}. (b) ε_{xx}. Figures published in [Babout et al. 2004b]

In the case of the ε_{yy} strain component, it was found that the zone 1 displays a higher deformation scatter than the other three zones. This trend is shown in Figure IV-3, which presents a strain map calculated after 5% deformation of the tensile sample. The map is superimposed on the corresponding lamellar microstructure recorded at the initial stage. One can notice that the strain is relatively homogeneous in the zones 2 to 4, compared to the zone 1 where the strain intensity is much higher and spread in different locations. Moreover, in the grain where zone 1 was selected, the highest strain seems to be located in a variant where the α-lamellar structure is closely oriented along the direction parallel to the tensile axis rather than in the colonies with their orientation perpendicular to the tensile axis. From the strain map, one can also observe that the α-layer at the β-grain boundary do not exhibit any major strain localisation.

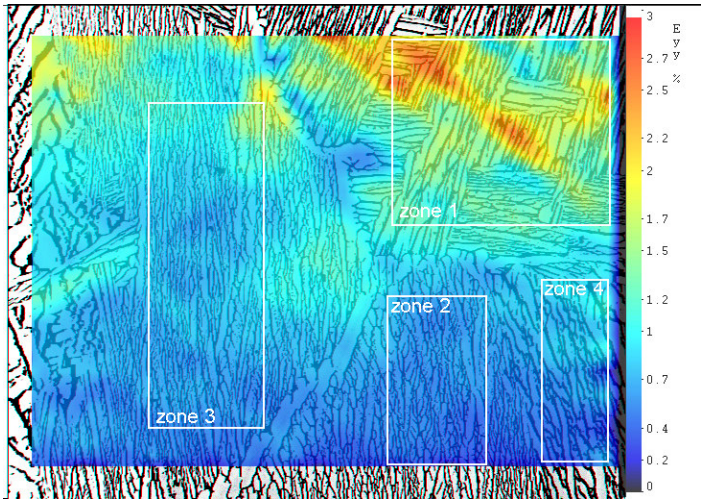

Figure IV-3. ε_{yy} strain map obtained by the image correlation technique. The tensile direction is vertical. Figure published in [Babout et al. 2004b]

From the previous results, the lamellar orientation seems to play a role in the localisation of strain within a grain. However, this effect cannot be regarded as a major influence to explain the difference between the different grains as their orientation is similar in zones 2,3 and 4 and parallel to the y-axis. On the other hand, the effect of crystal orientation of lamellar colonies can be related to the strain localisations. Indeed, one can tell from the comparison between the EBSD and strain maps (Figure IV-1b and Figure IV-3 respectively) that the colonies corresponding to the zones 2 and 3 have their c-axis orientated relatively parallel to the tensile axis. This is in agreement with the low strain since the pyramidal slip required in this case has a critical resolved shear stress significantly higher than the prismatic or basal slip (both have only the "a" component) [Savage et al. 2001; Zaefferer 2003]. However, in the case of zone 1, the crystallographic orientation is more suitable for higher strain concentration as slip bends may develop more easily in the basal plane, parallel to the prismatic direction. This argument was confirmed by higher magnification optical images which have shown a concentration of the slip bend in this colony higher than the one in the zones 2 and 3. The relatively low strain concentration in the α-layer predicts a transgranular dimple fracture mode in the coarse lamellar microstructure instead of the intergranular dimple fracture mode, as expected in the martensitic lamellar microstructure [Lutjering 1998].

This 2D study could be transposed to 3D during an in situ tensile test coupled with X-ray microtomography. However, this will imply that the image correlation technique is adapted to 3D, which has not been the case hitherto because of computational limitations. Moreover, the presence of two crystallographic phases makes the use of DCT problematic since the technique is, to this day, designed for polycrystalline materials exhibiting low intra-grain orientation spread (i.e. lower than 1°) [King et al. 2010]. However, a different type of study which is complementary to that one and can be conducted in 3D concerns the development of fatigue crack, since it is known, in 2D, to be strongly influenced by the microstructure, especially for short cracks.

IV.3.1.2. Crack propagation during in situ fatigue test coupled with X-ray microtomography

The 3D images shown in Figure IV-4 present a comparison between the initial stage and one of two fatigued stages of a notched (α+β) Ti-6246 alloy sample. One can see that the lamellar microstructure can be satisfyingly observed, with a primary grain boundary (β-grain boundary in Figure IV-4) separating two grains clearly visualised. Some α lamellar colonies situated within β grain are also unmistakably distinguishable. a closer look shows that white fringes are situated between the lamellae and along the β grain boundary and correspond to the phase contrast (see section I.2.2.3). Even though only three scans have

been acquired for the sequential experiment presented in [Babout et al. 2006c], their comparison reveals useful information. One can see in Figure IV-4b that crack1 has propagated fairly linearly within a colony between points A and B, then deviated at a boundary with a neighbouring colony. The computation of an oblique slice in the crack plane also reveals more interesting features of the crack development in interaction with the microstructure: undulation of the crack front (between points B and C in Figure IV-5a) and apparent crack branches propagating between the lamellae (points 1 to 4 in Figure IV-5a). This phenomenon has been also observed in a more recent and more detailed study of the fatigue short crack interaction with the microstructure [Birosca et al. 2010]. The 3D rendering of this crack is displayed in Figure IV-5b with isosurfaces of the notch and the β grain boundary. The figure also shows the isosurface of the intense phase contrast fringes generated by the unresolved cracks (PCC). The different features have been segmented using an image processing method known as region growing. It is worth noticing that the difficult segmentation of the β grain boundary has been facilitated once again by the white fringes which contain a region growing within the boundary. The presence of the β grain boundary is revealed by the growth of α-layer along it. The observations have not revealed a strong influence of the β grain boundary because of the localisation of the notch that crosses the one of interest. However, Birosca et al. [Birosca et al. 2010] have also shown that undulation and deflection of the crack occurred when it reached the β grain boundary. Moreover, their observation concluded that when the misorientation between two adjacent β grains is large, a crack which enters a new grain is diverted and usually stopped, then a secondary crack forms, leading to a crack bifurcation.

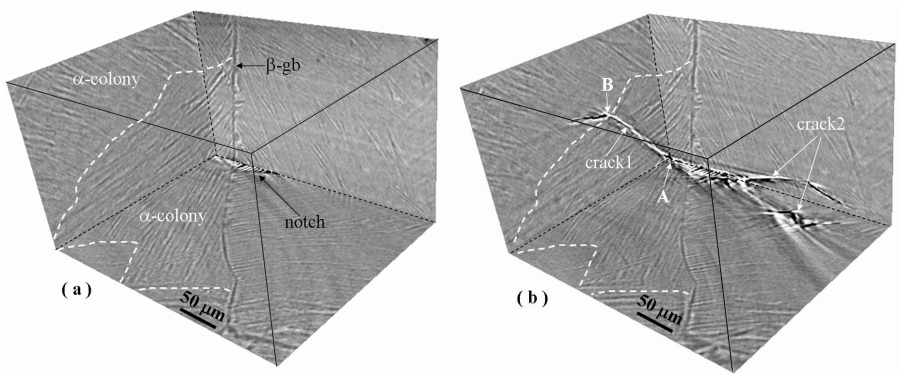

Figure IV-4. 3D reconstructed images in 3 principal directions of Ti-6246 alloy sample (a) virgin state, (b) after 29K cycles. Figures published in [Babout et al. 2006c]

The previous observations have confirmed a notion that β grain boundary and α lamellar colonies alike have a direct impact on the crack path, especially for short fatigue cracks. However, the degree of deflection that is introduced when a boundary is reached has only been established in a qualitative way so far. A more precise estimation would necessitate the segmentation of the features that are correlated to the crack deflection, i.e. The crack itself, the β grain boundary and the α lamellar colonies. in the case of the latter feature, the directionality of the lamellae could also be estimated and correlated to the deflection, even if a more sound parameter was the lattice orientation extracted from DCT. However, this 3D estimation is still impossible for a two-phase material and only successive EBSD maps following a grinding step or FIB polishing have been used [Groeber et al. 2006; Birosca et al. 2010] to build 3D orientation maps of such materials. The segmentation of the above mentioned features is therefore a complementary analysis that is worth carrying out. The features have to be treated separately, hence the next section presents the first methodology that has been used to segment α-lamellar colonies constituting the most challenging microstructural feature, as it can be guessed from Figure IV-4.

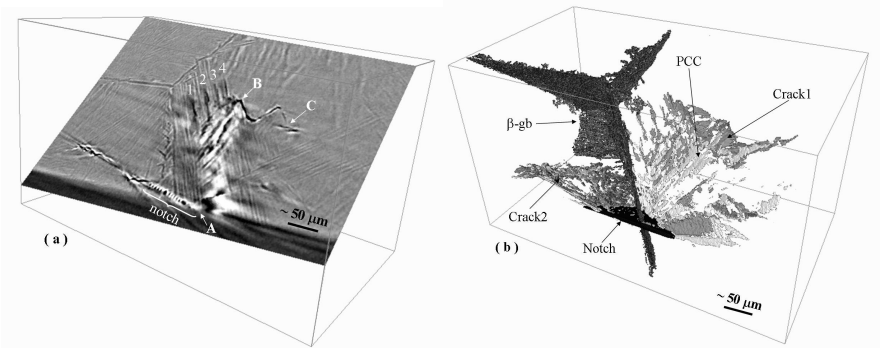

Figure IV-5. (a) oblique slice- 29K cycles.(b) 3D rendering of crack (grey), grain boundary (dark grey) and notch (black). The isosurface of phase contrast corresponding to the sub-resolution crack (PCC) is also displayed (light grey). Figures published in [Babout et al. 2006c]

IV.3.2. 2D segmentation of lamellar colonies using texture-based method: ideas and limitations

From an image processing point of view, the task to segment the different lamellar colonies is not conventional because an image of lamellar microstructure is a good example of a textured one. Indeed, it seems composed of repeated elements (the lamellae) with different interspacing and different orientations (a group of lamellae with the same orientation and relatively constant interspacing forms a colony). Moreover, classical segmentation methods based on the intensity histogram cannot be used to segment

and separate the different colonies. Even if the pattern in each α-lamellar colony does not repeat perfectly, image texture segmentation algorithms seem the most promising approach for this segmentation task.

Texture is a commonly used feature in the analysis and interpretation of images. It is characterised by a set of local statistical properties of pixel intensities. It analyses variations in the image, taking into account such properties as: smoothness, coarseness and regularity of patterns. Traditionally, texture features have been calculated using a variety of statistical, structural and spectral techniques, including co-occurrence matrices, spectral measures using filters, such as the Gabor filter [Teuner et al. 1995; Pichler et al. 1996], the fractal dimension and multi-resolution technique, such as wavelets [Mallat 1989]. The latter has been successfully used in image processing with the recent emergence of application to texture classification. The main advantages of the wavelet frames representation are that they focus on scale and orientation texture features and they decompose the image into orthogonal components.

IV.3.2.1. Methodology

The method that has been applied is presented in [Babout et al. 2009] and it considers different sets of images for the texture segmentation: the original image and the so-called detail images after DWT decomposition of the original one. The usefulness of wavelets has been shown in texture analysis, possibly due to their finite duration, which provides both frequency and spatial locality. The hierarchical wavelet transform uses a family of wavelet functions and its associated scaling functions to decompose the original image/signal into different sub-bands [Mallat 1989]. An example of such decomposition at level 1 is shown in Figure IV-6. The decomposition has been obtained using MaZda, a texture analysis software [Strzelecki et al. 2006]. The figure shows the so-called Approximation Image (*A1*; top-left), the Vertical Detail Image (*V1*; bottom-left), the Horizontal Detail Image (*H1*; top-right) and the Diagonal Detail Image (*D1*; bottom-right). The Detail images have been binarised and inverted to enhance the contrast between colonies of different directionality. These images are obtained from the decomposition of the original image using a combination of low-pass and high-pass bands based on Haar wavelet [Dettori and Semler 2007], along both x- and y- directions of the input. For instance, the image *H1* is obtained from the original one by consecutively convolving it with the low-pass filter along x-direction and the high-pass filter along y-direction. During decomposition, approximation and detail images are down-sampled, resulting in images four times smaller than the original one. in order to create decomposed images of the same size as the original one, the input image is then up-sampled prior to wavelet decomposition. The Approximation Image at level 1 can as well be decomposed into four sub-images, and the process can be repeated recursively to obtain a filtered image

of size 1 (pixel). The wavelet decomposition is then a multi-resolution technique since at each level of decomposition the spatial resolution is decreased by a factor of 2.

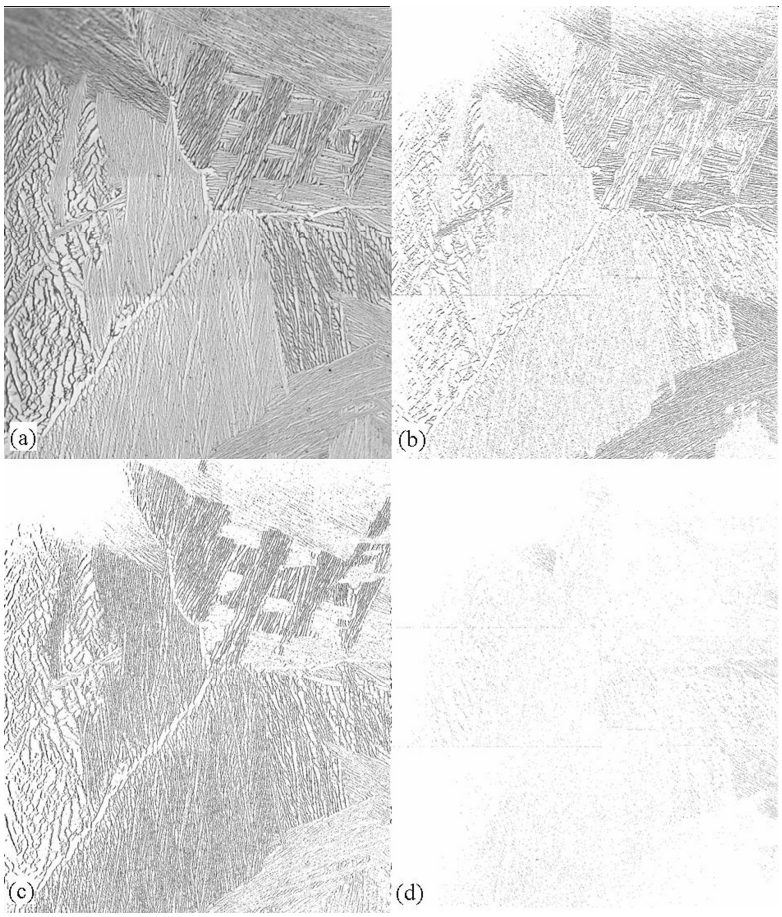

Figure IV-6. Wavelet transforms applied to image shown in Figure IV-1a. (a) Approximation image, (b), Horizontal Detail image, (c), Vertical Detail image and (d) Diagonal Detail image. Figures published in [Babout et al. 2009]

One can see from Figure IV-6b and Figure IV-6c that *V1* and *H1* exhibit a higher contrast than that of the original image for colonies, which tend to be perpendicular and parallel to x-direction, respectively. On the other hand, *D1* does not exhibit such a trend with few areas oriented close to 45°, resulting in a very low contrasted image (Figure IV-6d). Therefore, *H1* and *V1* are used preferentially for the following step of the texture segmentation method. It consists in generating a new image A*1* for which each pixel is classified as follows:

$$p_{A1,xy} = \begin{cases} 0 & I(V1_{xy}) > I(H1_{xy}) \\ & + \delta \min(I(V1_{xy}), I(H1_{xy})), \\ 127 & I(V1_{xy}) < I(H1_{xy}) \\ & + \delta \min(I(V1_{xy}), I(H1_{xy})), \\ 255 & \left| \frac{I(V1_{xy}) - I(H1_{xy})}{\min(I(V1_{xy}), I(H1_{xy}))} \right| \leq \delta \end{cases} \quad \textbf{Eq. IV-1}$$

where $p_{A1,xy}$ is the grey level of the pixel at coordinate *(x,y)*, δ an empirical dimensionless factor smaller than 0.1, $I(V1_{xy})$ and $I(H1_{xy})$ are the local mean grey level intensities, as described by the following general expression:

$$I(A_{xy}) = \frac{1}{(2r+1)^2} \sum_{i=x-r}^{x+r} \sum_{j=y-r}^{y+r} p_A(i,j) \quad \textbf{Eq. IV-2}$$

where a is a given analysed image, *2r + 1* is the size of the analysing window and $p_A(i,j)$ is the grey level of the pixel at coordinate *(i,j)*. The third classifier in Eq. IV-1 ($p_{A1,xy} = 255$) corresponds to the situation where there is no preferential directionality (either vertical or horizontal) in the current position. in practice, δ is selected after the comparison of the data *in* ROIs where both *H1* and *V1* present a similar grey level intensity.

The second step of the texture segmentation is based on the local analysis of the grey level variance parameter in the original image. The variance σ^2 is one of texture measures that can be used to discriminate among different classes of texture pattern. This parameter tells how spread out the distribution of grey level is. For a window (also called ROI) of size *NxM* centred at a pixel position *(x, y)* the variance calculated for an image a is given by:

$$\sigma^2 \equiv \sigma^2(A_{xy}) = \sum_{i=1}^{N_g} (i - I(A_{xy}))^2 h_A(i) \quad \textbf{Eq. IV-3}$$

where N_g denotes the number of intensity levels (i.e. 256 in the present case), $h(i)$ is the normalised histogram vector (i.e. histogram whose entries are divided by the total number of pixels in ROI) and $I(A_{xy})$ is the mean intensity defined by Eq. IV-2.

A new set of classifiers is defined depending on the value of the variance. The range of variance value of the image is separated into 3 regions delimited by:

$$P_1 = C_1 + \varepsilon$$
$$P_2 = C_2 - \varepsilon$$

Eq. IV-4

where C_1 and C_2 are the minimum and maximum variance of all the windows extracted from the input image, respectively, and ε is the scale factor defined by:

$$\varepsilon = (C_2 - C_1) \times \delta'$$

Eq. IV-5

where δ' is an empirical factor with a value ranging between 0.1 and 0.5. a new image *A2* is created, based on the following class of pixels, depending on their variance value (low, middle and high):

$$p_{A2,xy} = \begin{cases} 0 & \sigma^2 < P_1, \\ 127 & \sigma^2 < P_2 \wedge \sigma^2 \geq P_1, \\ 255 & \sigma^2 > P_2 \end{cases}$$

Eq. IV-6

Finally, the pixels of the final image A_{fs} are classified into 7 different classes $cl_{1\to7}$ based on their corresponding value in *A1* and *A2*:

$$cl_1 = \{(x,y) \in Z^2 ; p_{A1,xy} = 0 \wedge p_{A2,xy} = 0\}$$
$$cl_2 = \{(x,y) \in Z^2 ; p_{A1,xy} = 0 \wedge p_{A2,xy} = 127\}$$
$$cl_3 = \{(x,y) \in Z^2 ; p_{A1,xy} = 0 \wedge p_{A2,xy} = 255\}$$
$$cl_4 = \{(x,y) \in Z^2 ; p_{A1,xy} = 127 \wedge p_{A2,xy} = 0\}$$
$$cl_5 = \{(x,y) \in Z^2 ; p_{A1,xy} = 127 \wedge p_{A2,xy} = 127\}$$
$$cl_6 = \{(x,y) \in Z^2 ; p_{A1,xy} = 127 \wedge p_{A2,xy} = 255\}$$
$$cl_7 = \{(x,y) \in Z^2 ; p_{Acl1}(x,y) = 255\}$$

Eq. IV-7

The definition of the class 7 is not taking into account the variance since the areas around the pixels of this class do not exhibit directionality, hence variation in the average intensity.

The values assigned to pixels from classes 1 to 7 were set to 0, 75, 125, 150, 175, 200 and 255, respectively. It is worth mentioning that the method described above was intended to assess whether the wavelet-based texture method is a possible candidate to segment the microstructure of interest. The following scenario was then devised: testing the approach on a 2D model "little-noise" image of lamellar microstructure where good texture segmentation is expected, and on a "real" 2D image of the same microstructure obtained with X-ray microtomography to analyse the possible limitations of the method and foresee new strategies.

IV.3.2.2. Microscope images

Figure IV-7 displays the result of the above procedure tested on the image presented in Figure IV-1. Particularly, it shows the pixel classification after the wavelet transform (Figure IV-7b), and the final segmented image (Figure IV-7c). The features (mean intensity in decomposed images and variance) were calculated for each pixel of the original image using a local window of size 25x25 centred on the corresponding pixel. The window size of 25x25 was found a good compromise between the reliability of the calculated texture features and the accuracy of boundary localisation in texture segmentation. Moreover, the choice of δ and δ' set to 0.1 and 0.2 (Eq. IV-1 and Eq. IV-5) was found to provide the best texture segmentation. The corresponding variance boundaries, P1 and P2 defined in Eq. IV-4, were set to 700 and 2820, based on the minimum and maximum variance of all the windows extracted from the image, i.e. 0 and 3520, respectively.

One can notice that the first classification based on the local intensity of the wavelet transform decomposition separates relatively well the colonies with nearly-horizontal and vertical orientations. Only a few boundaries between the areas with strong horizontal and vertical details present no preferential directionality (very thin white layers and spots in Figure IV-7b). The final segmentation also compares relatively well with an EBSD map of the same region (Figure IV-7d), showing the effect of variance classification to separate the colonies of the same wavelet-based classification. It is worth noticing that even if 7 classes of feature properties are defined in Eq. IV-7; the colonies are mainly classified as cl_1, cl_2, cl_4 and cl_5, as shown in Figure IV-7c. The results show particularly good boundary discrimination between colonies 7 and 8, where the mean variances are different and the standard deviation is low

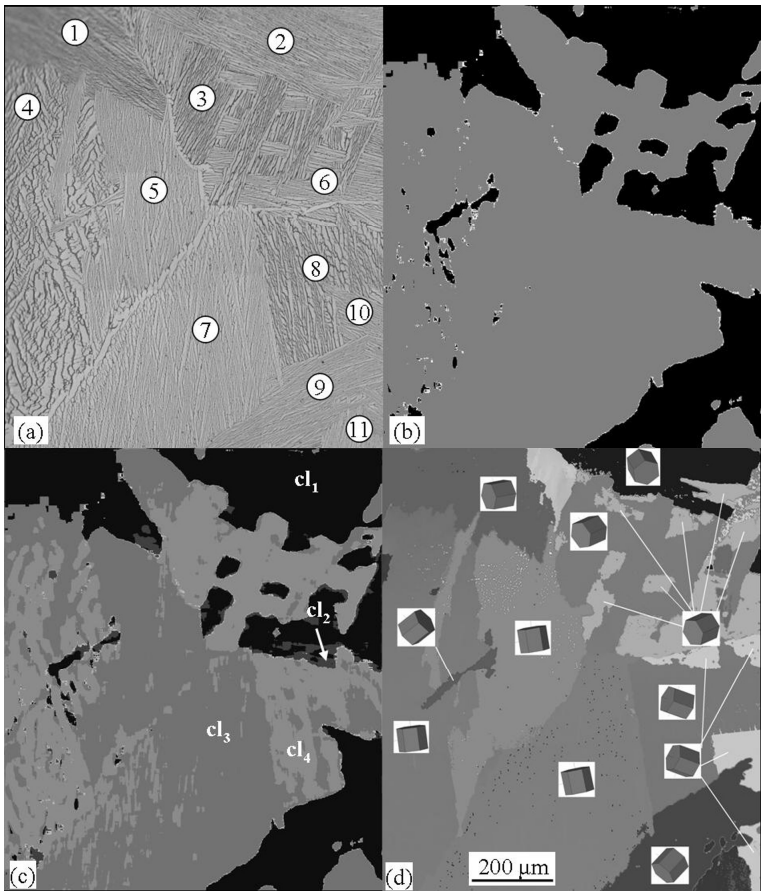

Figure IV-7. (a)Image from optical microscope and corresponding segmented results: (b) segmentation after wavelet classification (c) final segmentation (d) EBSD map of the same region as (a) showing the different hcp crystal lattice orientation of the colonies. Figures published in [Babout et al. 2009]

(small fluctuation of the variance indicating regularity of the lamellar pattern in these colonies). However, the texture segmentation fails to separate features where the mean variance is of a similar order of magnitude, for instance, between colonies 5 and 7 or 9 and 10. in the former case, the method also shows its current limitation to detect the grain boundary present between these two colonies. Finally, the variance shows some limitation to accurately discriminate the boundary of the colonies where an interspacing between lamellae is irregular and of similar size as the analyzing window, illustrated by a large fluctuation of the variance value, such as in zone 4.

IV.3.2.3. X-ray microtomography image

The method presented in the previous section concerned the case of the best scenario where features of the image with different orientations and different grey level intensities were clearly distinguishable. The type of image, presented in this section, is of a greater importance since it is directly linked to the main goal of correlating, in 3D using X-ray microtomography, the propagation of a crack with the microstructure of a lamellar titanium alloy. However, such images contain a higher level of noise than that in the previous case, reducing the perception of lamellar colonies. Not only the noise, but also the weak phase contrast resulting from unresolved lamellae at a given spatial resolution of the system (in the present case, 0.7 μm) may also locally weaken the colony segmentation. Therefore, before considering the 3D case, the method has been applied to 2D reconstructed images of the same material, i.e. Ti-64 sample, observed with an optical microscope.

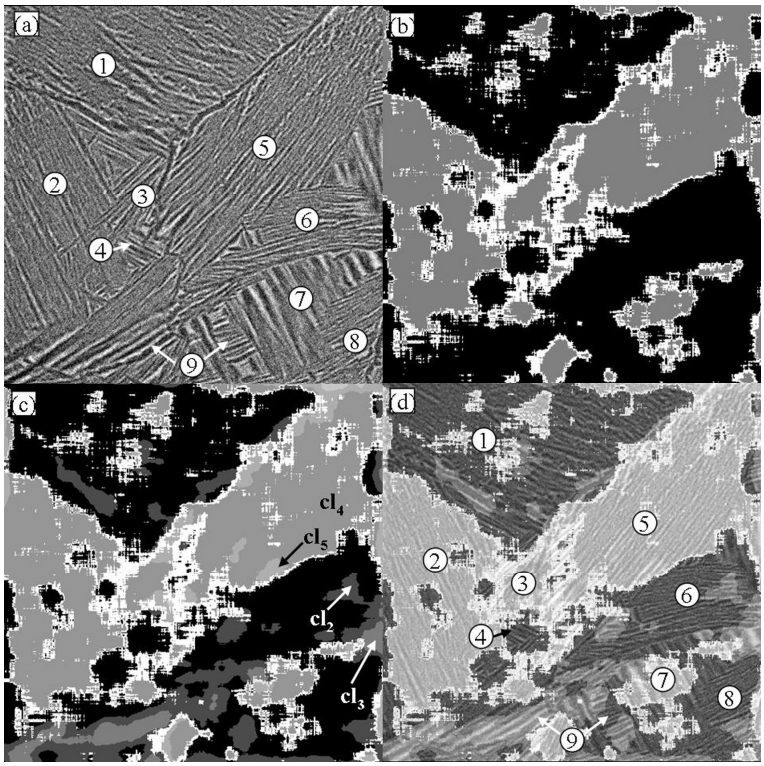

Figure IV-8. (a) image from X-ray microtomography and corresponding segmented results (b) segmentation after wavelet classification (c) final segmentation (d) superposition of (a) and (c). Figures published in [Babout et al. 2009]

Figure IV-8 displays the result of the texture segmentation (500x500 pixels). The features (intensity in decomposed images and variance) at a pixel (x,y) were calculated within a local window 32x32 pixels in size centred on it. This window was set larger than the window in the previous example because of a higher level of noise. Moreover, δ and δ' were set to 0.1 and 0.4, the latter showing, from our point of view, the best texture segmentation. The pixels in this image present a variance between 840 and 4790, which result in variance boundaries P1 and P2 equal to 2620 and 3015, respectively.

In general, the result of the texture segmentation shown in Figure IV-8c, superimposed on the original image as shown in Figure IV-8d, is less satisfying than in the previous case, i.e. The image from the optical microscope. However, due to the complexity of the image, the results are encouraging. Indeed, one can notice than some boundary discriminations between colonies are relatively accurate, such as the ones between colonies 1 and 2, 1 and 5 or 5 and 6, which, in these cases, are mainly due to relatively good wavelet decomposition (see Figure IV-8b). Some small regions, such as zones 3 and 4, are also detected. However, the decomposition fails, like in the previous example, to delimitate colonies of the same orientation separated by a grain boundary, such as colony 1 and the one localised above colony 3 in Figure IV-8a. As expected, the areas which correspond to the third class from wavelet decomposition (Eq. IV-1), i.e. without preferential directionality (white colour), are formed at boundaries between the colonies with strong misorientation. Two large white areas can also be observed between zones 2 and 3, 3 and 5. While the former area results from the misorientation of the colonies within the same grain, the latter one corresponds to a portion of zone 5, surprisingly. The possible reason which could explain the presence of no preferential directionality in this zone is the average orientation of the lamellae at 45º which may result, after wavelet decomposition, in the nearly equal local intensity in the corresponding Horizontal and Vertical Detail images. Finally, the boundary discrimination is not satisfying in the zones where the lamellar directionality is fading, as in zone 7. However, Figure IV-9 shows that the lamellae are better distinguishable and regularly spaced in another orthogonal plane. Therefore, for this colony, the boundary discrimination may be more accurate in that plane.

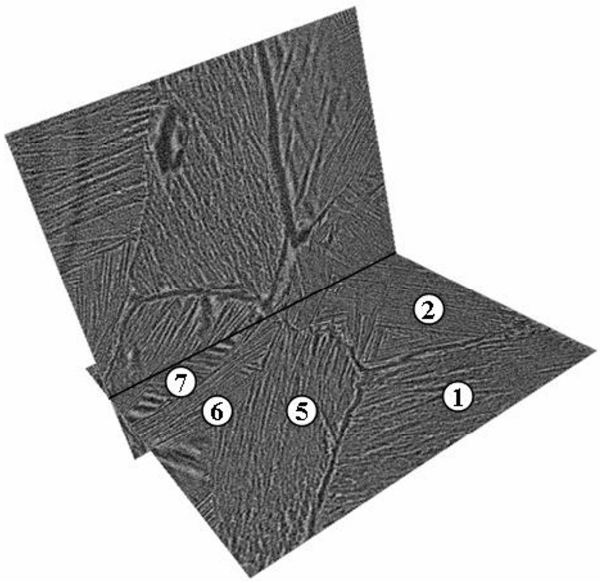

Figure IV-9. 3D view showing the reconstructed image of Fig. 5a with another orthogonal plane crossing the colonies 2 and 5. Figure published in [Babout et al. 2009]

IV.4. Conclusion and future work

This chapter has presented the unique results of X-ray microtomography investigation of short fatigue crack propagation in lamellar titanium alloys. The tomography data have provided a chronological description of the crack propagation in three dimensions. Additionally, it has confirmed the role of prior β grain boundaries and identified the importance of the morphology and crystallographic orientation of the α lamellae, as this has also been shown using the image correlation during a simple monotonic tensile test. For instance, the qualitative results have shown that cracks are deflected by the β grain boundaries, usually stopped at these boundaries with secondary cracks propagating farther and resulting in branching. in addition, the lamellar grain orientation and morphology cause a second-order crack front undulation with the tendency for large misorientations between the lamellae preferably orientated for prismatic ‹a› slip or pyramidal ‹c+a› slip deflecting the crack path. The crystallographic influences have been carried out using EBSD on a set of polished surfaces that have been ground at different depths from the notched surface. However, the results are semi-quantitative since it is practically impossible to characterise its interaction with these microstructural features along the full depth of the crack. Therefore, a complementary study that aims at segmenting the different features and correlate them together has already been embarked upon.

This section has presented a preliminary approach based on the wavelet-based texture segmentation method to segment lamellar colonies in a (α+β) titanium alloy. a comparison of segmentation results of images of the same titanium-based microstructure from an optical microscope and X-ray microtomography have shown that the method, which does not take into account any prior knowledge of the texture pattern, works relatively well when the lamellae are clearly distinguishable and the pattern in colonies is regular. However, the present method does not detect those grain boundaries which may be of importance when they separate two colonies of the same orientation. This is a crucial point in the future study of correlation between the crack path and the microstructure since grain boundaries in lamellar titanium alloys deflect cracks. a possible method would be to specify a special class of grey level features which discriminate only those grain boundaries among all the patterns which compose the lamellar image. Moreover, the choice of the boundaries for the variance classification may also be insufficient to adequately discriminate connected colonies of the same orientation. The present method was simply considering three ranges of variance value, based on the minimum and the maximum variance of the image, while another approach could consider a study of the variance histogram to select the ranges.

Other approaches such as a gradient-based approach [Vanderesse et al. 2008] and a ridgelet transform [Donoho 2001] are currently in the implementation phase. The gradient-based approach has already been tested on lamellar titanium alloys but the method has shown limitations in defining precisely the boundaries between colonies, and even more between β grain boundaries. The current method expands the one presented in [Vanderesse et al. 2008] by including pattern recognition concepts such as clusterisation and classification based on a training data set. The ridgelet transform is a recent multi-resolution analysis tool based on the wavelet transform which captures the structural information of an image based on multiple radial directions in the frequency domain [Donoho 2001]. The image decomposition considers more than three detail images as for DWT (vertical, horizontal and diagonal), and may therefore be of a greater interest to issue the discrimination of adjacent lamellar colonies with opposite orientations.

V. FINAL CONCLUSIONS AND FUTURE WORK

This manuscript sums up the research work of the author produced in the past seven years in the field of materials science, with a special focus on the study of three different degradation processes in engineering materials using X-ray (micro)tomography. His personal contribution has covered most of the necessary steps of a materials science study, e.g. sample preparations, setup and conduction of in situ experiments, data analysis and development of prediction models. He has also developed algorithms for 3D image processing and analysis of X-ray (micro)tomography images. Naturally, the unique results presented in this work wouldn't have been possible without strong collaborations with eminent colleagues from the MMSC (the School of Materials – The University of Manchester), i.e. Prof. P.J. Withers, Dr T.J. Marrow, Dr P.M. Mummery, and from the CED (Technical University of Łódź), i.e. Dr M. Janaszewski and Mr. Ł. Jopek. Although the content of the manuscript is mainly materials science-oriented, some aspects of computer science, especially those concerning image processing and analysis, have been combined so as to show that both fields of science need each other, especially with the 3D characteristics of the data. Indeed, materials science needs the information from the images to be extracted. Likewise, computer science, and in our case image processing, needs original data to test new algorithms and methodology. a great deal of effort has been put in the writing of this manuscript to make it readily comprehensible for both materials scientists and computer scientists who are willing to acquire more information about the other field. The author does hope that he has achieved this goal.

From the three different studies presented in this manuscript it seems evident that there is no single universal image processing solution that can extract features from any microstructural image, the image being either 2D or 3D. in most of the cases there is one solution to one problem, and it strongly depends on the morphological characteristics of the feature. For example, in the case of a porosity network in nuclear graphite presented in Chapter II, it was important to define a strategy that would separate isolated and continuous porosities since they influence mechanical and physical properties of the material in different ways. The author has therefore developed a geometrical approach called the intersected branch method that allows one to perform such porosity classification. The incorporation of these data into the porosity model based on Euler equations compared relatively well with the experimental data of thermal conductivity obtained for the samples with different weight loss induced by thermal oxidation.

The approach presented in Chapter III was completely different. in this case, the study was aimed at the analysis of the interaction of an intergranular stress corrosion induced crack with the microstructure of polycrystalline stainless steel.

Indeed, the visual inspection of the 3D data revealed the presence of the so-called bridge ligaments along the crack path that cannot be extracted using standard methods, such as histogram-based segmentation since these features do not correspond to a subset of the 3D space. Two methods, originally developed for medical applications, have been tested: voxel coding and hole closing. The latter has shown its usefulness in solving a challenging problem of segmenting bridges equivalent to the holes in the 3D object that corresponds to the crack. The algorithm has also been extended to extract the volumetric area of a bridge defined by the thickness of the surrounding crack in order to further define the crack opening displacement.

In the previous studies, the features of interest have been analysed, or extracted, after the classical histogram-based segmentation of the porosity network or the crack. The problem with the lamellar titanium alloy presented in Chapter IV is that α colonies are good examples of textured objects and the classical segmentation method is useless. The in-situ fatigue experiment coupled with X-ray microtomography carried out under the supervision of the author on this type of materials has revealed the importance of such a feature in the propagation of short cracks. Among these three studies, this is the one that presents the most difficult challenges because of the complexity of the microstructure. The method tested so far, i.e. discrete wavelet transform, has shown some promising results in the case of optical microscope images, but seems less satisfactory in the case of X-ray microtomography images, mainly due to the higher level of noise present in the volume. It is worth mentioning that this investigation is the latest of the three studies proposed and it will take a larger part of the author's research efforts in the future, as presented in more details below.

Drawing on the above conclusion, some prospects of work can be outlined that correspond to the continuity of these projects, but also new avenues are opened up related to using image processing and analysis to assist the quantification of phenomena in materials science.

1. Morphological and crystallographic analysis of bridges: Bridges are represented by objects of 1-voxel thickness that can be further analysed in terms of shape using morphological descriptors, but also in terms of size and orientation. This set of information can be correlated with crystallographic properties of the bridges with respect to the grain boundaries that have failed during the IGSCC due to the emergence of the DCT in the past 5 years. Therefore, it will be possible to determine in the future whether the presence of the bridges is mainly governed by the degree of crystallographic misorientation of adjacent grains, or rather influenced by the spatial orientation of the grain in relation to the crack path (as one can assume that the grain boundary that is oriented perpendicularly to the loading direction is less prone to cracking). Most of this work started during

the recent six-month training period of the author at the MMSC within the DENIDIA project and should end within the next two years. However, preliminary results have been already presented in two recent articles. The first one has been published in Decembre 2010 [Ludwig et al. 2010]. It presents the first results of crystallographic properties of the bridges detected along the main crack path that led to the failure of the specimen investigated. The second one, which considers the same set of tomography data and has focused on the geometrical characteristics of the bridges during failure process, has been submitted by the author in Octobre 2010 [Babout et al. 2010b].

2. Correlation between short fatigue crack and microstructural features of a lamellar titanium alloy: the work that has been presented in this manuscript is just the visible part of the iceberg. There is still much to be done in the field of data characterisation, especially in terms of feature segmentation which concerns not only the α-colonies, but also the β grain boundaries as well as the crack itself. As mentioned earlier, the greatest challenge resides in the segmentation of the α-colonies. Some new methods are currently in the implementation phase and this work is mainly carried out by Mr. Ł. Jopek within the framework of his PhD that he embarked upon in September 2008. It is worth mentioning that the author has submitted in August 2010 a research proposal which has been qualified for funding by the Polish Ministry of Science and Higher Education (Section N519 – computer methods in science). It aims at the segmentation of each feature listed above from different scans (the first scan used for microstructural features, other scans for the crack propagation) and combine them back using the image registration method. This will allow one to extract characteristic curvilinear patterns of the feature that represent the crack, such as the one where two crack branches are formed (branch segments), where the crack strongly changes its propagation direction (deflection segment) and possible undulation of the crack tip (sinusoidal-like segment).

3. New avenues of research: the recent stay of the author at the MMSC was also of a great benefit to the new projects that take advantage of the X-ray tomography technique. These involve characterisation of other types of materials in different processes, but are also challenging from the image processing point of view. This concerns the inspection of the new solid state welding of aluminium alloy sheets (e.g. USW and FSSW) in collaboration with Prof. P.B. Prangnell, but also the deformation process of auxetic polyurethane foam (collaboration with Prof. P.J. Withers and Dr S.M. McDonald). The preliminary results of both studies have been presented in [Babout et al. 2010a]. For instance, it would be very interesting to characterise the shape of the non-welded areas in USW for different energy inputs. This study will be relatively similar to the one

corresponding to the classification of bridge shapes in IGSCC in stainless steel. Indeed, these defects are located at the weld interface, and thus are very thin, but the area can be relatively large, compared to the spatial resolution of the X-ray tomography system in use. Regarding the deformation process in polyurethane foam, the research is also very challenging and worth consideration, both from the materials science and image processing points of view. The auxetic property of these foams is relatively new in the field of materials science and very little is known about how to understand and predict the deformation process. Moreover, the microstructure of this open cell material is a typical example of the application of a thinning algorithm and the graph theory to analyse the joints and rubs as nodes and segments. This will give rise to more possibilities in terms of understanding and predicting how the deformation occurs at the level of joints, but also at the level of the loops defined by connected joints.

BIBLIOGRAPHY

[1] ABRAMOFF, M.D., MAGALHAES, P.J. and RAM, S.J., 2004. *Image processing with image J.* Biophotonics International, 11: p. 36-41.

[2] AKTOUF, Z., BERTRAND, G. and PERROTON, L., 2002. a *three-dimensional holes closing algorithm.* Pattern Recognition Letters, 23: p. 523-531.

[3] APPLETON, B. and TALBOT, H., 2006. *Globally minimal surfaces by continuous maximal flows.* IEEE Transactions on Pattern Analysis and Machine Intelligence, 28: p. 106-118.

[4] ASHBY, M., 2005. *Materials selection in mechanical design (third edition)*. Oxford: Butterworth-Heinemann. 624 p.

[5] ATTIX, F.H.R. and ROESCH, W.C., 1968. *Radiation dosimetry. Volume I: Fundamentals*. New York: Academic Press.

[6] BABOUT, L., 2006. a *novel computational approach to detect isolated and continuous phase in structured materials*. In: *Proceedings of 2nd International Conference of Young Scientists "Perspective Technologies and Methods in MEMS Design" – MEMSTECH 2006*. Lviv-Polyana, Ukraine: IEEE,Piscataway, NJ, USA. p. 39-42.

[7] BABOUT, L., BRECHET, Y., MAIRE, E. and FOUGERES, R., 2004a. *On the competition between particle fracture and particle decohesion in metal matrix composites.* Acta Materialia, 52: p. 4517-4525.

[8] BABOUT, L., DA FONSECA, J.Q. and PREUSS, M., 2004b. *Local strain imaging during mechanical loading of lamellar microstructures in titanium based alloys*. In: *Advances in Experimental Mechanics*. Applied Mechanics and Materials. 159-164 p.

[9] BABOUT, L. and JANASZEWSKI, M., 2009. *Analysis of bridge ligaments in 3D volumetric images using discrete topology.* Automatyka: p. 771-781.

[10] BABOUT, L., JANASZEWSKI, M., BAKAVOS, D., MCDONALD, S.A., PRANGNELL, P.B., MARROW, T.J. and WITHERS, P.J., 2010a. *3D Inspection of Fabrication and Degradation Processes from X-ray (micro) Tomography Images using a Hole Closing Algorithm*. In: *Proceedings of IEEE International Conference on Image Systems and Techniques (IST2010)*. Thessaloniki, Greece. p. 337-342.

[11] BABOUT, L., JANASZEWSKI, M., MARROW, T.J. and WITHERS, P.J., 2010b. *How to fill a hole in a crack? Case study of intergranular stress corrosion cracking in austenitic stainless steel.* Scripta Materialia. Submitted.

[12] BABOUT, L., JOPEK, L., JANASZEWSKI, M., PREUSS, M. and BUFFIERE, J.-Y., 2009. *Wavelet-based texture segmentation of titanium based alloy lamellar microstructure: application to images from optical microscope and X-ray microtomography.* Elektryka, 114: p. 181-187.

[13] BABOUT, L., LUDWIG, W., MAIRE, E. and BUFFIERE, J.Y., 2003. *Damage assessment in metallic structural materials using high resolution synchrotron X-ray tomography.* Nuclear Instruments and Methods in Physics Research Section B: Beam Interactions with Materials and Atoms, 200: p. 303-307.

[14] BABOUT, L., MAIRE, E., BUFFIERE, J.Y. and FOUGERES, R., 2001. *Characterization by X-ray computed tomography of decohesion, porosity growth and coalescence in model metal matrix composites.* Acta Materialia, 49: p. 2055-2063.

[15] BABOUT, L., MAIRE, E. and FOUGERES, R., 2004c. *Damage initiation in model metallic materials: X-ray tomography and modelling.* Acta Materialia, 52: p. 2475-2487.

[16] BABOUT, L., MARROW, T.J., ENGELBERG, D. and WITHERS, P.J., 2006a. *X-ray microtomographic observation of intergranular stress corrosion cracking in sensitised austenitic stainless steel.* Materials Science and Technology, 9: p. 1068-1075.

[17] BABOUT, L., MARROW, T.J., MUMMERY, P.M. and WITHERS, P.J., 2006b. *Mapping the evolution of density in 3D of thermally oxidised graphite for nuclear applications.* Scripta Materialia, 54: p. 829-834.

[18] BABOUT, L., MARROW, T.J. and PREUSS, M., 2006c. *Sequential X-ray tomography studies of damage assessment in materials science*. In: *Proceedings of 4th Symposium on Process Tomography in Poland.* Warsaw. p. 159-162.

[19] BABOUT, L., MARSDEN, B.J., MUMMERY, P.M. and MARROW, T.J., 2008. *Three-dimensional characterization and thermal property modelling of thermally oxidized nuclear graphite.* Acta Materialia, 56: p. 4242-4254.

[20] BABOUT, L., MUMMERY, P.M., MARROW, T.J., TZELEPI, A. and WITHERS, P.J., 2005. The *effect of thermal oxidation on polycrystalline graphite studied by X-ray tomography.* Carbon, 43: p. 765-774.

[21] BARUCHEL, J., BUFFIERE, J.Y., MAIRE, E., MERLE, P. and PEIX, G., 2000. *X-ray tomography in materials science*. Paris: Hermes Science, 204 p.

[22] BENNETT, J.A. and YOUNG, R.J., 1997. *Micromechanical aspects of fibre/crack interactions in an aramid/epoxy composite.* Composites Science and Technology, 57: p. 945-956.

[23] BERRE, C., FOK, S.L., MARSDEN, B.J., MUMMERY, P.M., MARROW, T.J. and NEIGHBOUR, G.B., 2008a. *Microstructural modelling of nuclear graphite using multi-phase models.* Journal of Nuclear Materials, 380: p. 46-58.

[24] BERRE, C., FOK, S.L., MUMMERY, P.M., ALI, J., MARSDEN, B.J., MARROW, T.J. and NEIGHBOUR, G.B., 2008b. *Failure analysis of the effects of porosity in thermally oxidised nuclear graphite using finite element modelling.* Journal of Nuclear Materials, 381: p. 1-8.

[25] BERTRAND, G., 1994. *Simple points, topological numbers and geodesic neighborhoods in cubic grids.* Pattern Recognition Letters, 15: p. 1003-1011.

[26] BERTRAND, G. and MALANDAIN, G., 1994. a *new characterization of three-dimensional simple points.* Pattern Recognition Letters, 15: p. 169-175.

[27] BIROSCA, S., BUFFIERE, J.Y., GARCIA-PASTOR, F.A., KARADGE, M., BABOUT, L. and PREUSS, M., 2010. *Corrigendum to "Three-dimensional characterization of fatigue cracks in Ti-6246 using X-ray tomography and electron backscatter diffraction" [Acta Materialia 57 (2009) 5834-5847](DOI:10.1016/j.actamat.2009.08.009).* Acta Materialia, 58: p. 1466.

[28] BOCCACCINI, A.R., 1998. *Incorporation of porosity to control the residual thermal stresses in ceramic composites and laminates.* The European Physical Journal: Applied Physics, 2: p. 197-202.

[29] BORGEFORS, G., 1986. *Distance transformations in digital images.* Computer Vision, Graphics, and Image Processing, 34: p. 344-371.

[30] BREVAL, E., KLIMKIEWICZ, M., AGRAWAL, D.K. and RUSINKO, F., 2002. *Pinhole formation and weight loss during oxidation of industrial graphite and carbon.* Carbon, 40: p. 1017-1027.

[31] BROCKLEHURST, J.E., BROWN, R.G., GILCHRIST, K.E. and LABATON, V.Y., 1970. The *effect of radiolytic oxidation on the physical properties of graphite.* Journal of Nuclear Materials, 35: p. 183-194.

[32] BUFFIÈRE, J.-Y., SAVELLI, S., JOUNEAU, P.H., MAIRE, E. and FOUGÈRES, R., 2001. *Experimental study of porosity and its relation to fatigue mechanisms of model Al-Si7-Mg0.3 cast Al alloys.* Materials Science and Engineering: A, 316: p. 115-126.

[33] BUFFIERE, J.-Y., MAIRE, E., CLOETENS, P., LORMAND, G. and FOUGERES, R., 1999. *Characterization of internal damage in a MMC_p using X-ray synchrotron phase contrast microtomography.* Acta Materialia, 47: p. 1613-1625.

[34] BURCHELL, T.D., 2001. *Thermal properties and nuclear energy applications*. In: *Graphite and Precursors*. P. Delhaes, Editor. CRC Press. 312 p.

[35] BURCHELL, T.D., PICKUP, I.M., MCENANEY, B. and COOKE, R.G., 1986. *The relationship between microstructure and the reduction of elastic modulus in thermally and radiolytically corroded nuclear graphites.* Carbon, 24: p. 545-549.

[36] BYSTRZYCKI, J., PRZETAKIEWICZ, W. and KURZYDŁOWSKI, K.J., 1993. *Study of annealing twins and island grains in F.C.C. alloy.* Acta Metallurgica et Materialia, 41: p. 2639-2649.

[37] CALAS-BLANCHARD, C., COMTAT, M., MARTY, J.L. and MAURAN, S., 2003. *Textural characterisation of graphite matrices using electrochemical methods.* Carbon, 41: p. 123-130.

[38] CERNUSCHI, F., AHMANIEMI, S., VUORISTO, P. and MANTYLA, T., 2004. *Modelling of thermal conductivity of porous materials: application to thick thermal barrier coatings.* Journal of the European Ceramic Society, 24: p. 2657-2667.

[39] CLOETENS, P., LUDWIG, W., BARUCHEL, J., VAN DYCK, D., VAN LANDUYT, J., GUIGAY, J.P. and SCHLENKER, M., 1999. *Holotomography: Quantitative phase tomography with micrometer resolution using hard synchrotron radiation X-rays.* Applied Physics Letters, 75: p. 2912-2914.

[40] CLOETENS, P., PATEYRON-SALOME, M., BUFFIERE, J.Y., PEIX, G., BARUCHEL, J., PEYRIN, F. and SCHLENKER, M., 1997. *Observation of microstructure and damage in materials by phase sensitive radiography and tomography.* Journal of Applied Physics, 81: p. 5878-5886.

[41] CORMEN, T.H., LEISERSON, C.E., RIVEST, R.L. and STEIN, C., 2001. *Introduction to algorithms (second edition)*. Cambridge: MIT Press. 1180 p.

[42] COUPRIE, M., COEURJOLLY, D. and ZROUR, R., 2007. *Discrete bisector function and Euclidean skeleton in 2D and 3D.* Image and Vision Computing, 25: p. 1543-1556.

[43] DAVIS, J.R., 2000. *Corrosion: understanding the basics*: ASM International. 563 p.

[44] DETTORI, L. and SEMLER, L., 2007. a *comparison of wavelet, ridgelet, and curvelet-based texture classification algorithms in computed tomography.* Computers in Biology and Medicine, 37: p. 486-498.

[45] DONOHO, D., 2001. *Ridge functions and orthonormal ridgelets.* Journal of Approximation Theory, 111: p. 143-179.

[46] DOUARCHE, N., ROUBY, D., PEIX, G. and JOUIN, J.M., 2001. *Relations between X-ray tomography, density and mechanical properties in carbon-carbon composites.* Carbon, 39: p. 1455-1465.

[47] ELAQRA, H., GODIN, N., PEIX, G., R'MILI, M. and FANTOZZI, G., 2007. *Damage evolution analysis in mortar, during compressive loading using acoustic emission and X-ray tomography: Effects of the sand/cement ratio.* Cement and Concrete Research, 37: p. 703-713.

[48] EULER, F., 1957. *Simple geometric model for the effect of porosity on materials constants.* Journal of Applied Physics, 28: p. 1342-1345.

[49] FELDKAMP, L.A., DAVIS, L.C. and KRESS, J.W., 1984. *Practical cone-beam algorithm.* Journal of Optical Society of America A, 1: p. 612-619.

[50] FERRIE, E., BUFFIERE, J.-Y. and LUDWIG, W., 2005. *3D characterisation of the nucleation of a short fatigue crack at a pore in a cast Al alloy using high resolution synchrotron microtomography.* International Journal of Fatigue, 27: p. 1215-1220.

[51] FERRIE, E. and SAUZAY, M., 2009. *Influence of local crystallographic orientation on short crack propagation in high cycle fatigue of 316LN steel.* Journal of Nuclear Materials, 386-388: p. 666-669.

[52] FISCHER, F., LIM, G.T., HANDGE, U.A. and ALTSADT, V., 2009. *Numerical simulation of mechanical properties of cellular materials using computed tomography analysis.* Journal of Cellular Plastics, 45: p. 441-460.

[53] GERTSMAN, V.Y. and BRUEMMER, S.M., 2001. *Study of grain boundary character along intergranular stress corrosion crack paths in austenitic alloys.* Acta Materialia, 49: p. 1589-1598.

[54] GONZALEZ, M., DOMINGUEZ, G. and BATHIAS, C., 2000. *Some Results from X-Ray Computed Tomography Applied to Metal Matrix Composites.* Journal of Composites Technology and Research, 22: p. 45-48.

[55] GROEBER, M.A., HALEY, B.K., UCHIC, M.D., DIMIDUK, D.M. and GHOSH, S., 2006. *3D reconstruction and characterization of polycrystalline microstructures using a FIB-SEM system.* Materials Characterization, 57: p. 259-273.

[56] HAMILTON, R.W., FORSTER, M.F., DASHWOOD, R.J. and LEE, P.D., 2002. *Application of X-ray tomography to quantify the distribution of TiB2 particulate in aluminium.* Scripta Materialia, 46: p. 25-29.

[57] HODGKINS, A., MARROW, T.J., MUMMERY, P., MARSDEN, B. and FOK, A., 2006. *X-ray tomography observation of crack propagation in nuclear graphite.* Materials Science and Technology, 22: p. 1045-1051.

[58] HOPPEL, H.W., KAUTZ, M., XU, C., MURASHKIN, M., LANGDON, T.G., VALIEV, R.Z. and MUGHRABI, H., 2006. *An overview: Fatigue behaviour of ultrafine-grained metals and alloys.* International Journal of Fatigue, 28: p. 1001-1010.

[58] HOROWITZ, H.H., 1983. *Chemical studies of polythionic acid stress-corrosion cracking.* Corrosion Science, 23: p. 353-362.

[60] HYUN, S.K., MURAKAMI, K. and NAKAJIMA, H., 2001. *Anisotropic mechanical properties of porous copper fabricated by unidirectional solidification.* Materials Science and Engineering: A, 299: p. 241-248.

[61] HYVARINEN, A. and OJA, E., 2000. *Independent component analysis: Algorithms and applications.* Neural Networks, 13: p. 411-430.

[62] JANASZEWSKI, M., COUPRIE, M. and BABOUT, L., 2009. *Geometric approach to hole segmentation and hole closing in 3D volumetric objects*. In: *Progress in Pattern Recognition, Image Analysis, Computer Vision, and Applications*. E. BayroCorrochano and J.O. Eklundh, Editors. Lecture Notes in Computer Science. SPRINGER-VERLAG BERLIN: Berlin. 255-262 p.

[63] JANASZEWSKI, M., COUPRIE, M. and BABOUT, L., 2010. *Hole filling in 3D volumetric objects.* Pattern Recognition, 43: p. 3548-3559.

[64] JANASZEWSKI, M., MARROW, T.J. and BABOUT, L., 2007. *Adaptive 3D thinning algorithm to detect bridging ligaments during intergranular stress corrosion cracking of stainless steel*. In: *Proceedings of 5th World Congress on industrial Process Tomography*. Bergen. p. 1107-1115.

[65] JIVKOV, A.P., STEVENS, N.P.C. and MARROW, T.J., 2006. a *three-dimensional computational model for intergranular cracking.* Computational Materials Science, 38: p. 442-453.

[66] JOHNSON, G., KING, A., HONNICKE, M.G., MARROW, J. and LUDWIG, W., 2008. *X-ray diffraction contrast tomography: a novel technique for three-dimensional grain mapping of polycrystals. II. The combined case.* Journal of Applied Crystallography, 41: p. 310-318.

[67] JOHNSON, P.A.V., SCHOFIELD, P., BLANCHARD, A. and KELLY, B.T., 1982. *Analysis of the effect of radiolytic oxidation in carbon-dioxide on the transport of gases through graphite.* Carbon, 20: p. 141-142.

[68] JOPEK, Ł., NOWOTNIAK, R., POSTOLSKI, M., BABOUT, L. and JANASZEWSKI, M., 2009. *Application of quantum genetic algorithms in feature selection problem.* Automatyka, 13: p. 1219-1231. in Polish.

[69] KADAR, C., MAIRE, E., BORBELY, A., PEIX, G., LENDVAI, J. and RAJKOVITS, Z., 2004. *X-ray tomography and finite element simulation of the indentation behavior of metal foams.* Materials Science and Engineering A, 387-389: p. 321-325.

[70] KAK, A.C. and SLANEY, M., 1987. *Principles of computerized tomographic imaging*. New York.

[71] KELLY, B.T., MARSDEN, B.J. and HALL, K., *Irradiation damage in graphite due to fast neutrons in fission and fusion systems*. 2000, Vienna: International Atomic Energy Agency.AEA-TECDOC-1154. 220 p.

[72] KENESEI, P., BIERMANN, H. and BORBELY, A., 2005. *Structure-property relationship in particle reinforced metal-matrix composites based on holotomography.* Scripta Materialia, 53: p. 787-791.

[73] KING, A., HERBIG, M., LUDWIG, W., REISCHIG, P., LAURIDSEN, E.M., MARROW, T. and BUFFIERE, J.Y., 2010. *Non-destructive analysis of micro texture and grain boundary character from X-ray diffraction contrast tomography.* Nuclear Instruments and Methods in Physics Research, Section B: Beam Interactions with Materials and Atoms, 268: p. 291-296.

[74] KING, A., JOHNSON, G., ENGELBERG, D., LUDWIG, W. and MARROW, J., 2008. *Observations of intergranular stress corrosion cracking in a grain-mapped polycrystal.* Science, 321: p. 382-385.

[75] KINOSHITA, T. and MUNEKAWA, S., 1997. *Effect of grain boundary segregation on thermal conductivity of hot-pressed silicon carbide.* Acta Materialia, 45: p. 2001-2012.

[76] KNUDSEN, F.P., 1959. *Dependence of mechanical strength of brittle polycrystalline specimens on porosity and grain size.* Journal of American Ceramic Society, 42: p. 376-387.

[77] KOKAWA, H., SHIMADA, M. and SATO, Y.S., 2000. *Grain-boundary structure and precipitation in sensitized austenitic stainless steel.* Journal of Metallurgy, 52: p. 34-37.

[78] KONG, T.Y., 1989. a *digital fundamental group.* Computers and Graphics, 13: p. 159-166.

[79] KONG, T.Y. and ROSENFELD, A., 1989. *Digital topology: Introduction and survey.* Computer Vision, Graphics, and Image Processing, 48: p. 357-393.

[80] KORNEV, A., BABOUT, L., JANASZEWSKI, M. and TALBOT, H., 2010. *Outer Surface Reconstruction for 3d Fractured Objects*. In: *Computer Vision and Graphics, Pts 1 and 2*. L. Bolc et al., Editors. Lecture Notes in Computer Science. SPRINGER-VERLAG: Berlin. p. 57-64.

[81] LI, W.J., WANG, N., CHEN, J., LIU, G., PAN, Z.Y., GUAN, Y., YANG, Y.H., WU, W.Q., TIAN, J.P., WEI, S.Q., WU, Z.Y., TIAN, Y.C., and GUO, L., 2009. *Quantitative study of interior nanostructure in hollow zinc oxide particles on the basis of nondestructive X-ray nanotomography.* Applied Physics Letters, 95: 053108.

[82] LIMODIN, N., SALVO, L., SUERY, M. and DIMICHIEL, M., 2007. in *situ investigation by X-ray tomography of the overall and local microstructural changes occurring during partial remelting of an Al-15.8 wt.% Cu alloy.* Acta Materialia, 55: p. 3177-3191.

[83] LIN, H. and POPE, D.P., 1993. The *influence of grain boundary geometry on intergranular crack propagation in Ni3Al.* Acta Metallurgica et Materialia, 41: p. 553-562.

[84] LIN, P., PALUMBO, G., ERB, U. and AUST, K.T., 1995. *Influence of grain boundary character distribution on sensitization and intergranular corrosion of alloy 600.* Scripta Metallurgica et Materialia, 33: p. 1387-1392.

[85] LLORCA, J., 2000. *Void formation in metal matrix composite*. In: *Comprehensive composites materials*. T.W. Clyne, Editor. Elsevier: Amsterdam. 91-115 p.

[86] LUDWIG, W., BUFFIERE, J.Y., SAVELLI, S. and CLOETENS, P., 2003. *Study of the interaction of a short fatigue crack with grain boundaries in a cast Al alloy using X-ray microtomography.* Acta Materialia, 51: p. 585-598.

[87] LUDWIG, W., KING, A., HERBIG, M., REISCHIG, P., MARROW, J., BABOUT, L., LAURIDSEN, E.M., PROUDHON, H. and BUFFIERE, J.Y., 2010. *Characterization of polycrystalline materials by combined use of synchrotron X-ray imaging and diffraction techniques.* JOM, 62: p. 22-28.

[88] LUDWIG, W., SCHMIDT, S., LAURIDSEN, E.M. and POULSEN, H.F., 2008. *X-ray diffraction contrast tomography: a novel technique for three-dimensional grain mapping of polycrystals. I. Direct beam case.* Journal of Applied Crystallography, 41: p. 302-309.

[89] LUTJERING, G., 1998. *Influence of processing on microstructure and mechanical properties of ($\alpha + \beta$) titanium alloys.* Materials Science and Engineering A, 243: p. 32-45.

[90] LUTJERING, G. and WILLIAMS, J.C., 2007. *Titanium: engineering materials and processes*. Heidelberg: Springer Verlag. 442 p.

[91] MAHAJAN, S., PANDE, C.S., IMAM, M.A. and RATH, B.B., 1997. *Formation of annealing twins in f.c.c. crystals.* Acta Materialia, 45: p. 2633-2638.

[92] MAIRE, E., BABOUT, L., BUFFIERE, J.-Y. and FOUGERES., R., 2001. *Recent results on 3D characterisation of microstructure and damage of metal matrix composites and a metallic foam using X-ray tomography.* Materials Science and Engineering A, 319-321: p. 216-219.

[93] MAIRE, E., BOUAZIZ, O., DI MICHIEL, M. and VERDU, C., 2008. *Initiation and growth of damage in a dual-phase steel observed by X-ray microtomography.* Acta Materialia, 56: p. 4954-4964.

[94] MAIRE, E., CHAIX, J.M., GLANDUT, N., SALVO, L. and BABOUT, L., 2002. *Elaboration de composites modèles Al-ZrO2 par métallurgie des poudres.* La Revue de Métallurgie-CIT/Science et génie des matériaux: p. 1043-1049.

[95] MAIRE, E., COLOMBO, P., ADRIEN, J., BABOUT, L. and BIASETTO, L., 2007. *Characterization of the morphology of cellular ceramics by 3D image processing of X-ray tomography.* Journal of the European Ceramic Society, 27: p. 1973-1981.

[96] MAIRE, E., FAZEKAS, A., SALVO, L., DENDIEVEL, R., YOUSSEF, S., CLOETENS, P. and LETANG, J.M., 2003. *X-ray tomography applied to the characterization of cellular materials. Related finite element modeling problems.* Composites Science and Technology, 63: p. 2431-2443.

[97] MAIRE, E., OWEN, A., BUFFIERE, J.-Y. and WITHERS, P.J., 2001. *A synchrotron X-ray study of a Ti/SiCf composite during in-situ straining.* Acta Materialia, 49: p. 143-153.

[98] MALANDAIN, G., BERTRAND, G. and AYACHE, N., 1993. *Topological segmentation of discrete surfaces.* International Journal of Computer Vision, 10: p. 183-197.

[99] MALLAT, S.G., 1989. a *theory for multiresolution signal decomposition: the wavelet representation.* IEEE Transactions on Pattern Analysis and Machine Intelligence, 11: p. 674-693.

[100] MARROW, J., LUPRANO, V. and ROBERTS, S., 1993. *Scanning acoustic microscopy observations of high-temperature crack-bridging mechanisms in alumina.* Journal of the American Ceramic Society, 76: p. 2915-2918.

[101] MARROW, T.J., BABOUT, L., JIVKOV, A.P., WOOD, P., ENGELBERG, D., STEVENS, N., WITHERS, P.J. and NEWMAN, R.C., 2006. *Three dimensional observations and modelling of intergranular stress corrosion cracking in austenitic stainless steel.* Journal of Nuclear Materials, 352: p. 62-74.

[102] MARTIN, C.F., JOSSEROND, C., SALVO, L., BLANDIN, J.J., CLOETENS, P. and BOLLER, E., 2000. *Characterisation by X-ray micro-tomography of cavity coalescence during superplastic deformation.* Scripta Materialia, 42: p. 375-381.

[103] MARUYAMA, T., KAITO, T., ONOSE, S. and SHIBAHARA, I., 1995. *Change in physical properties of high density isotropic graphites irradiated in the "JOYO" fast reactor.* Journal of Nuclear Materials, 225: p. 267-272.

[104] MASAKI, K., OCHI, Y., MATSUMURA, T. and SANO, Y., 2007. *Effects of laser peening treatment on high cycle fatigue properties of degassing-processed cast aluminum alloy.* Materials Science & Engineering A, 468-470: p. 171-175.

[105] MCDONALD, S.A., MUMMERY, P.M., JOHNSON, G. and WITHERS, P.J., 2006. *Characterization of the three-dimensional structure of a metallic foam during compressive deformation.* Journal of Microscopy, 223: p. 150-158.

[106] MCDONALD, S.A., PREUSS, M., MAIRE, E., BUFFIERE, J.Y., MUMMERY, P.M. and WITHERS, P.J., 2003. *X-ray tomographic imaging of Ti/SiC composites.* Journal of Microscopy, 209: p. 102-112.

[107] MEREDITH, R.E. and TOBIAS, C.W., 1962. *Conduction in heterogeneous systems*. In: *Advances in Electrochemistry and Electrochemical Engineering*. C.W. Tobias, Editor. Interscience: New York. 15-47 p.

[108] MIYOSHI, M., HAMAKUBO, T., KODAMA, T., TSUCHIYA, M., KOISHIKAWA, A. and AOKI, N., 2008. *Development of the compact low-energy soft X-ray CT instrument for the soft material structural analysis.* Journal of Vacuum Science and Technology B: Microelectronics and Nanometer Structures, 26: p. 2356-2361.

[109] MONTEILLET, F. and MOUSSI, F., 1986. *Physique et mecanique de l'endommagement*, ed. F. Monteillet and F. Moussi. Les Ulis: Les Editions de Physique. 258 p.

[110] MONTMINY, M.D., TANNENBAUM, A.R. and MACOSKO, C.W., 2001. *New algorithms for 3-D imaging and analysis of open-celled foams.* Journal of Cellular Plastics, 37: p. 501-515.

[111] MORALES-RODRIGUEZ, A., REYNAUD, P., FANTOZZI, G., ADRIEN, J. and MAIRE, E., 2009. *Porosity analysis of long-fiber-reinforced ceramic matrix composites using X-ray tomography.* Scripta Materialia, 60: p. 388-390.

[112] NIBLACK, C.W., GIBBONS, P.B. and CAPSON, D.W., 1992. *Generating skeletons and centerlines from the distance transform.* CVGIP: Graphical Models and Image Processing, 54: p. 420-437.

[113] NIGHTINGALE, R.E., 1962. *Nuclear graphite*. New York and London: Academic Press. 547 p.

[114] NIKOLAIDIS, N. and PITA, I., 2001. *3-D Image Processing Algorithms*. New York: Wiley-Interscience. 176 p.

[115] OSTADI, H., RAMA, P., LIU, Y., CHEN, R., ZHANG, X.X. and JIANG, K., 2010. *Threshold fine-tuning and 3D characterisation of porous media using X-ray nanotomography.* Current Nanoscience, 6: p. 226-231.

[116] PAL, N.R. and PAL, S.K., 1993. a *review on image segmentation techniques.* Pattern Recognition, 26: p. 1277-1294.

[117] PALUMBO, G., AUST, K.T., LEHOCKEY, E.M., ERB, U. and LIN, P., 1998. *On a more restrictive geometric criterion for "special" CSL grain boundaries.* Scripta Materialia, 38: p. 1685-1690.

[118] PARKER, W.J., JENKINS, R.J., BUTLER, C.P. and ABBOTT, G.L., 1961. *Flash method of determining thermal diffusivity.* J. Appl. Phys., 32: p. 1679-1684.

[119] PETROU, M. and GARCIA SEVILLA, P., 2006. *Image processing: Dealing with texture*: Wiley. 634 p.

[120] PICHLER, O., TEUNER, A. and HOSTICKA, B.J., 1996. a *comparison of texture feature extraction using adaptive Gabor filtering, pyramidal and tree structured wavelet transforms.* Pattern Recognition, 29: p. 733-742.

[121] PICKUP, I.M., MCENANEY, B. and COOKE, R.G., 1986. *Fracture processes in graphite and the effects of oxidation.* Carbon, 24: p. 535-543.

[122] PRASHER, R., 2006. *Transverse thermal conductivity of porous materials made from aligned nano- and microcylindrical pores.* Journal of Applied Physics, 100: p. 064302-1-7.

[123] PREUSS, M., WITHERS, P.J., MAIRE, E. and BUFFIERE, J.-Y., 2002. *SiC single fibre full-fragmentation during straining in a Ti-6Al-4V matrix studied by synchrotron X-rays.* Acta Materialia, 50: p. 3177-3192.

[124] PROUDHON, H., BUFFIERE, J.-Y. and FOUVRY, S., 2006. *Characterisation of fretting fatigue damage using synchrotron X-ray micro-tomography.* Tribology International, 39: p. 1106-1113.

[125] RAGHAVAN, S., WANG, H., DINWIDDIE, R.B., PORTER, W.D. and MAYO, M.J., 1998. The *effect of grain size, porosity and yttria content on the thermal conductivity of nanocrystalline zirconia.* Scripta Materialia, 39: p. 1119-1125.

[126] RANDRIANALISOA, J. and BAILLIS, D., 2007. *Thermal conductivity across nanostructured porous silicon films.* Journal of Physics: Conference Series, 92: p. 012081-1-4.

[127] RATTANASAK, U. and KENDALL, K., 2005. *Pore structure of cement/pozzolan composites by X-ray microtomography.* Cement and Concrete Research, 35: p. 637-640.

[128] REMY, E. and THIEL, E., 2005. *Exact medial axis with euclidean distance.* Image and Vision Computing, 23: p. 167-175.

[129] RICE, R., 2005. *Use of normalized porosity in models for the porosity dependence of mechanical properties.* Journal of Materials Science, 40: p. 983-989.

[130] RICE, R.W., 1996. *Evaluation and extension of physical property-porosity models based on minimum solid area.* Journal of Materials Science, 31: p. 102-118.

[131] ROBERTS, A.P. and GARBOCZI, E.J., 2000. *Elastic properties of model porous ceramics.* Journal of American Ceramic Society, 83: p. 3041-3048.

[132] RUSS, G.C., 1995. The *imaging processing handbook*. 2 ed. Boca Raton: CRC Press. 771 p.

[133] RYAN, M.P., WILLIAMS, D.E., CHATER, R.J., HUTTON, B.M. and MCPHAIL, D.S., 2002. *Why stainless steel corrodes.* Nature, 415: p. 770-774.

[134] SADANANDA, K. and VASUDEVAN, A.K., 2005. *Fatigue crack growth behavior of titanium alloys.* International Journal of Fatigue, 27: p. 1255-1266.

[135] SARRAZIN, C., CHIRON, R., LESTERLIN, S. and PETIT, J., 1994. *Electron backscattering pattern identification of surface morphology of fatigue cracks in TA6V.* Fatigue and Fracture of Engineering Materials and Structures, 17: p. 1383-1389.

[136] SARRAZIN-BAUDOUX, C., 2005. *Abnormal near-threshold fatigue crack propagation of Ti alloys: Role of the microstructure.* International Journal of Fatigue, 27: p. 773-782.

[137] SAÚDE, A.V., COUPRIE, M. and LOTUFO, R.A., 2009. *Discrete 2D and 3D euclidean medial axis in higher resolution.* Image and Vision Computing, 27: p. 354-363.

[138] SAVAGE, M.F., TATALOVICH, J., ZUPAN, M., HEMKER, K.J. and MILLS, M.J., 2001. *Deformation mechanisms and microtensile behavior of single colony Ti-6242Si.* Materials Science and Engineering A, 319-321: p. 398-403.

[139] SCHIJVE, J., 2009. *Fatigue of structures and materials*. 2nd ed. Berlin: Springer. 621 p.

[140] SCHILLING, P.J., KAREDLA, B.P.R., TATIPARTHI, A.K., VERGES, M.A. and HERRINGTON, P.D., 2005. *X-ray computed microtomography of internal damage in fiber reinforced polymer matrix composites.* Composites Science and Technology, 65: p. 2071-2078.

[141] SCHROEDER, G., ALBRECHT, J. and LUETJERING, G., 2001. *Fatigue crack propagation in titanium alloys with lamellar and bi-lamellar microstructures.* Materials Science and Engineering A, 319-321: p. 602-606.

[142] SCHULZ, B., 1981. *Thermal conductivity of porous and highly porous materials.* High Temperature High Pressure, 13: p. 649-660.

[143] SCOTT, P.M., 2000. *Stress corrosion cracking in pressurized water reactors--interpretation, modeling, and remedies.* Corrosion, 56: p. 771-782.

[144] SERRA, J., 1982. *Image Analysis and mathematical morphology*. London: Academic Press. 610 p.

[145] SEZGIN, M. and SANKUR, B., 2004. *Survey over image thresholding techniques and quantitative performance evaluation.* Journal of Electronic Imaging, 13: p. 146-168.

[146] SHEN, H., NUTT, S. and HULL, D., 2004. *Direct observation and measurement of fiber architecture in short fiber-polymer composite foam through micro-CT imaging.* Composites Science and Technology, 64: p. 2113-2120.

[147] SHIMADA, M., KOKAWA, H., WANG, Z.J., SATO, Y.S. and KARIBE, I., 2002. *Optimization of grain boundary character distribution for intergranular corrosion resistant 304 stainless steel by twin-induced grain boundary engineering.* Acta Materialia, 50: p. 2331-2341.

[148] SINCLAIR, R., PREUSS, M., MAIRE, E., BUFFIERE, J.-Y., BOWEN, P. and WITHERS, P.J., 2004. The *effect of fibre fractures in the bridging zone of fatigue cracked Ti-6Al-4V/SiC fibre composites.* Acta Materialia, 52: p. 1423-1438.

[149] SOILLE, P., 2003. *Morphological Image Analysis*. 2nd ed. Berlin: Springer. 391 p.

[150] STRZELECKI, M., MATERKA, A. and SZCZYPINSKI, P., 2006. *MaZda*. In: *Texture analysis for magnetic resonance imaging*. M. Hajek et al., Editors. Med4publishing: Prague. 105-111 p.

[151] SUMITA, J., SHIBATA, T., KUNIMOTO, E., YAMAJI, M., KONISHI, T. and SAWA, K., 2010. *Investigation of microstructural change by X-ray tomography and anisotropic effect on thermal property of thermally oxidized 2D-C/C composite for very high temperature reactor.* Journal of Nuclear Science and Technology, 47: p. 411-420.

[152] TAKAYA, S., SUZUKI, T., MATSUMOTO, Y., DEMACHI, K. and UESAKA, M., 2004. *Estimation of stress corrosion cracking sensitivity of type 304 stainless steel by magnetic force microscope.* Journal of Nuclear Materials, 327: p. 19-26.

[153] TEUNER, A., PICHLER, O. and HOSTICKA, B.J., 1995. *Unsupervised texture segmentation of images using tuned matched Gabor filters.* IEEE Transactions on Image Processing, 4: p. 863-870.

[154] THOMASON, P.F., 1990. *Ductile fracture of metals (1st edition).* Oxford: Pergamon Press. 219 p.

[155] THROWER, P.A., BOGNET, J.C. and MATHEW, G.K., 1982. The *influence of oxidation on the structure and strength of graphite-I: Materials of different structure.* Carbon, 20: p. 457-464.

[156] TING, K., 1999. The *evaluation of intergranular stress corrosion cracking problems of stainless steel piping in Taiwan BWR-6 nuclear power plant.* Nuclear Engineering and Design, 191: p. 245-254.

[157] TRILLO, E.A. and MURR, L.E., 1999. *Effects of carbon content, deformation, and interfacial energetics on carbide precipitation and corrosion sensitization in 304 stainless steel.* Acta Materialia, 47: p. 235-245.

[158] TURNBULL, A., HORNER, D.A. and CONNOLLY, B.J., 2009. *Challenges in modelling the evolution of stress corrosion cracks from pits.* Engineering Fracture Mechanics, 76: p. 633-640.

[159] UTHUS, L., HOFF, I. and HORVLI, I., 2005. *Evaluation of grain shape characterization methods for unbound aggregates*. In: *Proceedings of the Seventh International Conference on the Bearing Capacity of Road, Railways and Airfields*. Trondheim.

[160] VANDERESSE, N., MAIRE, E., DARRIEULAT, M., MONTHEILLET, F., MOREAUD, M. and JEULIN, D., 2008. *Three-dimensional microtomographic study of Widmanstatten microstructures in an alpha/beta titanium alloy.* Scripta Materialia, 58: p. 512-515.

[161] VASUDEVAN, A.K., SADANANDA, K. and GLINKA, G., 2001. *Critical parameters for fatigue damage.* International Journal of Fatigue, 23: p. S39-S53.

[162] VISAGE IMAGING, 2008. *Amira™ 5 User's guide*. 407 p.

[163] WASNIK, D.N., KAIN, V., SAMAJDAR, I., VERLINDEN, B. and DE, P.K., 2002. *Resistance to sensitization and intergranular corrosion through extreme randomization of grain boundaries.* Acta Materialia, 50: p. 4587-4601.

[164] WECK, A., WILKINSON, D.S. and MAIRE, E., 2008a. *Observation of void nucleation, growth and coalescence in a model metal matrix composite using X-ray tomography.* Materials Science and Engineering A, 488: p. 435-445.

[165] WECK, A., WILKINSON, D.S., MAIRE, E. and TODA, H., 2008b. *Visualization by X-ray tomography of void growth and coalescence leading to fracture in model materials.* Acta Materialia, 56: p. 2919-2928.

[166] WHITE, I.F., SMITH, G.M., SAUNDERS, L.J., KAYE, C.J., MARTIN, T.J., CLARKE, G.H. and WAKERLEY, M.W., *Assessment of management modes for graphite from reactor decommissioning*. 1984, Brussels: CEC Nuclear Science and Technology. EUR 9232. 119 p.

[167] WISMANS, J.G.F., VAN DOMMELEN, J.A.W., GOVAERT, L.E., MEIJER, H.E.H. and VAN RIETBERG, B., 2009. *Computed tomography-based modeling of structured polymers.* Journal of Cellular Plastics, 45: p. 157-179.

[168] WITHERS, P.J., 2007. *X-ray nanotomography.* Materials Today, 10: p. 26-34.

[169] WRIGHT, P., MOFFAT, A., SINCLAIR, I. and SPEARING, S.M., 2010. *High resolution tomographic imaging and modelling of notch tip damage in a laminated composite.* Composites Science and Technology, 70: p. 1444-1452.

[170] ZAEFFERER, S., 2003. a *study of active deformation systems in titanium alloys: Dependence on alloy composition and correlation with deformation texture.* Materials Science and Engineering A, 344: p. 20-30.

[171] ZHANG, H., TODA, H., QU, P.C., SAKAGUCHI, Y., KOBAYASHI, M., UESUGI, K. and SUZUKI, Y., 2009. *Three-dimensional fatigue crack growth behavior in an aluminum alloy investigated with in situ high-resolution synchrotron X-ray microtomography.* Acta Materialia, 57: p. 3287-3300.

[172] ZHOU, Y. and TOGA, A.W., 1999. *Efficient skeletonization of volumetric objects.* IEEE Transactions on Visualization and Computer Graphics, 5: p. 196-209.

STRESZCZENIE

Niniejsza rozprawa habilitacyjna przedstawia nowe metody eksperymentalne i obliczeniowe stosowane do badania stopnia degradacji materiałów konstrukcyjnych. Zadania te zostały zrealizowane przez zastosowanie tomografii rentgenowskiej i nowych algorytmów analizy i przetwarzania obrazów.

Praca składa się z czterech rozdziałów. W pierwszym zostały zaprezentowane najczęstsze procesy prowadzące do degradacji materiałów konstrukcyjnych. Przedstawiono w nim również jak w ciągu ostatnich dziesięciu lat tomografia rentgenowska stała się nieniszczącym narzędziem do trójwymiarowej wizualizacji tych procesów. Zjawisko to zostało szczegółowo przedstawione na przykładzie ilościowej analizy procesu rozprzestrzeniania się przełomu w materiałach kompozytowych. Materiał ten został specjalnie wyprodukowany w celu spełnienia wymagań tomografii rentgenowskiej. Na tym przykładzie wykazano wyraźnie, że poza unikatowością obrazu trójwymiarowego uzyskanego za pomocą tomografii rentgenowskiej zawiera on również wiele informacji o charakterze jakościowym wynikających z analizy skomplikowanej mikrostruktury lub niskiego kontrastu analizowanych obrazów. Pozwala to sformułować ważny wniosek wynikający z pracy: należy rozwijać badania w dziedzinie przetwarzania obrazów w celu pozyskiwania informacji ilościowych z obrazów 3D.

Kolejne trzy rozdziały są poświęcone przedstawieniu wyników prac zarówno z punktu widzenia inżynierii materiałowej, jak i systemów komputerowych. Obejmują one zagadnienia procesu utleniania grafitu używanego w technice jądrowej, naprężeniowej korozji międzykrystalicznej w austenitycznych stalach nierdzewnych, jak również propagacji szczeliny zmęczeniowej w stopach (α + β) tytanu o strukturze płytkowej. Autor przedstawił swój nowatorski udział w poszczególnych badaniach, zarówno w części doświadczalnej, jak i obliczeniowej. W każdym z rozdziałów zostały podkreślone wyniki uzyskane z tomografii rentgenowskiej, ze szczególnym naciskiem położonym na elementy mikrostruktury, które mają wpływ na proces niszczenia materiału. Następnie przeprowadzone badania zostały rozpatrzone w kontekście systemów komputerowych i zostały zaprezentowane nowe strategie obliczeniowe w zakresie przetwarzania obrazów. W ostatniej części pracy zostały przedstawione wyniki badań z punktu widzenia inżynierii materiałowej, bazujące na danych ilościowych uzyskanych jako wynik przetwarzania obrazów.

Praca ma charakter interdyscyplinarny. Duży nacisk został położony przez autora na całościowe przygotowanie pracy w formie zrozumiałej zarówno dla specjalistów z dziedziny inżynierii materiałowej, jak i systemów komputerowych, którzy chcieliby uzyskać więcej informacji dotyczących drugiej dziedziny wiedzy.

CHARAKTERYSTYKA ZAWODOWA AUTORA

Dr Laurent Babout urodził się w roku 1974 w Rillieux la Pape (Francja). W 1998 r. ukończył studia na *Groupe de Métallurgie Physique et Physique des Matériaux* w INSA Lyon (Francja) i uzyskał tytuł magistra materiałoznawstwa. Następnym etapem jego kariery zawodowej były studia doktoranckie na *Groupe de Métallurgie Physique et Physique des Matériaux*. Tematyka badawcza jego pracy doktorskiej dotyczyła metalicznych kompozytów matrycowych, a ściślej inicjacji uszkodzeń w tych materiałach z wykorzystaniem tomografii rentgenowskiej i metody elementów skończonych. W roku 2002 L. Babout obronił na INSA w Lyonie pracę doktorską nt. „Badanie rozwoju uszkodzeń w niejednorodnych materiałach metalicznych: tomografia rentgenowska i modelowanie".

Od lutego 2003 do września 2005 był zatrudniony jako pracownik naukowo-badawczy w *Materials Science Centre* na Uniwersytecie w Manchesterze. Jego praca koncentrowała się na badaniach nad procesami pęknięć materiałów przemysłowych (takich jak grafit, austenityczna stal nierdzewna i dwu-fazowe ($\alpha + \beta$) stopy tytanu) z wykorzystaniem tomografii rentgenowskiej. W 2005 roku został zatrudniony w Katedrze Informatyki Stosowanej Politechniki Łódzkiej na stanowisku starszego specjalisty ds. informatyki, a następnie adiunkta. Jego aktywność naukowa skupia się przede wszystkim na przetwarzaniu i analizie obrazów trójwymiarowych.

Dr Laurent Babout jest autorem lub współautorem około 50 artykułów naukowych, w tym 16 z tzw. listy filadelfijskiej. Jego artykuły były cytowane około 280 razy i dr Babout ma indeks h powyżej 11. W ostatnich latach aktywnie uczestniczył w projekcie europejskim DENIDIA, będąc wraz z prof. Sankowskim jego współtwórcą i koordynatorem. W ramach projektu prowadził badania naukowe przez okres 6-ciu miesięcy na Uniwersytecie w Manchesterze. Był także sekretarzem 5^{tej} Międzynarodowej Konferencji Tomografii Procesowej, Zakopane 25-26 sierpnia 2008 r.

Działalność dydaktyczna autora rozprawy obejmuje algorytmikę, bazy dane i przedmioty związane z programowaniem komputerów.

ISSN 0137-4834